



**EVALUATION OF HYDROTHERMALLY SYNTHESIZED URANIUM  
DIOXIDE FOR NOVEL SEMICONDUCTOR APPLICATIONS**

DISSERTATION

Christopher M. Young, LTC, USA

AFIT-ENP-DS-16-S-027

**DEPARTMENT OF THE AIR FORCE  
AIR UNIVERSITY**

**AIR FORCE INSTITUTE OF TECHNOLOGY**

---

---

**Wright-Patterson Air Force Base, Ohio**

**DISTRIBUTION STATEMENT A. APPROVED FOR PUBLIC RELEASE;  
DISTRIBUTION UNLIMITED.**

The views expressed in this thesis are those of the author and do not reflect the official policy or position of the United States Air Force, Department of Defense, or the United States Government. This material is declared a work of the U.S. Government and is not subject to copyright protection in the United States.

AFIT-ENP-DS-16-S-027

**EVALUATION OF HYDROTHERMALLY SYNTHESIZED URANIUM  
DIOXIDE FOR NOVEL SEMICONDUCTOR APPLICATIONS**

DISSERTATION

Presented to the Faculty

Department of Engineering Physics

Graduate School of Engineering and Management

Air Force Institute of Technology

Air University

Air Education and Training Command

In Partial Fulfillment of the Requirements for the

Degree of Doctor of Philosophy

Christopher M. Young, LTC, USA

August 2016

**DISTRIBUTION STATEMENT A. APPROVED FOR PUBLIC RELEASE;  
DISTRIBUTION UNLIMITED**

EVALUATION OF HYDROTHERMALLY SYNTHESIZED URANIUM DIOXIDE  
FOR NOVEL SEMICONDUCTOR APPLICATIONS

Christopher M. Young, LTC, USA

Committee Membership:

James C. Petrosky, PhD  
Chair

Larry W. Burggraf, PhD  
Member

John W. McClory, PhD  
Member

William P. Baker, PhD  
Member

ADEDJI B. BADIRU, PhD  
Dean, Graduate School of Engineering and Management

## Abstract

This research is focused on determining the feasibility of using single crystal uranium dioxide,  $\text{UO}_2$ , as the detection medium of a solid state neutron detector. The Air Force Research Laboratory has had recent success in synthesizing single crystal  $\text{UO}_2$  using a hydrothermal growth process. The stoichiometry and single-crystal nature of the hydrothermally synthesized material was determined by x-ray diffraction (XRD) and x-ray photoelectron spectroscopy (XPS). XRD resolved the unit cell to 3 orthogonal and identical lattice parameters of length  $5.4703 \pm 0.0006 \text{ \AA}$  consistent with the fluorite structure of  $\text{UO}_{2.003}$  and of sufficient quality for semiconductor applications. The satellite structure and binding energies, specifically in the region of the U 4f features, were also found to be consistent with nearly stoichiometric  $\text{UO}_2$ .

The stability of the crystal surface was studied with XPS. Using depth-resolved techniques, the binding energy shift of the U 4f photopeaks indicated that the sputtered surface stoichiometry was near that of the sub-surface, shifting only by  $0.15 \pm 0.05 \text{ eV}$  between the maximum depth ( $\sim 50 \text{ \AA}$ ) and the surface with the trend toward higher surface oxide states. The first ever photoelectric work functions of the (111) and (100) surfaces of hydrothermally grown  $\text{UO}_2$  were measured at  $6.28 \pm 0.36 \text{ eV}$  (111) and  $5.80 \pm 0.36 \text{ eV}$  (100). The temporal evolution of the work function measurements deviated less than 6.4% on the (111) surface and 2.1% on the (100) surface between the initial and maximum values over a 24-hour period indicating an electronically stable surface under high vacuum conditions.

The effective Debye temperature of hydrothermally synthesized  $\text{UO}_2$  was measured and a lattice stiffening transition was found at  $476 \pm 91$  K on a clean and annealed surface. The effective Debye temperature below the transition was  $500 \pm 59$  K and  $165 \pm 21$  K above it. This surface transition is likely that of a mixed phase of  $(\text{UO}_{2+x} + \text{U}_4\text{O}_{9-y})$  below the transition to a single  $(\text{UO}_{2+x})$  phase above the transition. This implies the single  $(\text{UO}_{2+x})$  phase is less rigid which has important implications for crystal doping and purification.

Analysis of the current-voltage response of a Ag- $\text{UO}_2$ -GaIn device suggests that the crystal bulk is n-type, an important discovery toward fabrication of engineered junctions. A rudimentary resistive detector was fabricated using mechanically contacted  $\text{UO}_2$ . Despite multiple efforts to parse the measured response, the device did not conclusively demonstrate the ability to detect or discriminate between  $\alpha$  and  $\gamma$  radiation. The potential for neutron radiation detection using hydrothermally synthesized  $\text{UO}_2$  remains to be answered.

## Table of Contents

	Page
Abstract .....	iv
Table of Contents .....	vi
List of Figures .....	viii
List of Tables .....	xv
Acknowledgments.....	xvii
 I. Introduction .....	 1
1.1 Motivation .....	1
1.2 Special Nuclear Material Detection.....	2
1.3 Research Objective and Overview .....	6
 II. Theory .....	 8
2.1 X-ray Fluorescence Spectroscopy .....	8
2.2 X-ray Diffraction .....	10
2.3 Photoemission Spectroscopy .....	12
2.3.1 Photoemission Model.....	12
2.3.2 PES Energy Scheme .....	12
2.3.3 Photoelectron Attenuation Depth & Depth-Resolved PES.....	14
2.3.4 Photoelectric Work Function .....	17
2.3.5 Temperature Dependent XPS & Effective Surface Debye Temperature.....	22
2.3.6 Auger Emission and the Auger Parameter .....	26
2.4 Schottky-Mott Theory .....	28
2.5 Hydrothermal Crystal Growth.....	30
2.6 Stoichiometry and Oxygen Defects .....	35
 III. Crystal Growth and Characterization.....	 39
3.1 Growth and Analysis of UO <sub>2</sub> Crystals.....	39
3.1.1 Phase Study .....	39
3.2 X-ray Diffraction Analysis .....	40
3.2.1 Single-Crystal XRD .....	40
3.2.2 Rocking Curve Measurement .....	40
3.3 PES Analysis .....	43
3.3.1 XPS Confirmation of Stoichiometry.....	43
3.3.2 Auger Parameter Analysis .....	45
 IV. Electronic Characterization of the Crystal Surface .....	 46

4.1 Surface & Subsurface Stoichiometry .....	46
4.1.1 Depth Resolved Chemical Shift (Surface to Core Level Shift) .....	47
4.1.2 Depth Resolved Auger .....	50
4.2 Effective Surface Debye Temperature Measurement.....	52
4.2.1 Debye Experiment .....	52
4.2.2 Debye Analysis .....	55
4.2.3 Debye Summary.....	61
4.3 Work Function Measurements .....	62
4.3.1 Experiment and Analysis .....	63
4.3.2 Reconstruction Kinetics .....	66
4.3.3 Work Function Summary.....	69
4.4 Identification of Cs Contamination by XPS .....	70
4.4.1 Temperature Dependence of Cs Migration.....	70
4.4.2 Temperature Threshold of Cs Diffusion .....	72
V. Contact Study .....	75
5.1 Determination of Candidate Metals for Electrical Contacts .....	75
5.2 Evaluation of Experimental Contacts .....	77
5.2.1 Current-Voltage Measurements .....	78
5.2.2 Capacitance-Voltage Measurement .....	80
5.2.3 Implications of I(V) and C(V) Measurements .....	84
VI. Pulse Discrimination Experiment .....	85
6.1 Motivation and Purpose.....	85
6.2 Experiment .....	85
6.2.1 Detector and Instrumentation Scheme .....	85
6.2.2 Estimation of Detector Background and Expected Signal Parameters .....	87
6.2.3 Initial Results .....	89
6.2.4 Noise Analysis .....	91
6.2.5 Pulse Form Analysis .....	93
6.2.5 Detector Noise & Trigger Scheme.....	94
6.2.6 Source Description and Geometry .....	96
6.2.7 Efficiency Analysis.....	98
6.2.8 Pulse-Shape Parameter Study .....	102
6.3 Implications .....	106
VII. Conclusion.....	108
7.1 Summary of Findings .....	108
7.1.1 Crystal Quality .....	108
7.1.2 Electronic Characteristics .....	109
7.1.3 Potential for Radiation Detection.....	110
7.2 Future Work.....	110
Works Cited .....	112



## List of Figures

	Page
Figure 1. The first 4 shells of electronic states describing a typical high-Z atom. The primary x-rays, identified as $h\nu$ , excite the core electrons into lesser-bound state vacancies. The resulting vacancies are filled in accordance with the selection rules resulting in the emission of secondary x-rays, a.k.a fluorescent or characteristic x-rays, with well-characterized energies. The spectroscopic notation for the energy levels and a representative sampling of allowed x-ray emissions are displayed on the right. Each element can be identified by its characteristic x-rays. ....	10
Figure 2. Incident x-rays are scattered by the planes of a crystal lattice. When the path length difference of parallel beams is an integer multiple of the wavelength, constructive interference occurs. The identification of the angle, $\Theta$ , at which this occurs provides the interplanar spacing of the lattice. ....	11
Figure 3. The energy scheme of photoelectron spectroscopy. XPS and UPS differ primarily in the energy of the photon source. ....	13
Figure 4. The aluminum $K\alpha$ line shown with contributions from both the $K\alpha_1$ and $K\alpha_2$ . ....	14
Figure 5. The angle between the sample and the electron analyzer can be varied to sample either the bulk or surface electronic states. In each of the two cases shown, the attenuation distance is the same but the sample depth changes. ....	17
Figure 6. The relationship between the electrochemical potential of bulk electrons, $\mu$ , as it relates to the local vacuum level, $\varepsilon Vac_0$ , and the theoretical vacuum level at infinity, $\varepsilon vac_\infty$ . ....	18
Figure 7. A binding energy (BE) vs intensity (I) spectrum for (a) the grounded sample and (b) the same sample with an applied bias of V. The fermi edge, $BE = 0$ , is denoted by $a_0$ and $b_0$ . The energy difference between $SEC_a$ and $SEC_b$ (or between $a_0$ and $b_0$ ) is bias voltage V. An applied bias increases the intensity of low energy photoelectrons. ....	20

Figure 8. A nominal PES spectrum showing the Secondary Electron Cutoff (SEC) and linear regression line to determine the SEC energy. ....21

Figure 9. The generation of an Auger electron in atomic oxygen. An x-ray creates a core hole, C1, in the K shell shown in (b) of a ground-state atom depicted in (a). A second hole, C2, is created in an L shell, the electron filling C1 as shown in (c). The Auger emission creates the third hole, C3, shown in (d). The full nomenclature of this emission is O(KL2,3L2,3). The energy difference between L2 and L3 is small and thus the levels are essentially the same energy. All of the emissions involving the KLL levels are referred to collectively as the O(KLL). Figure after [9]. ....27

Figure 10. The energy band diagram of a p-type semiconductor and a metal depicted separately on the left and joined in a junction on the right. The Fermi-levels align and the energy levels bend correspondingly. The energy levels of the vacuum, conduction band, valence band, and Fermi are represented by  $E_{vac}$ ,  $E_{cp}$ ,  $E_{vp}$ , and  $E_f$ . The band gap is denoted as  $E_g$ . The work function of the semiconductor and the metal are depicted as  $\phi_s$  and  $\phi_m$ . The barrier height is  $\phi_{bp}$  as predicted by (49). The electronegativity of the semiconductor is  $X_s$ . Figure after [25]. ....30

Figure 11. The critical point of water is 647 K (374 °C, 705 °F) and 218 atm (22.064 MPa, 3200 psia). ....31

Figure 12. A Bridgeman autoclave on the left showing 4 heater bands and a pressure gauge. On the right is a drawing of the sealed metal ampoule (e) inside the autoclave within which sits a ladder made of wire (c) supporting a seed crystal (b) which is surrounded by a mineralizer solution (d). The nutrient, or feedstock (f) sits at the bottom of the dissolution zone which is kept hotter than the growth zone. The difference in the zone temperatures determines the differential solubility (the growth rate). A convective flow pattern is established which transports dissolved nutrient into the growth zone. ....33

Figure 13. The solubility of  $ThO_2$  in an aqueous CsF mineralizer solution at 25k psia adapted from [28]. The solubility difference as a function of CsF concentration for the same 50° temperature gradient is depicted by a, b, and c. Solubility (i.e. growth rate) is controlled by both the mineralizer concentration and temperature gradient. The same growth rate may be achieved anywhere along a linear solubility line for a given temperature gradient. However, crystal composition may differ based on the competing solubility of impurity species. ....34

Figure 14. The fluorite structure of the $\text{UO}_2$ conventional unit cell. The smaller uranium atoms (blue) are located in the FCC position surrounding the larger oxygen atoms (red) of a simple cubic. Image produced using [29].	35
Figure 15. The single-crystal XRD absolute scan of the $\text{UO}_2$ crystal. The single family of Bragg peaks indicates a single-crystal sample.	41
Figure 16. The rocking curve of the $\text{UO}_2$ -T-29b (111) sample about the Bragg angle of the single peak. The FWHM of $0.4566 \pm 0.0007^\circ$ was determined by a Gaussian fitting.	42
Figure 17. The $\text{U}4f$ spectrum of $\text{UO}_2$ -T-18a. The $\text{Al } K\alpha_{3,4}$ ghost peaks were fitted to remove the effects of the un-monochromated x-ray source.	44
Figure 18. The depth-resolved XPS measurements of the $\text{U}4f$ region from normal ( $0^\circ$ ) to $59^\circ$ . The binding energy shift of the $4f$ core levels indicates an increase in the oxidation state of U. The inefficiently sputtered hemisphere of the round sample was responsible for the increasing contribution of higher uranium oxides to the peak at steep angles and subsequent large binding energy shift.	48
Figure 19. Depth resolved XPS on the $\text{UO}_2$ -T-29a (100) sample. The binding energy shift from minimum to maximum value is 0.11 eV for the $4f_{7/2}$ and 0.14 eV for $4f_{5/2}$ .	49
Figure 20. Depth resolved XPS on the $\text{UO}_2$ -T-29b (111) sample. The binding energy shift from minimum to maximum value is 0.16 eV for the $4f_{7/2}$ and 0.13 eV for $4f_{5/2}$ . The $0^\circ$ measurement was repeated at the end of the experiment and showed a shift to lower energy by 0.06 eV.	49
Figure 21. The angle-dependent U NOV: $4f_{7/2}$ Auger Parameter shown with an uncertainty of $\pm 0.15$ eV. The dashed line, the parameter for $\text{UO}_2$ , and the dotted dashed line, the value for $\text{U}_4\text{O}_9$ , as measured by [36], are depicted as reference points. The surface of the crystal displayed a trend toward hyperstoichiometry.	51

Figure 22. The angle-dependent U  $4f_{7/2}$  Auger Parameter shown with an uncertainty of  $\pm 0.25$  eV. The dashed line, the parameter for  $UO_2$ , and the dotted dashed line, the value for  $U_4O_9$ , as measured by [36], are depicted as reference points. The surface of the crystal displayed hyperstoichiometry.....51

Figure 23. The deconvolved XPS spectrum of the U4f region. The raw XPS data is shown as open circles. The background and peak line shapes are shown as thin lines with the resulting envelope shown as a heavy line.....54

Figure 24. The natural logarithmic ratio of intensities for the uranium peaks as a function of temperature. The reference intensity was the intensity measured at 303 K for both surface annealing conditions. The 623 K annealed surface exhibits the shallowest slope indicating a high effective Debye temperature ( $500 \pm 59$  K) post-transition corresponding to the ( $UO_{2+x} + U_4O_{9-y}$ ) phase. The transition of the crystal surface to the ( $UO_{2+x}$ ) phase is marked by a sharp change in the intensity ratio point near 475 K. The slope post-transition indicates a lower effective Debye temperature ( $165 \pm 21$  K) for ( $UO_{2+x}$ ). .....56

Figure 25. The  $U4f_{7/2}$  centroid energy measured at different temperatures for both annealing conditions. The surface of both samples was hyperstoichiometric at the onset of measurement and reduced with increasing temperature as evidenced by the shift to lower energy. The 623 K annealed sample is closer to the expected value of 380.00 eV for stoichiometric  $UO_2$ . The error bars of  $\pm 0.05$  eV are an artifact of the spectrometer energy calibration.....59

Figure 26. The natural logarithmic ratio of U  $4f_{7/2}$  intensity for both surface preparations on the major axis compared to the linear expansion coefficient,  $\alpha$ , for  $UO_2$  as a function of temperature found in the literature on the minor axis [43]. The change in  $\alpha$  occurs at  $\approx 490$  K which is in good agreement with the observed phase change at 476 K determined by XPS.....60

Figure 27. The work function of the (111) sample was obtained by a linear fitting of the secondary electron cut-off. The initial measurement and a subsequent measurement which yielded the maximum value are depicted along with the respective linear fits. The depicted energy scale is corrected for the photon line width.....64

Figure 28. The time-evolution of the work function for the (111) and (100) $\text{UO}_2$ surfaces. In the figure's inset, an extrapolation of the trend provides an estimate of the initial work function at cessation of sputtering ( $t=0$ ); 5.66 eV (111) and 5.56 eV (100). The maximum values are 6.28 eV (111) and 5.80 eV (100). Error bars of $\pm 0.36$ eV are omitted for clarity. ....	65
Figure 29. The log of the work function change plotted with respect to the log of time for the reconstructing surfaces. ....	68
Figure 30. XPS spectrum of the U4d region using Mg $k\alpha$ radiation on the clean $\text{UO}_2$ surface at 70 °C showing the $\text{U}4d_{3/2}$ and $\text{U}4d_{5/2}$ peaks with the O KLL Auger in the center. The U4d shake-up satellites are also observed. ....	71
Figure 31. XPS spectrum of the U4d region using Mg $k\alpha$ radiation held at 350 °C for several hours showing the $\text{Cs}4d_{3/2}$ and $\text{Cs}d_{5/2}$ peaks along with the U4d and O KLL Auger features. The core U lines are diminished by the Debye effects at elevated temperature which is most striking for the $\text{U}4d_{3/2}$ . ....	72
Figure 32. Ratio of the $\text{U}4d_{5/2} : \text{Cs}4d_{3/2}$ intensity as a function of sample temperature. ....	73
Figure 33. The (100) surface viewed from the $\langle 100 \rangle$ . The oxygen atoms (large spheres) are red, the uranium atoms (small spheres) are blue. The drawing is scaled by ionic radius. The conventional unit cell is illustrated by the nine uranium atoms of the FCC-like (100) in which four oxygen atoms are located. The sub-cell is offset by $45^\circ$ . ....	76
Figure 34. The $I(V)$ response of the $\text{Ag}/\text{UO}_2/\text{GaIn}$ device. The response was generally Ohmic with a larger rectification in the forward bias. The absolute value of the reverse bias data is displayed alongside the forward bias data for comparison. A reference line representing a $714.3 \Omega$ is displayed for reference. ....	79
Figure 35. The $I(V)$ measurements of the $\text{W}/\text{UO}_2/\text{W}$ devices and the $\text{Ag}/\text{UO}_2/\text{GaIn}$ device. The response of the $\text{Ag}/\text{UO}_2/\text{GaIn}$ device is an order of magnitude higher but has a similar response curve to the T11b $\text{W}/\text{UO}_2/\text{W}$ device. The LEFT vertical axis corresponds to the T29a sample. The T11 sample current is on the RIGHT side vertical axis. ....	80

Figure 36. The energy level diagram for an abrupt metal to n-type semiconductor junction adapted from [18].	81
Figure 37. A plot of $(A/C)^2$ vs V. The measurement started and ended at 0 V, scanning out to $\pm 10$ V twice, which produces multiple values for the same bias.	83
Figure 38. A magnified image of the $UO_2$ crystal with mechanical tungsten contacts applied.	86
Figure 39. Diagram of the pulse detection instrumentation scheme.	87
Figure 40. Results of the initial a) 24-hour background/internal noise measurement and b) 24-hour $^{241}\text{Am}$ signal response are pictured. During the background acquisition, only 7 counts were obtained, whereas 67 counts were acquired during the source exposure time period.	90
Figure 41. A typical pulse-shape attributed to an alpha-particle deposition in the detector. The zero-time point in this plot is determined by the trigger setting of the oscilloscope which is arbitrary.	93
Figure 42. Oscilloscope traces typical of events captured by the fall-time trigger. The upper left trace is considered a pulse. The upper right is pulse-like but excluded by the algorithm due to insufficiently long tail and poor exponential fit. The bottom left trace is excluded by the absence of a defined pulse peak. The bottom right trace is excluded based on a lack of defined pulse peak and poor exponential tail fitting.	96
Figure 43. The experimental source and detector geometry.	97
Figure 44. Placement of the $^{241}\text{Am}$ sources (left) and a $\gamma$ -ray source (right).	98
Figure 45. A pulse height vs. time constant histogram summarizing the post-processed detector background, response to $^{241}\text{Am}$ , $^{241}\text{Am}$ with paper filter, and $^{60}\text{Co}$ at 143 mm. The red pixels are of the highest intensity for each histogram with a value indicated by the color bar.	103

Figure 46. A pulse height vs. time constant histogram summarizing the post-processed detector background, response to  $^{137}\text{Cs}$  at two different distances as well as  $^{60}\text{Co}$ . The red pixels are of the highest intensity for each histogram with a value indicated by the color bar. ....104

Figure 47. A pulse height vs. time constant histogram summarizing the post-processed detector background, response to  $^{55}\text{Fe}$  at three different distances. The red pixels are of the highest intensity for each histogram with a value indicated by the color bar.....105

Figure 48. Results of the parameter study using 63% of the identified pulses. The scheme cannot separate the radiation types at this level. ....106

## List of Tables

	Page
Table 1. The primary decay modes, half-lives, and spontaneous neutron emission rate of selected nuclides. ....	2
Table 2. Prompt energy distribution of $^{235}\text{U}$ fission .....	5
Table 3. The XPS spectral summary of UO <sub>2</sub> -T-18a and comparative spectra from high-resolution XPS on UO <sub>x</sub> [34]. The measured values for T18a are $\pm 0.03$ eV. The absence of comparative data indicates the feature either cannot be resolved, ‘- -’, or does not exist, ‘n/a’ .....	43
Table 4. The binding energies of the U4f peaks as a function of oxidation state. ....	46
Table 5. A nominal deconvolution of the U4f XPS spectral region at 303 K. The values shown are from a single measurement. Major peaks were well-supported by an integrated intensity in excess of a million counts.....	55
Table 6. Summary of the effective Debye temperature computation from the temperature-dependent, photoelectric intensity derived Debye-Waller factor of the sample annealed at 298 K for 12 hours. The U5f valence state does not follow the Debye-Waller relationship and is presented for comparison.....	57
Table 7. Summary of the effective Debye temperature computation from the temperature-dependent, photoelectric intensity derived Debye-Waller factor of the sample annealed at 623 K for 12 hours. ....	57
Table 8. Summary of the photoelectron kinetic energy, attenuation length in a UO <sub>2</sub> lattice (TPP-2M, 99% attenuation), and measured transition temperature of the U photopeaks. The attenuation length illustrates the surface sensitivity of the measurement. ....	58
Table 9. Candidate metals for electrical contacts. The parenthetical value following the contact type in the two rightmost columns indicates the order of best agreement. ....	77



Table 10. The primary $^{238}\text{U}$ decay chain contributions to the crystal background. ....	88
Table 11. Summary of sources. The $^{241}\text{Am}$ source was used with and without shielding for $\alpha$ particles. ....	98
Table 12. Mono-energetic photon attenuation in the $\text{UO}_2$ crystal. ....	100
Table 13. Summary of the data collected using different sources and source to detector distances. Numbers in <i>red</i> indicate the data was collected very near the maximum collection rate of the oscilloscope and is potentially inaccurate. ....	101

## **Acknowledgments**

Many thanks to my family, friends, and colleagues without whom I would not have been able to gather and analyze the data critical to this research. I owe a great deal to the faculty, staff, and post-doctoral researchers of AFIT for making this research possible. I am especially indebted to the AFRL crystal growth team for their tireless efforts to overcome the many challenges in producing single-crystal uranium dioxide samples.

Chris Young

# **EVALUATION OF HYDROTHERMALLY SYNTHESIZED URANIUM OXIDE FOR NOVEL SEMICONDUCTOR APPLICATIONS**

## **I. Introduction**

### **1.1 Motivation**

Tracking and identification of radiation sources in the age of nuclear proliferation and well-resourced non-state actors is a top national priority. The successful detection and interdiction of nuclear material traveling among the substantial volume of imported goods to the US remains the primary task of the Domestic Nuclear Detection Office (DNDO). To this end, great emphasis has been placed on developing better detection systems for the use in homeland security radiation detectors. In the age of high-tech, miniaturized devices, the end-user expects a radiation detector to be compact, portable, consume little power, and provide rich detail from the measured spectrum. However, successful radiation detection favors large detector volumes and long count intervals. Within this trade-space, the employment of more efficient detector materials, especially neutron sensitive materials, supports the end-user's expectations. One approach to counter-proliferation on a broad scale is the wide-spread placement of many small detectors, which can be combined with data mining to provide details about movements of radiation sources. To achieve this, detectors must be small, simple, low power consumers, and efficient at detection of the radiation of interest while minimizing the effect of natural and man-made background. With the exception of detection efficiency, all of these are hallmarks of the solid-state motif.

## 1.2 Special Nuclear Material Detection

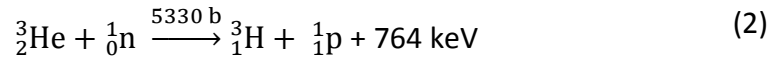
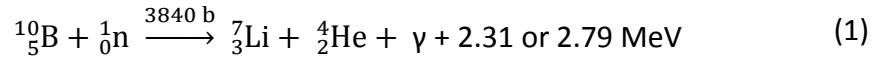
The detection of special nuclear material, SNM, most directly relates to the identification of nuclear weapon materials by remote means. Defined by Title I of the Atomic Energy Act of 1954, SNM includes Pu, U-233, and U enriched in the isotopes U-233 or U-235 [1]. Such materials are long-lived and decay by  $\alpha$ -emission. By definition, they are fissionable and undergo spontaneous fission, emitting neutrons in the process. SNM also emits gamma-rays by virtue of decay de-excitation, but a neutron signature is unambiguous, harder to mask, and almost always associated with SNM. In addition, terrestrial gamma-ray background sources represent a potential detection complication. Table 1 summarizes the spontaneous neutron emission rates of select nuclides. Because the nuclides of Pu are difficult to separate, any fraction of Pu-240 in a Pu mass will enhance neutron emission.

Table 1. The primary decay modes, half-lives, and spontaneous neutron emission rate of selected nuclides.

	Half-Life [year]	Primary Decay Mode	Spontaneous Fission Neutron Emission Rate [n / 100 g s]*
<sup>239</sup> Pu	24110	$\alpha$ Emission	2
<sup>240</sup> Pu	6564	$\alpha$ Emission	138359
<sup>241</sup> Pu	14.4	$\alpha$ Emission	23
<sup>235</sup> U	7.04E+08	$\alpha$ Emission	0.14
<sup>238</sup> U	4.50E+09	$\alpha$ Emission	1.5

\* Emission rate based upon an average of 2.89 neutrons per Plutonium fission and 2.44 neutrons per Uranium fission [2].

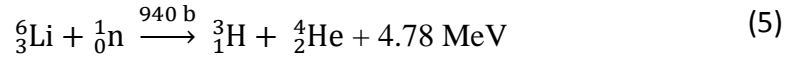
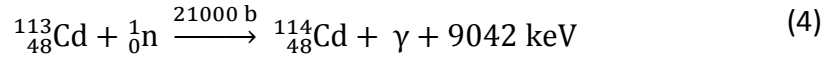
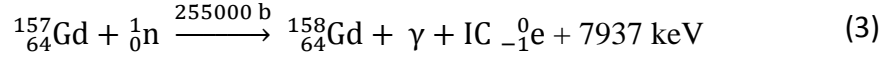
Neutron detectors exploit specific nuclear reactions for detection since neutrons cannot be detected directly in a practical system. In such a reaction, the products must include energetic particles which produce charged particles capable of ionizing matter. Two of the most common and well-documented reactions employ  $\text{BF}_3$  or  $^3\text{He}$  gases with reactions depicted (1) and (2) [3].



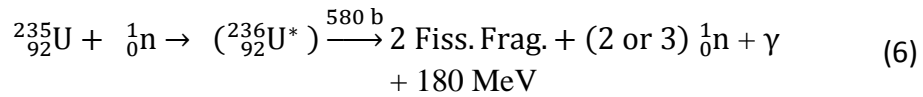
Depicted above each reaction is the thermal neutron cross-section, or probability of interaction in area units. The reaction energy, depicted as a product, is often referred to as the ‘Q’ value which is distributed among the reaction products. The high cross section for the  $^3\text{He}$  reaction and its availability as a by-product from nuclear weapon material production has made it an attractive detection medium for portal neutrons for decades. Unfortunately, due to recent low production rates  $^3\text{He}$  detectors have become costly and a national effort to find a suitable replacement is underway [4].

Semi-conducting neutron detectors using a conversion material are a potential alternative based upon modern manufacturing techniques and device fabrication methods. These detectors make use of the reaction products from neutron interactions in the conversion material which introduces ionization events within the depletion region of the device junction. This potentially provides a signal that can be substantive compared to saturation currents across the junction interface, assuming efficient charge collection in a

small volume. Typical reactions employed in a conversion layer material are listed in (3), (4), and (5).



An efficient detector design employs a reaction with both a large neutron fission cross-section and a large ‘Q’ value which can be efficiently collected electronically. Materials containing Gd are attractive based on the cross-section, but the detectable internal-conversion electron possesses such a small fraction of the ‘Q’ value that charge collection limits its efficiency. The  ${}^6\text{Li}$  reaction is nearly the reverse; the cross-section is lower but the ‘Q’ value of 4.78 MeV is distributed among large particles which produce significant ionization. By comparison, for uranium, and especially in the case of  $^{235}\text{U}$ , the fission interaction is shown in (6). Not only is the cross-section relatively high, but the ‘Q’ value is over 30 times larger than for  ${}^6\text{Li}$ .



The ‘Q’ value energy manifests primarily in the form of fission fragment kinetic energy shown in Table 2 [2]. This is valuable, given that the fission fragments are highly charged and have a short track length. Therefore, fission interactions occurring inside the active detector volume within a crystal made with uranium have a high probability of producing secondary ionization which is the electronic signal indicating detection.

Table 2. Prompt energy distribution of  $^{235}\text{U}$  fission

Fission Fragment Energy	168
Neutron Energy	5
Prompt Gamma-ray Energy	7
Total Prompt Energy	180 MeV

The theory thus far has ignored the vast engineering challenge of developing electronically viable uranium materials and efficiently converting the ionization energy into a detected signal. The fabrication of a high-quality uranium-based diode is one path to efficient charge collection. An efficient diode will have a large depletion region, sufficient conductivity for charge collection, and an efficient mechanism to produce charge carriers within the depletion region; the latter being an intrinsic property of uranium for reasons stated previously. Due to the difficulty in making suitable diodes that incorporate uranium, the engineering approach has been to create a diode of electronically suitable material upon which is placed a neutron reactive conversion layer as previously stated [5]. This approach has inherent efficiency losses. If a diode has a suitable electronic structure, conduction parameters, and is made from a solid-state material containing uranium, such a diode would be an intrinsic detector.

Until recently, a lack of suitable  $\text{UO}_2$  has limited its semiconductor potential [6] [7] [8]. Previous semiconductor-focused research utilized poor quality  $\text{UO}_2$  crystal material grown by melt processes which are known to produce defected crystals [7].

### 1.3 Research Objective and Overview

The primary objective of this research was to characterize single crystal samples of  $\text{UO}_2$  developed via hydrothermal growth, and to assess their potential for development of radiation detection devices. In pursuit of this ultimate goal, the systematic study of hydrothermally grown  $\text{UO}_2$  crystals was undertaken to specifically address the following questions.

- (1) Does the hydrothermal growth process produce single-crystal  $\text{UO}_2$  with sufficient quality, purity, and stoichiometry, to be considered for electronic material?
- (2) What are the electronic characteristics of the crystal and crystal surface?
- (3) Do the crystals have the potential for a radiation detection device?

Several crystals were synthesized in an iterative process in which the growth conditions were refined by elemental analysis feedback. The use of x-ray fluorescence (XRF) and single-crystal x-ray diffraction (SCXRD) provided purity and structure data to confirm the formation of nearly stoichiometric  $\text{UO}_2$ . An XRD rocking curve confirmed long-range crystal order. The crystal surface was characterized by photoemission spectroscopy (PES) utilizing both temperature and depth-resolved techniques to confirm the surface was nearly stoichiometric  $\text{UO}_2$ . Two effective surface Debye temperatures were identified, separated by a lattice stiffening transition at a phase transition which has implications for crystal purification, crystal doping, and dopant migration. The photoelectric work function of two crystal faces, (111) and (100), was measured and used to determine the electronic stability of the surfaces. The measurements were used to identify potential metals for application of Ohmic and Schottky contacts. The I(V) characteristics of both a mechanical W- $\text{UO}_2$  junction and surface-applied Ag- $\text{UO}_2$ -GaIn



junction device were measured in confirmation of the theory. In addition,  $I(V)$  and  $C(V)$  measurements of the Ag-UO<sub>2</sub>-GaIn junction inferred that the material was n-type with a p-type junction, an unexpected result, which is analyzed further in the document. A resistive device fabricated using mechanical W-UO<sub>2</sub> contacts was evaluated as a radiation detector with mixed results.

## II. Theory

This section introduces relevant theory applicable to the measurement techniques employed in this research as well as the nature of uranium oxide. During the iterative development of the growth process, x-ray fluorescence and x-ray diffraction measurements provided information as to the composition and structure of the crystals and are presented first. Photoemission spectroscopy, in its various forms, provided electronic structure, elemental composition, and insight into the chemical environment of the elements of the crystal. Basic semiconductor theory is presented along with the physics of hydrothermal crystal growth. The theory of defect formation in uranium oxide, specifically the formation of oxygen defects which are largely responsible for the electronic and physical properties of the material, is also presented.

### 2.1 X-ray Fluorescence Spectroscopy

X-ray fluorescence spectroscopy (XRF) leverages the unique electronic energy distribution of each element to provide elemental composition information. An XRF system uses a primary x-ray source to excite or ionize the atoms within a sample. The excited atomic states relax and emit characteristic, fluorescent x-rays in accordance with spectroscopic selection rules.

Figure 1 depicts the electronic states of a typical high-Z atom. The states are characterized by combinations of the principle quantum number,  $n$ , the angular momentum quantum number  $\ell$ , and the spin-orbit coupling,  $j$ . Each energy group is identified by a shell designation which can be enumerated further for convenience. The shells are designated as K, L, M, N, and O which correspond to the principle quantum

numbers 1, 2, 3, 4, and 5. The source x-rays, usually generated with an uncommon metal anode such as rhodium, excite the target material electrons into unoccupied states provided the energy of the primary x-ray exceeds the binding energy of the initial state [9]. The vacancies are filled by electrons from lesser-bound states in general accordance with (7)-(9), the selection rules, which govern the change of principle quantum number,  $\Delta n$ , angular momentum quantum number,  $\Delta l$ , and the total momentum quantum number,  $\Delta j$ , for the transitions [9].

$$\Delta n = \geq 1 \quad (7)$$

$$\Delta j = 0, \pm 1 \quad (8)$$

$$\Delta l = 0, \pm 1 \quad (9)$$

The energy difference between the initial and final state is emitted as a secondary x-ray photon which gives rise to the term fluorescence. The secondary x-rays and their relative intensities are well-documented and the spectrum can provide both the identity and relative abundance of each element in the sample with a detection threshold under optimal conditions of 1 ppm [9] [10]. XRF measurements are nearly independent of elemental bonding environment and therefore provide an elemental analysis of the crystal samples investigated in this research.

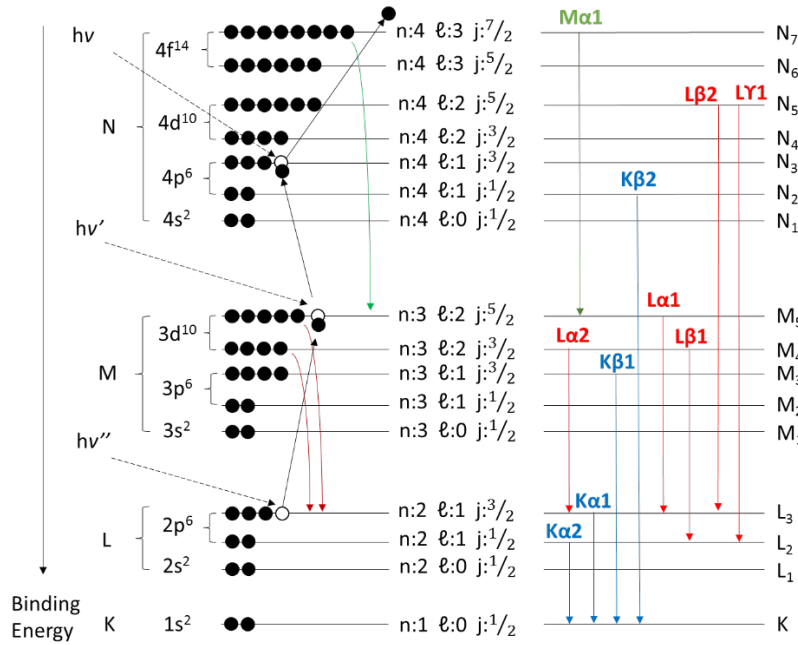


Figure 1. The first 4 shells of electronic states describing a typical high-Z atom. The primary x-rays, identified as  $h\nu$ , excite the core electrons into lesser-bound state vacancies. The resulting vacancies are filled in accordance with the selection rules resulting in the emission of secondary x-rays, a.k.a fluorescent or characteristic x-rays, with well-characterized energies. The spectroscopic notation for the energy levels and a representative sampling of allowed x-ray emissions are displayed on the right. Each element can be identified by its characteristic x-rays.

## 2.2 X-ray Diffraction

A crystal is a matrix of regularly spaced atomic planes. Interrogation of the matrix by parallel x-ray beams as depicted in Figure 2 will yield a constructively scattered interference pattern in accordance with Bragg's law of diffraction given by (10) in which  $n$  is an integer and  $\lambda$  is the x-ray wavelength.

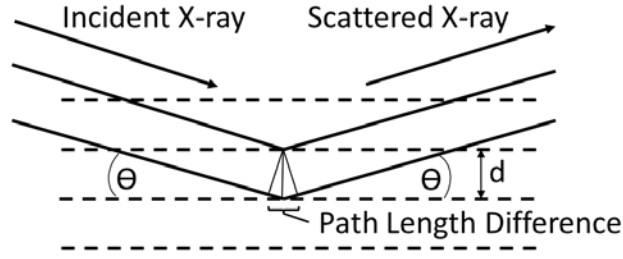


Figure 2. Incident x-rays are scattered by the planes of a crystal lattice. When the path length difference of parallel beams is an integer multiple of the wavelength, constructive interference occurs. The identification of the angle,  $\Theta$ , at which this occurs provides the interplanar spacing of the lattice.

The interplanar spacing,  $d$ , is related to the angle of x-ray incidence by (11).

$$\text{Path Length Difference} = n \lambda \quad (10)$$

For a fixed x-ray energy, the crystal can be interrogated through a spectrum of angles which will yield the interplanar spacing. This is related to the Miller indices of the (cubic) crystal by (12) [9].

$$2 d \sin \theta = n \lambda \quad (11)$$

When this is generalized to three dimensions, i.e. single-crystal x-ray diffraction, it can provide the lattice constants.

$$d_{hkl} = \frac{a}{\sqrt{h^2 + k^2 + l^2}} \quad (12)$$

As an example, consider a  $\text{UO}_2$  (111) Bragg peak angle of  $14.1^\circ$  measured using a  $\text{Cu } \alpha_1$  radiation source with a wavelength of  $1.5406 \text{ \AA}$ . The resulting interplanar distance,  $d$ ,

computed from (11) , is 3.13 Å. The lattice parameter is then computed by (12) to be 5.42 Å with the assignment of the Miller indices (h,k,l) to (111).

## **2.3 Photoemission Spectroscopy**

Photoemission spectroscopy measures the kinetic energy of photoelectrons generated in a sample from an excitation source, usually an x-ray or UV photon. The measured photoelectron energy spectrum contains information about the chemical environment of the emitting atoms. This powerful tool can determine both the identity and chemical state or states of the constituent atomic species within the sample.

### **2.3.1 Photoemission Model**

A 3-step model describes the basic process of photoelectron generation and energy measurement [11]. In the first step, photons of known energy are directed into a sample which generates photoelectrons via the photoelectric effect. In step 2, the photoelectrons move through the sample to the surface. In step 3, photoelectrons with sufficient energy escape the surface into the vacuum and are collected by an electron analyzer. The kinetic energy of the electron, as measured by the analyzer, is directly related to the energy of the bound state.

### **2.3.2 PES Energy Scheme**

X-ray photoemission and ultraviolet photoemission, commonly abbreviated XPS and UPS, differ only in the energy of the excitation photon and photoelectric cross-sections. The energy level scheme of each process is similar and depicted in Figure 3 which assumes the sample is grounded to the instrument so that the Fermi levels are

aligned. The photoelectron is generated by a finite photon energy,  $h\nu$ , which is the maximum kinetic energy,  $KE$ , of a detected photoelectron. To first-order, the kinetic energy of the electron is the difference between the photon energy and the binding energy of the electronic state. However, as the photoelectron approaches the sample surface, it must overcome a surface potential as it transits to the vacuum.

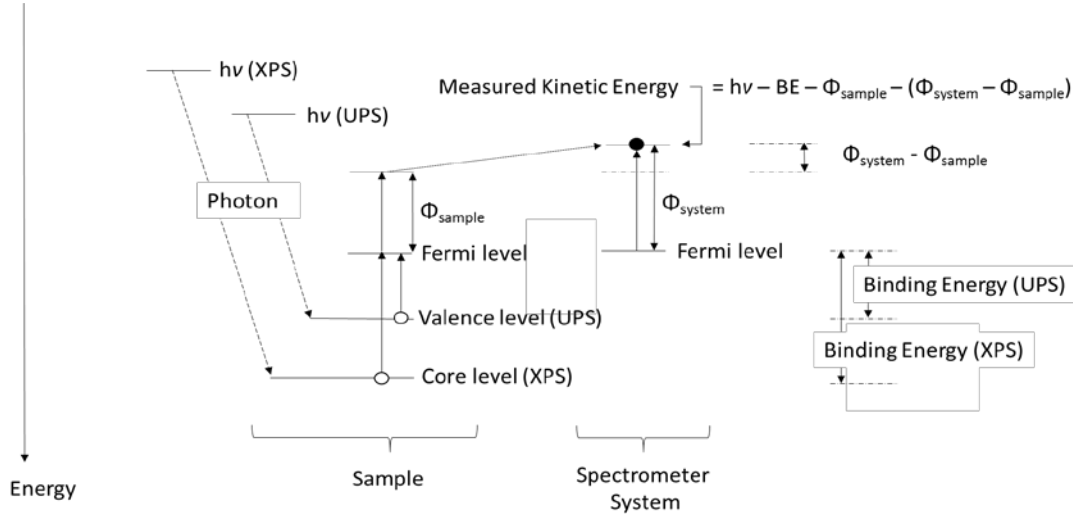


Figure 3. The energy scheme of photoelectron spectroscopy. XPS and UPS differ primarily in the energy of the photon source.

This surface potential is known as the sample work function,  $\phi_{\text{sample}}$ , which is strongly influenced by surface morphology and crystal orientation. An additional amount of energy is lost to the spectrometer and its surroundings. This is called the system work function,  $\phi_{\text{system}}$ . Following the energy balance of Figure 3, the measured  $KE$  is described by (13).

$$KE = h\nu - BE - \phi_{\text{sample}} - (\phi_{\text{system}} - \phi_{\text{sample}}) \quad (13)$$

The  $\phi_{\text{sample}}$  cancels and the  $BE$  is described by (14).

$$BE = h\nu - KE - \phi_{system} \quad (14)$$

The Al or Mg K $\alpha$  lines of 1486.6 and 1253.6 eV respectively are the most common x-ray sources for XPS [11]. A He gas discharge lamp is a common UPS source which has a He1 $\alpha$  line of 21.2 eV. The aluminum K $\alpha$  energy has a line width, or full width at half maximum (FWHM), of 0.85 eV from the unresolved contributions of the K $\alpha_1$  and K $\alpha_2$  lines which differ in centroid energies by 0.43 eV [12]. The convolved K $\alpha$  centroid energy is 1486.60 eV which is shown in Figure 4.

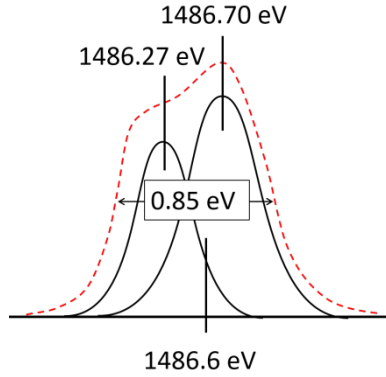


Figure 4. The aluminum K $\alpha$  line shown with contributions from both the K $\alpha_1$  and K $\alpha_2$ .

### 2.3.3 Photoelectron Attenuation Depth & Depth-Resolved PES

The penetration depth of the excitation photon is computed by (15). It relates the photon intensity,  $I$ , to the initial photon intensity,  $I_0$ , which decays along a distance,  $d$ , according to the mass attenuation coefficient,  $\frac{\mu}{\rho}$ , and the sample density,  $\rho$ . It is common to define attenuation as  $1/e$ ,  $\approx 0.3679$ , the condition at which 63% of the x-ray photons are absorbed.



$$I = I_0 e^{-\frac{\mu}{\rho} \rho d} \quad (15)$$

Using a single attenuation coefficient,  $\mu/\rho$ , to approximate the interaction of the x-ray photon in the crystal with a density,  $\rho$ , of 11 g/cm<sup>3</sup>, a 1480 eV photon is attenuated in 492 unit cell lengths of 5.47 Å, a 21 eV photon is attenuated in 150 unit cells. The x-ray attenuation distances are over 10 times that of the photoelectrons and do not represent the information depth of PES. The photoelectron attenuation distance is described by (16) where  $d$  is now the photoelectron travel distance and  $\lambda_i$  is the inelastic mean free path, or IMFP, of the photoelectron.

$$I = I_0 e^{-d/\lambda_i} \quad (16)$$

The previous definition of 63% attenuation yields  $d = \lambda_i$ . An alternate definition of 95% attenuation yields  $d = 3 \lambda_i$ . The IMFP can be obtained by the empirical relation of Tanuma, Powell, and Penn known as TPP2M which is an empirical fit given by (17) through (23) [11] [13]. Using this relationship, the IMFP is a function of the electron energy in eV,  $E$ , the free electron plasmon energy,  $E_p$ , the material density (in g/cc),  $\rho$ , the number of valence electrons per molecule,  $N_v$ , the band gap energy,  $E_g$ , (in eV) and the molecular weight,  $M$ .

$$\lambda_i = \frac{E}{\left(E_p^2 \left[ \beta \ln(\gamma E) - \left(\frac{C}{E}\right) + \left(\frac{D}{E^2}\right) \right] \right)} \quad (17)$$

$$\beta = -0.0216 + \frac{0.944}{\sqrt{E_p^2 + E_g^2}} + 7.39 \times 10^{-4} \rho \quad (18)$$

$$\gamma = 0.191 \rho^{-0.50} \quad (19)$$

$$C = 1.97 - 0.91 U \quad (20)$$

$$D = 53.4 - 20.8 U \quad (21)$$

$$U = \frac{N_v}{M} = \frac{E_p^2}{829.4} \quad (22)$$

$$E_p = 28.8 \sqrt{\frac{N_v}{M}} \quad (23)$$

Using the appropriate parameters for  $\text{UO}_2$ , a photoelectron with 1480 eV of kinetic energy has an IMFP of about 20 Å. If the more restrictive definition of 95% attenuation is used, the distance is 60 Å. Using the greater distance, the path length equates to only 11 unit cells. A 21.2 eV photoelectron is attenuated in 2.4 Å (95% attenuation). This is less than ½ of a unit cell. The TPP2M approximation is less accurate in the low-energy regime, but it is clear that the limiting sample depth is determined by photoelectron attenuation not photon penetration.

XPS can be used to differentiate between the surface and sub-surface electronic states by varying the angle between the sample surface and the electron analyzer. As depicted in Figure 5, placing the analyzer normal to the surface provides the maximum sampling depth. A steeper angle, achieved by moving the electron analyzer or tilting the sample, will preferentially select surface generated photoelectrons.

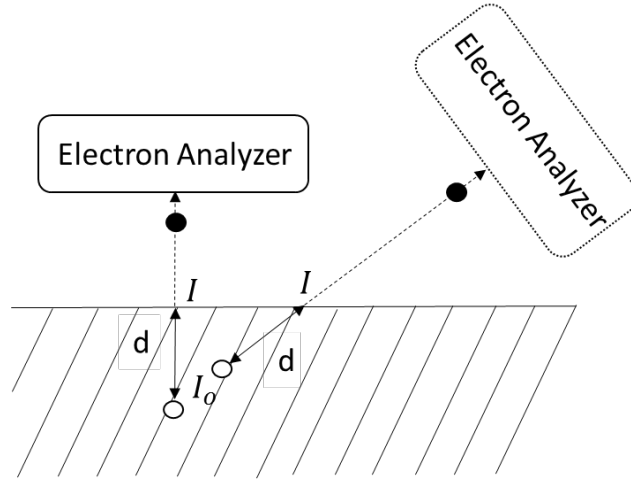


Figure 5. The angle between the sample and the electron analyzer can be varied to sample either the bulk or surface electronic states. In each of the two cases shown, the attenuation distance is the same but the sample depth changes.

#### 2.3.4 Photoelectric Work Function

Photoelectron spectroscopy is surface sensitive and is well-suited to the determination of a sample's surface work function,  $\Phi$ , defined as the minimum thermodynamic work required to liberate an electron from the Fermi level to the vacuum level [14]. In the context of photoemission, a measured work function is referenced to the least-bound electron density of states (DOS) which, for a conductor, is degenerate with the Fermi level [15]. In the case of a semi-conductor with a negligible DOS at the Fermi level, a photoemission measurement will reference the valence band maximum. The term 'photoelectric work function',  $\Phi_{PES}$ , is used to unambiguously describe the work function measured by the photoemission process.

A photoelectron generated by an excitation photon may transport beyond the surface of the crystal face into the vacuum. When the electron travels a distance beyond the surface of the material to the extent that the surface no longer influences the

electrostatic potential energy, the electron has achieved the local vacuum level which is defined as a near-zero potential energy state,  $\varepsilon_{vac}^0$ . The local vacuum level is not an absolute energy state and can vary among surfaces of differing crystal orientations [14] [16] [17]. It is this variation that makes the work function sensitive to crystal orientation and surface morphology. A true zero potential requires an infinite separation of the electron from the surface; i.e. the vacuum level at infinity,  $\varepsilon_{vac}^\infty$ . The work function, in terms of potential, is the difference between the electrochemical potential in the bulk crystal and the local vacuum level [14]. Figure 6 depicts the vacuum and Fermi energy levels in which the electrochemical potential of the electrons in the crystal bulk,  $\bar{\mu}$ , is defined by (24) where  $q$  is the elementary charge [14].

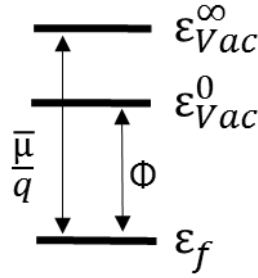


Figure 6. The relationship between the electrochemical potential of bulk electrons,  $\bar{\mu}$ , as it relates to the local vacuum level,  $\varepsilon_{vac}^0$ , and the theoretical vacuum level at infinity,  $\varepsilon_{vac}^\infty$ .

$$\bar{\mu} = q\varepsilon_{vac}^\infty - q\varepsilon_f \quad (24)$$

$$q\Phi = q[ (\varepsilon_{vac}^\infty - \varepsilon_f) - (\varepsilon_{vac}^\infty - \varepsilon_{vac}^0) ] \quad (25)$$

Taking  $\varepsilon_{vac}^\infty$  as the zero energy reference, (25) defines  $\Phi$  in terms of the vacuum levels which yields (26) upon simplification. Restated in terms of energy levels, (27) is

the functional form most often found in the literature describing the work function [18] [14] [15].

$$-q\Phi = q\varepsilon_f - q\varepsilon_{Vac}^0 \quad (26)$$

$$\Phi = \varepsilon_{Vac}^0 - \varepsilon_f \quad (27)$$

A photoemission spectrometer cannot detect electrons with an energy below  $\varepsilon_{Vac}^0$  which gives rise to a photoemission spectral feature known as the secondary electron cutoff (SEC).

The SEC represents the threshold energy of detection and photoelectrons of energy less than  $\Phi$  do not escape the surface of the crystal. From a practical stand-point, it is difficult for the spectrometer to detect electrons at such low energies and the signal intensity is increased by application of bias,  $V$ , between the sample and the spectrometer such that the emitted photoelectrons have an additional kinetic energy ( $KE$ ) determined by  $V$ . This has the effect of shifting the energy spectrum to lower binding energies ( $BE$ ) by the magnitude of  $V$ . Graphically, this is shown by Figure 7 which presents the SEC of a grounded sample as well as one shifted by  $V$ . The biased sample also has a more intense signal near the SEC. The maximum binding energy,  $BE_{max}$ , given by (29) is determined by (28) with  $KE = 0$ .

$$BE = h\nu - KE - \phi_{Spectrometer} \quad (28)$$

$$BE_{max} = h\nu - \phi_{Spectrometer} \quad (29)$$

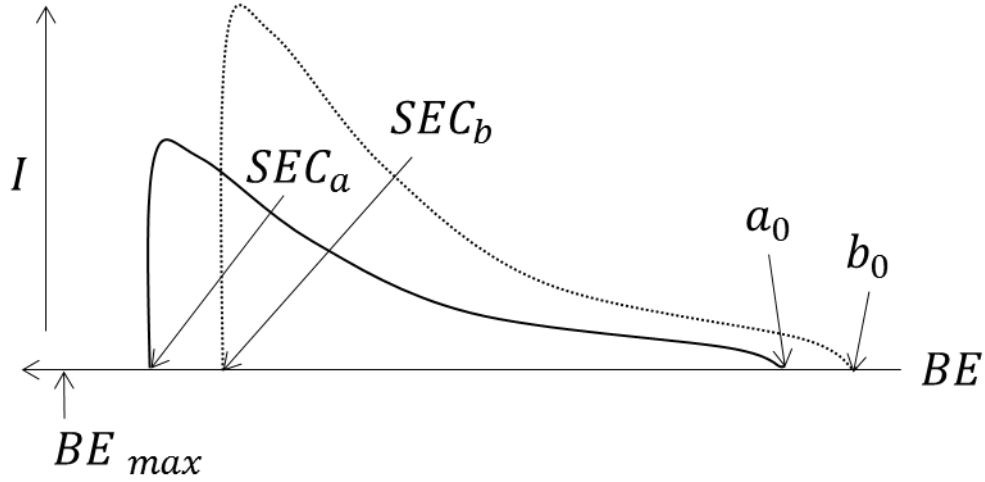


Figure 7. A binding energy (BE) vs intensity (I) spectrum for (a) the grounded sample and (b) the same sample with an applied bias of  $V$ . The fermi edge,  $BE = 0$ , is denoted by  $a_0$  and  $b_0$ . The energy difference between  $SEC_a$  and  $SEC_b$  (or between  $a_0$  and  $b_0$ ) is bias voltage  $V$ . An applied bias increases the intensity of low energy photoelectrons.

The difference between  $BE_{max}$  and the SEC is  $\Phi_{PES}$  shown as (30) in which the first two terms on the right represent  $BE_{max}$ .

$$\Phi_{PES} = hv - \phi_{Spectrometer} - SEC - V \quad (30)$$

Most metals have work functions around 2-5 eV which places the kinetic energy of the SEC below 10 eV for which the inelastic mean free path is on the order of a few angstroms. The photoelectrons collected for work function measurements originate at or very near the crystal surface.

The work function is determined from the energy of the SEC, as depicted in Figure 8. If the spectrum was an ideal step-function, a simple vertical line would intercept the 0 intensity mark indicating the energy of the SEC. Deviation from such a step-function can be attributed to several factors to include electron emission from a

lower work function material into the instrument's field-of-view, an inhomogeneous sample surface, excitation photon linewidth, and excitation photon intensity. The intercept at zero-ordinate of the linear signal edge fitting determines the SEC energy which is depicted by the dashed line in Figure 8.

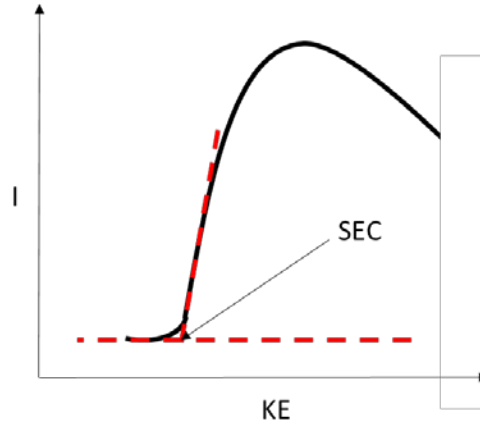


Figure 8. A nominal PES spectrum showing the Secondary Electron Cutoff (SEC) and linear regression line to determine the SEC energy.

Since the SEC is a minimum energy threshold, the measured SEC must be corrected by the portion of the photon linewidth greater than the centroid energy. This correction,  $\Delta$ , is one half of the full-width-at-half-maximum (FWHM) or 0.43 eV. This modification of (30) is shown as (31) which is now the complete expression for  $\Phi_{PES}$ .

$$\Phi_{PES} = h\nu - \phi_{Spectrometer} - SEC - V + \Delta \quad (31)$$

The expression given by (31) suggests a straightforward propagation of error by (32); a combination of the uncertainties of the excitation source energy, spectrometer calibration, SEC fit, and supplied sample bias.

$$\sigma_{\Phi_{PES}} = \sqrt{\sigma_{hv}^2 + \sigma_{spectrometer}^2 + \sigma_{SEC}^2 + \sigma_V^2} \quad (32)$$

The uncertainty of a work function measurement is most strongly influenced by the excitation photon linewidth. The use of an Al  $\alpha$  x-ray source provides a broadening uncertainty of 0.36 eV. The use of an ultra-violet source is generally preferred; the linewidth of the commonly used He-I line is 0.01 eV.

### 2.3.5 Temperature Dependent XPS & Effective Surface Debye Temperature

The heat capacity of a solid in the high temperature regime was modeled by Dulong and Petit as (33) in which the heat capacity at constant volume is  $C_V$ , with internal energy as  $E$ , the absolute temperature as  $T$ , Boltzman's constant as  $k_b$ , and the number of atoms in the solid as  $N$  [19]. The classic model is well-known and appropriate for the high-temperature regime in which it properly describes experimental data [20]. Debye's model, given in (34), more accurately predicts the heat capacity of a solid, especially in the low-temperature regime. The Debye temperature is depicted here as  $\Theta$  and defined by (35). For  $T > \Theta$ , (34) predicts the classical heat capacity of (33) which leads to a definition of  $\Theta$ ; the temperature at which the Debye model obeys (33) [19].

$$C_V = \left( \frac{\partial E}{\partial T} \right)_V = 3Nk_b \quad (33)$$

$$C_V = \left( \frac{\partial E}{\partial T} \right)_V = 9Nk_b \left( \frac{T}{\Theta} \right)^3 \int_0^{\Theta/T} dx \frac{x^4 e^x}{(e^x - 1)^2} \quad (34)$$

$$\Theta = \frac{\hbar v}{k_b} \left( \frac{6\pi^2 N}{V} \right)^{1/3} \quad (35)$$



A first-order description of this phenomenon assumes an isotropic lattice of spacing  $a_0$ . The Debye temperature describes the point at which the phonon wavelength exceeds  $a_0$ . Below this temperature, the thermodynamics of the material are described by collective lattice vibration and the phonons are of a wavelength  $> a_0$  which couple readily. At temperatures above  $\Theta$ , phonon wavelengths are smaller than  $a_0$  and independent thermal lattice vibration dominates the material behavior. Photoelectrons generated in a crystal lattice can couple with the phonon modes of the vibrating nuclei and scatter [11]. It follows that the intensity of a photoelectron spectrum should decrease as the temperature of the sample is increased. Hufner describes the number of atoms that contribute to a photoemission signal as (36).

$$N(E, \hbar\omega) \propto |\sigma^2| \left( e^{-\Delta k^2 U_0^2} \sum_{\mathbf{G}} \delta(\Delta \mathbf{k} - \mathbf{G}) + N(1 - e^{-\Delta k^2 U_0^2}) \right) \quad (36)$$

In this expression,  $\sigma$  is the photoabsorption cross-section,  $E$  is the electron energy,  $\hbar\omega$  is the photon energy,  $\Delta \mathbf{k}$  is the electron wave vector transfer,  $\mathbf{G}$  is the reciprocal lattice vector, and  $U_0$  is the mean displacement of the scattering nuclei. The first term in parenthesis represents the direct photoelectron current, the second term represents the indirect current arising from phonon-coupled transitions. The exponential can also be represented in terms of the Debye-Waller factor,  $W$ , given by (37) which is used to describe the temperature dependence of signal intensity as a function of temperature (38) [21].

$$e^{-\Delta k^2 U_0^2} = e^{-2W} \quad (37)$$

$$I = I_0 e^{-2W} \quad (38)$$

The mean displacement of the nuclei can be approximated by (39) which is identified by Hufner as the ‘Debye approximation’ in which  $M_A$  is the mass of the scattering center [11] [21]. This expression suggests that the mean displacement of the nuclei in the lattice should increase proportionately with temperature.

$$U_0 = \frac{3 \hbar^2}{M_A k_b \theta^2} T \quad (39)$$

Using a methodology presented by Hufner, substituting (39) into (36) yields (40).

$$I \propto |\sigma^2| \left( e^{-\Delta k^2 \left[ \frac{3 \hbar^2}{M_A k_b \theta^2} T \right]^2} \sum_{\mathbf{G}} \delta(\Delta \mathbf{k} - \mathbf{G}) + N \left( 1 - e^{-\Delta k^2 \left[ \frac{3 \hbar^2}{M_A k_b \theta^2} T \right]^2} \right) \right) \quad (40)$$

It is assumed that the final photon momentum approximates  $\Delta \mathbf{k}$  such that the magnitude of  $\Delta \mathbf{k}$  is described by (41).

$$\Delta k^2 = \sqrt{\frac{2mE}{\hbar^2}} \quad (41)$$

For a given spectral photoelectron feature, the intensity at an arbitrary temperature can be defined as a reference,  $I_{ref}$ . The intensity,  $I$ , at a different temperature can then be compared to  $I_{ref}$  using a ratio from (40) resulting in (42).

$$\frac{I}{I_{ref}} = \frac{e^{-\Delta k^2 \left[ \frac{3 \hbar^2}{M_A k_b \Theta^2} T \right]^2} \sum_{\mathbf{G}} \delta(\Delta \mathbf{k} - \mathbf{G}) + N \left( 1 - e^{-\Delta k^2 \left[ \frac{3 \hbar^2}{M_A k_b \Theta^2} T \right]^2} \right)}{e^{-\Delta k^2 \left[ \frac{3 \hbar^2}{M_A k_b \Theta^2} T_{ref} \right]^2} \sum_{\mathbf{G}} \delta(\Delta \mathbf{k} - \mathbf{G}) + N \left( 1 - e^{-\Delta k^2 \left[ \frac{3 \hbar^2}{M_A k_b \Theta^2} T_{ref} \right]^2} \right)} \quad (42)$$

The comparison of spectral intensities, changing only the single parameter of temperature, simplifies (42) to (43) which can be used to identify the Debye temperature from experimental data [11].

$$\ln \frac{I}{I_{ref}} = - \frac{3 \hbar^2 \sqrt{\frac{2mE}{\hbar^2}}}{M_A k_b \Theta^2} T + C \quad (43)$$

When plotted as the logarithm of the relative intensity vs. temperature, the slope contains  $\Theta$  which can be extracted by substitution of appropriate constants.

Another approach to identifying  $\Theta$  employs (38) and the definition of  $W$  for an isotropically vibrating system given by (44) [21].

$$2W = \frac{3T(\hbar \Delta k)^2}{M_A k_b \Theta^2} \quad (44)$$

This definition is consistent with (37) and (39) and simplifies the approach to (43) albeit neglecting the explicit discussion of the phonon-assisted photocurrent of (36).

Because XPS is a surface technique, the Debye temperature computed from XPS will be a surface Debye temperature. Previously stated, the Debye temperature corresponds to the energy at which the phonon modes are decoupled from the collective lattice vibrations. The Debye temperature may also be considered the temperature at

which all of the phonon modes are activated. A rigid surface will require more energy to reach this point than a less coherent surface. Therefore, a high Debye temperature equates to a stiffer surface which may reduce the diffusion of dopant materials and promote strain at non-homogenous boundaries. Once an electronic junction has been formed by dopant implantation during the construction of a device, diffusion of the dopant will reduce device efficiency. Conditions under which the Debye temperature decreases substantially are therefore operating limitations.

### 2.3.6 Auger Emission and the Auger Parameter

Auger electron emission complements photoemission and is modeled as a three-electron process. After the formation of a core-hole by photoemission,  $C1$ , the energy of the atom is reduced when an electron in a lower energy shell fills the hole, creating a second hole,  $C2$ . The energy difference between the two electron states may be emitted as a photon or by emission of an electron creating a third hole,  $C3$ . Electrons generated by this process are called Auger electrons. To first order, the kinetic energy of the Auger electron is the difference between the binding energies of the two core electron states reduced by the binding energy of the Auger electron. However, the creation of each core-hole may also be accompanied by atomic relaxation which reduces the energy carried by the emitted electron. This is summarized by (45) which is modified from [22].

$$KE_{Auger}(C1, C2, C3) = (BE_{C1} - BE_{C2}) - BE_{C3} - E_{Relaxation}(C1, C2) \quad (45)$$

Auger emissions are named using the spectroscopic notation described in 2.1. By way of example, the KLL Auger emission of atomic oxygen is graphically depicted by Figure 9.

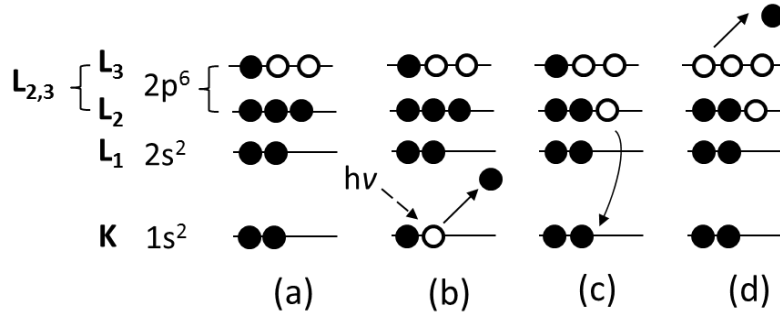


Figure 9. The generation of an Auger electron in atomic oxygen. An x-ray creates a core hole, C1, in the K shell shown in (b) of a ground-state atom depicted in (a). A second hole, C2, is created in an L shell, the electron filling C1 as shown in (c). The Auger emission creates the third hole, C3, shown in (d). The full nomenclature of this emission is O(KL<sub>2,3</sub>L<sub>2,3</sub>). The energy difference between L<sub>2</sub> and L<sub>3</sub> is small and thus the levels are essentially the same energy. All of the emissions involving the KLL levels are referred to collectively as the O(KLL). Figure after [9].

From the binding energies of the K (525 eV) and L<sub>2,3</sub> (7 eV) electrons, the estimated kinetic energy of the O(KL<sub>2,3</sub>L<sub>2,3</sub>) is 511 eV where the ‘O’ indicates oxygen [23]. Experimentally, this is observed around 507 eV and is strongly affected (several eVs) by the chemical environment of the atom [24].

Two uranium oxide Auger emissions of interest are the U(N<sub>6,7</sub>O<sub>4,5</sub>) and U(N<sub>6,7</sub>O<sub>4,5</sub>V). The N<sub>6,7</sub> indicates the 4f states with N<sub>7</sub> specifically identifying the 4f<sub>7/2</sub> electronic level. In both emission processes, the initial core-hole is of 4f nature. The O<sub>4,5</sub> is the 5d state while the valence band is indicated by ‘V’. In this research, these are referred to simply as the U NOO) and U NOV.

The Auger parameter,  $\alpha_{AP}$ , a relationship relating an Auger emission to an XPS core-level feature of the same element, may identify or differentiate between different chemical environments of the investigated atom by exploiting the differences in the Auger energies. Given by (46), the Auger parameter is defined as the difference in

kinetic energies of the Auger electron and the photoelectron emitted by creation of C1 [22].

$$\alpha_{AP} = KE_{Auger}(C1, C2, C3) - KE_{XPS}(C1) \quad (46)$$

The addition of the photon source excitation energy to the Auger parameter produces,  $\alpha'_{AP}$ , or modified Auger parameter which simplifies to (47) and uses the XPS binding energy in lieu of the kinetic energy. This form is universal in that it is independent of the photon source energy and spectrometer calibration [22].

$$\alpha'_{AP} = KE_{Auger}(C1, C2, C3) - BE_{XPS}(C1) \quad (47)$$

The modified Auger parameter is often simply referred to simply as the Auger parameter and all references will assume the modified version.

An advantage of the Auger parameter is the insensitivity to energy calibration. Measurements taken with different spectrometers may therefore be directly compared. In addition, the low kinetic energy of Auger electrons provides a more surface-sensitive measurement than traditional XPS. A U 4f<sub>7/2</sub> photoelectron generated from Al K $\alpha$  radiation is attenuated by approximately 20 Å of UO<sub>2</sub>. In contrast, the 286 eV U NOO Auger electron is attenuated in approximately 7 Å which is on the order of the unit cell dimension.

## 2.4 Schottky-Mott Theory

One of the requirements for a practical semiconductor device is the ability to operate in a circuit which infers the application of metal contacts. The simplest

semiconductor device is a rectifier made from a metal to semiconductor contact. The contact can be rectifying or non-rectifying (Ohmic or Schottky) [25]. The behavior of the resulting metal-semiconductor junction can be modeled with the energy band diagram of Figure 10 which depicts a metal and p-type semiconductor. The energy levels depicted are the vacuum level,  $E_{vac}$ , the conduction band edge,  $E_{cp}$ , the valence band edge,  $E_{vp}$ , the Fermi level,  $E_f$ , and the band gap,  $E_g$ . The energy bands of the isolated p-type semiconductor and the metal are placed together by any number of processes to create a junction which is shown in an idealized, abrupt transition region at the contact location though in reality such a junction would have a finite transition length. The bands of the semiconductor bend to align the Fermi levels of both materials which creates a barrier to charge carriers, which in this case are holes. The barrier height,  $\phi_{bp}$ , is a function of the metal's work function,  $\phi_m$ , and the electron affinity of the semiconductor,  $X_s$ . The Schottky-Mott equations describe this relationship which is often presented for an n-type semiconductor metal junction with a barrier height of  $\phi_{bn}$  given (48) [26].

$$q\phi_{bn} = q\phi_m - q\chi \quad (48)$$

$$q\phi_{bp} = E_g - (q\phi_m - q\chi) \quad (49)$$

The barrier of a p-type semiconductor metal junction is given by (49) and is related to (48) by (50) which prescribes that the magnitudes of the barrier heights  $\phi_{bn}$  and  $\phi_{bp}$  sum to the band gap.

$$q(\phi_{bn} + \phi_{bp}) = E_g \quad (50)$$

The junction forms a built-in voltage,  $V_{bi}$ , which is the difference in the work functions of the materials. The  $V_{bi}$  is not the same as  $\phi_b$ . The electronegativity of the semiconductor,  $X_s$ , is the energy difference between the conduction band and the vacuum level while the work function is the energy difference between the vacuum level and the Fermi level.

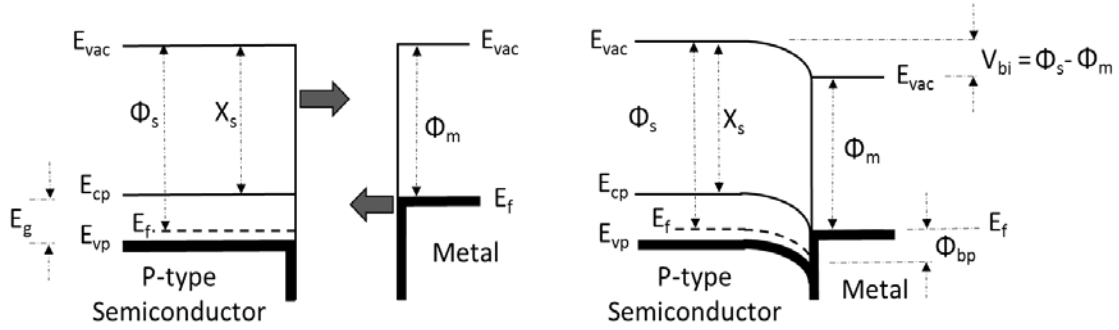


Figure 10. The energy band diagram of a p-type semiconductor and a metal depicted separately on the left and joined in a junction on the right. The Fermi-levels align and the energy levels bend correspondingly. The energy levels of the vacuum, conduction band, valence band, and Fermi are represented by  $E_{vac}$ ,  $E_{cp}$ ,  $E_{vp}$ , and  $E_f$ . The band gap is denoted as  $E_g$ . The work function of the semiconductor and the metal are depicted as  $\phi_s$  and  $\phi_m$ . The barrier height is  $\phi_{bp}$  as predicted by (49). The electronegativity of the semiconductor is  $X_s$ . Figure after [25].

A minimized barrier is achieved by choosing the metal work function with respect to the semi-conductor electron affinity such that (48) or (49) is minimized [26]. In some cases, metal induced gap states at the interface of the junction can provide allowed energies in the band gap that reduce the predicted barrier height [26].

## 2.5 Hydrothermal Crystal Growth

The hydrothermal growth technique employs an aqueous environment under high pressure and temperature conditions to dissolve and recrystallize a normally insoluble material. The conditions of pressure and temperature are often in the supercritical regime



for water though milder growth conditions may be described as hydrothermal by the crystal growth community. The critical point of water is 647 K (374 °C, 705 °F) and 218 atm (22.064 MPa, 3200 psia).

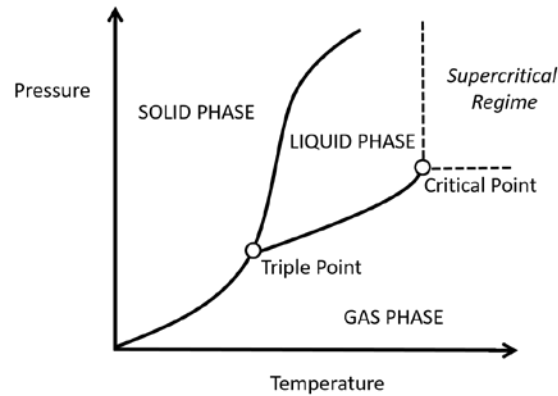


Figure 11. The critical point of water is 647 K (374 °C, 705 °F) and 218 atm (22.064 MPa, 3200 psia).

The term ‘hydrothermal’ describes the natural process of mineral formation under similar conditions of heat and pressure within the earth [27]. Crystals form a stable phase of the growth conditions and are highly ordered. The growth technique has been used to produce highly pure and dislocation free quartz since the 1940’s for radio and optical components and wrist-watch bezels [27].

A typical growth reaction makes use of the temperature-dependent solubility difference between a nutrient dissolution zone and a crystal growth zone. Geometrically, the regions are arranged vertically with the dissolution zone at the bottom of the reaction vessel so that gravity can hold un-dissolved solids in place. Figure 12 shows a Bridgeman autoclave around which is wrapped 4 heating bands to control the zone temperatures; two for the growth zone, and two for the dissolution zone. A pressure gauge and safety valve

sit atop the autoclave. A solubility additive known as a mineralizer can be added to the working fluid to enhance solubility of the growth nutrient. Although charged as a liquid, under growth conditions the aqueous fluid fills the entire reaction vessel. The temperature differential between the zones provides a turbulent, convective flow which brings dissolved nutrient to the colder growth zone where the nutrient may deposit either on a seed crystal (a transport growth reaction) or on the walls of the growth chamber (a spontaneous nucleation reaction). Seed crystals are supported by wires in order to maximize the surface area in contact with the solution. The reaction is typically housed in a sealed ampoule of a noble metal such as Ag to protect the autoclave from corrosive mineralizers. The flow rate and flow pattern can be altered by the use of baffles. In order to achieve the desired growth pressure, a specific charge volume is added to the sealed ampoule such that the operating temperature will provide the desired pressure (>3200 psia) without exceeding the limits of the equipment. A growth reaction is intended to operate under steady-state thermodynamic conditions. The initiation and shutdown of a reaction requires either a heating or cooling phase which can alter the composition of the seed crystal surface. Transient solubility conditions can dissolve the seed crystal on the approach to operating temperature, re-dissolve the growth product during cool-down, or preferentially deposit undesirable species on the seed crystal.

The high-pressure, high-temperature nature of the reaction within a sealed vessel makes it difficult to sample the growth solution and determine the intermediate species responsible for the crystal growth mechanism. The growth conditions are therefore determined experimentally. Although solubility data for milder conditions may inform the process, the solubility of the nutrient is determined experimentally.

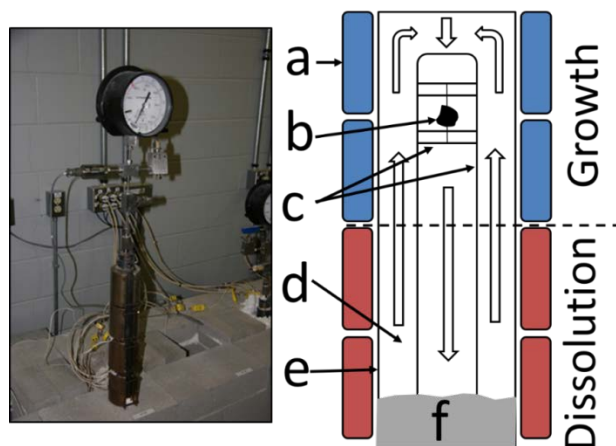


Figure 12. A Bridgeman autoclave on the left showing 4 heater bands and a pressure gauge. On the right is a drawing of the sealed metal ampoule (e) inside the autoclave within which sits a ladder made of wire (c) supporting a seed crystal (b) which is surrounded by a mineralizer solution (d). The nutrient, or feedstock (f) sits at the bottom of the dissolution zone which is kept hotter than the growth zone. The difference in the zone temperatures determines the differential solubility (the growth rate). A convective flow pattern is established which transports dissolved nutrient into the growth zone.

Solubility data is deduced from the mass lost to dissolution of a crystal under the reaction conditions of interest. Because the pressure and temperature conditions are rather extreme, a solubility experiment requires the crystal produced in a growth reaction. Thus, efficient growth reactions are informed by solubility data; solubility data is determined by dissolving the growth product. When a crystal is dissolved into an aqueous solution, the change in crystal mass,  $\Delta m_{crystal}$ , relative to the mass of the liquid phase,  $m_{liquid\ phase}$ , yields the mass percentage transferred to the liquid phase.

$$Mass\ \% = \frac{\Delta m_{crystal}}{(\Delta m_{crystal} + m_{liquid\ phase})} \quad (51)$$

Such data was determined in earlier research for  $ThO_2$  under conditions producing strong crystal phases, a portion of which is displayed in Figure 13.

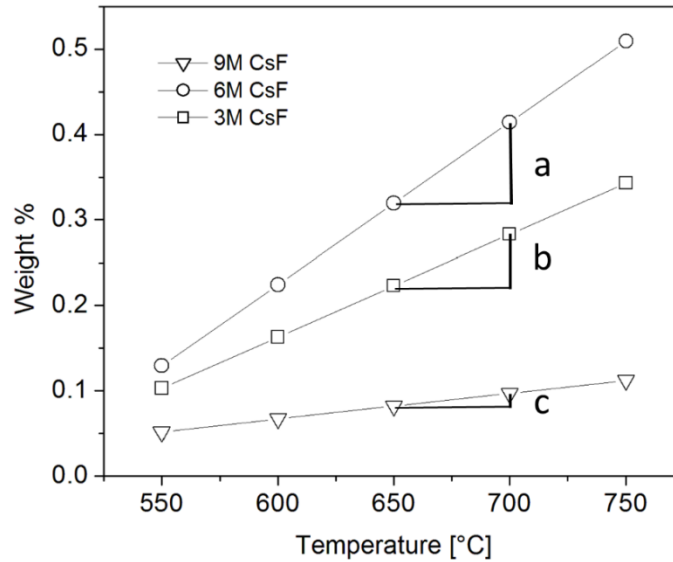


Figure 13. The solubility of  $\text{ThO}_2$  in an aqueous CsF mineralizer solution at 25k psia adapted from [28]. The solubility difference as a function of CsF concentration for the same  $50^\circ$  temperature gradient is depicted by a, b, and c. Solubility (i.e. growth rate) is controlled by both the mineralizer concentration and temperature gradient. The same growth rate may be achieved anywhere along a linear solubility line for a given temperature gradient. However, crystal composition may differ based on the competing solubility of impurity species.

The solubility data was determined using different concentrations of CsF mineralizer solution at 25 kpsia. Solubility is enhanced by formation of fluoride metal ion complexes and therefore shows a dependence on mineralizer concentration. The temperature gradient between the dissolution and crystallization zones can be maintained along the nearly linear solubility lines with the same growth rate. The growth rate, driven by the solubility difference as expressed in weight percent on the vertical axis, improves with either increased mineralizer concentration or larger temperature gradient. The growth temperatures, for the same gradient, can be altered to operate in a region which minimizes crystal impurities.

## 2.6 Stoichiometry and Oxygen Defects

Uranium dioxide has the fluorite crystal structure pictured in Figure 14 which can be described as a face centered cubic (FCC) lattice of uranium atoms enclosing a simple cubic lattice of oxygen atoms. The conventional unit cell therefore contains the stoichiometric O/U ratio of 2.

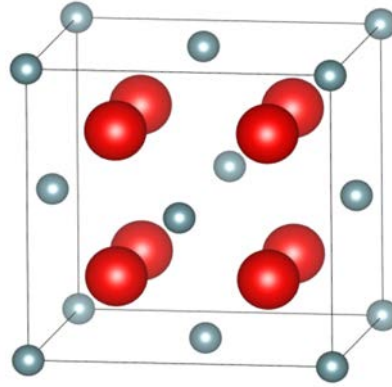
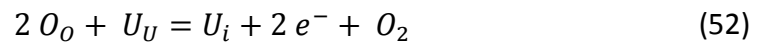


Figure 14. The fluorite structure of the  $\text{UO}_2$  conventional unit cell. The smaller uranium atoms (blue) are located in the FCC position surrounding the larger oxygen atoms (red) of a simple cubic. Image produced using [29].

The fluorite structure is maintained between  $\text{UO}_2$  and  $\text{UO}_{2.25}$  as a result of the open structure which permits O atoms to be incorporated in interstitial spaces. Oxygen defects influence the structure and electronic properties of  $\text{UO}_2$ .

The theory of oxygen pressure on the defect formation in  $\text{UO}_2$  is developed by [30] and a summarized adaptation is presented here. The formation of an interstitial uranium defect,  $U_i$ , and an oxygen vacancy,  $V_O$ , from occupied lattice positions  $U_U$  and  $O_O$ , can be expressed by (52) and (53) [30].



$$O_o = V_o + 2 e^- + \frac{1}{2} O_2 \quad (53)$$

The rate expressions, substituting  $n = [e^-]$  and  $[O_2] = p(O_2)$ , are described by (54) and (55) [30].

$$K_{U_i}[O_o]^2[U_U] = [U_i]n^2 p(O_2) \cong K_{U_i} \quad (54)$$

$$K_{V_o}[O_o] = [V_o]n^2 p(O_2)^{1/2} \cong K_{V_o} \quad (55)$$

For the limiting condition that  $[U_i] \gg [V_o]$  and substitution of  $n = 2[U_i]$ , the expression for the  $U_i$  concentration is developed by (68) and expressed as (69) [30].

$$4[U_i]^3 p(O_2) = K_{U_i} \quad (56)$$

$$[U_i] = \left( \frac{K_{U_i}}{4} \right)^{\frac{1}{3}} p(O_2)^{-\frac{1}{3}} \quad (57)$$

The expression for  $[V_o]$  is given by (58) which is developed by substitution of  $n = 2[U_i]$  and (57) into (55).

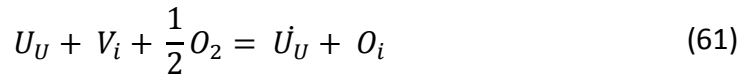
$$[V_o] = \frac{K_{V_o} p(O_2)^{\frac{1}{6}}}{(2K_{U_i})^{\frac{2}{3}}} \quad (58)$$

For the limiting condition that  $[U_i] \gg [V_o]$  and corresponding substitution of  $n = 2[U_o]$ , the defect concentrations are given by (71) and (72) [30]. If one considers this limiting condition most appropriate, the reduction of oxygen vacancies accompanies an increase of the oxygen pressure.

$$[V_O] = \left( \frac{K_{U_i}}{4} \right)^{\frac{1}{3}} p(O_2)^{-\frac{1}{6}} \quad (59)$$

$$[U_i] = \frac{K_{U_i} p(O_2)^{-\frac{2}{3}}}{(2 K_{V_O})^{\frac{2}{3}}} \quad (60)$$

Hypostoichiometric  $UO_2$  can be described by Frenkel defect formation in which an oxygen atom occupies an interstitial site within the unit cell. The requirement of charge compensation necessitates that the U(IV) atoms in the vicinity of the interstitial anion become U(V) [30]. The formation of the interstitial oxygen defect,  $O_i$ , is described by (61) in which  $U_U$  remains the uranium atom in a normally occupied lattice position,  $V_i$  is the unoccupied interstitial vacancy, and  $U_U'$  is the oxidized uranium atom resulting from charge neutrality. The concentration of the interstitial oxygen can be expressed by (62). Considering that the unit cell stoichiometry changed from  $UO_2$  to  $UO_3$  or  $UO_{2+x}$  where  $x = 1$ . Substitution of  $x = [O_i]$  into (62) indicates that  $x$  is proportional to the square-root of the oxygen pressure shown in (63).



$$[O_i] = \frac{K_{O_i} [U_U] [V_i] p(O_2)^{\frac{1}{2}}}{[U_U']} \quad (62)$$

$$x \propto p(O_2)^{\frac{1}{2}} \quad (63)$$

The mechanism of uranium oxidation, however, is more complicated than the simple addition of an interstitial oxygen to the fluorite cell. Recent research has shown that the inclusion of oxygen into a  $UO_2$  lattice through a (111) surface occurs in an ordered and

periodic way which differs from classical diffusion [31]. High temperature measurements between 600 and 1000 °C relating the equilibrium oxygen pressure to oxide stoichiometry show a more complex relationship than that described by (63) [30].



### **III. Crystal Growth and Characterization**

#### **3.1 Growth and Analysis of UO<sub>2</sub> Crystals**

The refinement of the growth process is both iterative and empirical; each growth reaction building upon the results of the previous reaction to produce a higher-quality crystal. The name of each crystal sample uses an alphanumeric scheme which describes the origin and chronological reaction serial of the form; 'AAA-B-##C'. The first string, 'AAA', is the feedstock description. The second, 'B', is either 'T' for transport or 'SN' for spontaneous nucleation. The last string, '##C', is an index number identifying the reaction number and a letter which is used to distinguish between individual crystals recovered from the same reaction. For example, UO<sub>2</sub>-T-19a represents the first of multiple crystals from reaction number 19 produced under transport growth conditions from a UO<sub>2</sub> feedstock. For simplification, the sample may be abbreviated 'T19a'.

##### **3.1.1 Phase Study**

In the case of UO<sub>2</sub> for which hydrothermal growth is novel, a series of experimental crystal growth reactions were used to determine appropriate growth conditions for crystal production. Varying only the mineralizer type and concentration, a total of 30, 7-day spontaneous nucleation growth reactions were conducted at 25 kpsia with dissolution and growth zone temperatures of 650 and 600 °C. The resulting crystalline products, or crystal phases, were analyzed. Desirable growth conditions produce UO<sub>2</sub> crystals without competing uranium or mineralizer consuming phases. The phase study strongly identified CsF as the mineralizer of choice.

## 3.2 X-ray Diffraction Analysis

### 3.2.1 Single-Crystal XRD

A fragment of the UO<sub>2</sub>-SN-89b sample was analyzed by single-crystal XRD using a Rigaku XtaLAB Mini single-crystal x-ray diffractometer. The unit cell was resolved to 3 orthogonal and identical lattice parameters of length  $5.4703 \pm 0.0006$  Å consistent with the fluorite structure. The lattice parameter of UO<sub>2.000 ± 0.001</sub> was measured by [32] to be  $5.47127 \pm 0.00008$  Å at 20 °C. The addition of oxygen beyond O/U = 2 contracts the lattice to 5.445 Å at UO<sub>2.25</sub>, the point at which the UO<sub>2+x</sub> phase is lost [33]. Interpolation between these two values provides a sample stoichiometry of UO<sub>2.003</sub>. This measurement is conservative in that the measured sample had both a high surface to volume ratio and was exposed to ambient oxygen pressure for several days prior to the measurement.

### 3.2.2 Rocking Curve Measurement

The single-crystal nature of the samples was confirmed with a rocking curve (or omega scan) measurement using a PANalytical Empyrean x-ray diffractometer. The 2 $\theta$  absolute scan, Figure 15, showed a single family of Bragg peaks in the diffraction pattern indicating that the specimen was a single crystal.

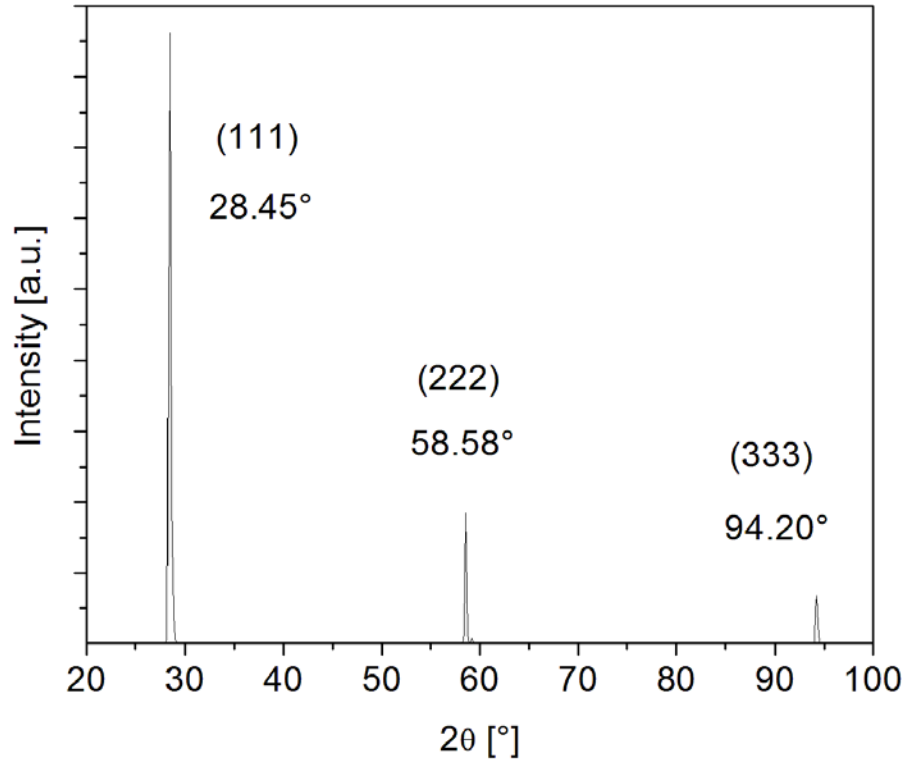


Figure 15. The single-crystal XRD absolute scan of the  $\text{UO}_2$  crystal. The single family of Bragg peaks indicates a single-crystal sample.

A subsequent omega scan ( $1\theta$ ), centered on the angle of the (111)  $2\theta$  peak, was collected at  $0.01^\circ$  increments between  $13.5962^\circ$  and  $15.5862^\circ$ . The full-width at half-maximum (FWHM) was determined by a Gaussian fit to be  $0.4566 \pm 0.0007^\circ$ . The small angle indicates that the crystal is well-ordered and reflects the variation in the mean distance between the (111) planes of the single crystal.

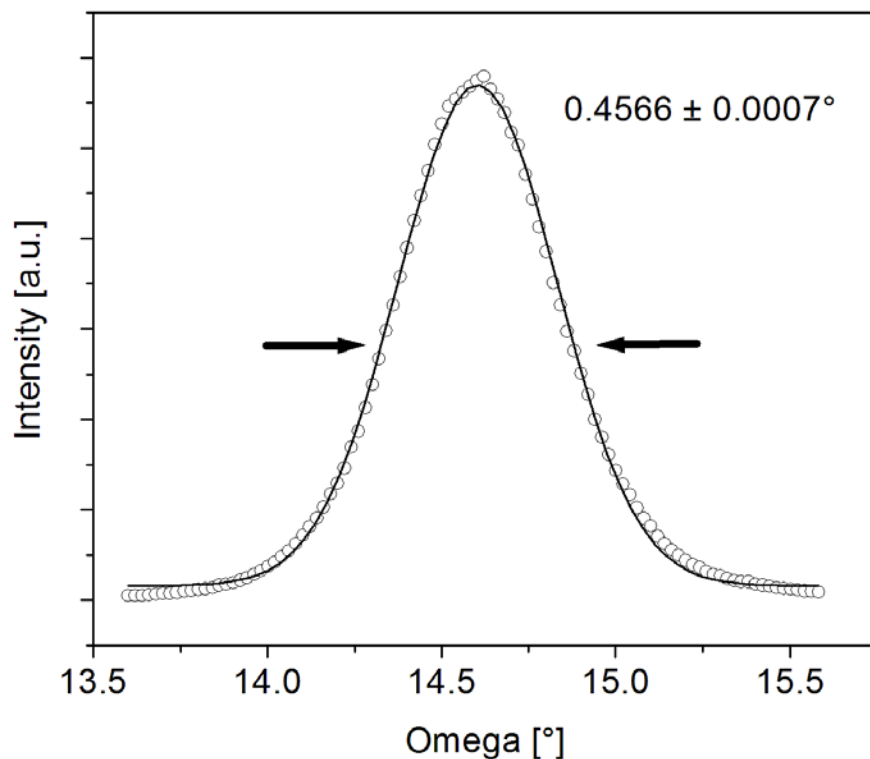


Figure 16. The rocking curve of the UO<sub>2</sub>-T-29b (111) sample about the Bragg angle of the single peak. The FWHM of  $0.4566 \pm 0.0007^\circ$  was determined by a Gaussian fitting.

The primary results of the XRD measurement is confirmation of the orientation and single-crystal nature of the sample. However, the centroid angle of the rocking curve,  $14.6^\circ$ , indicates a lattice parameter of  $5.43 \text{ \AA}$  indicating that the measured crystal was oxidized from several days of exposure to atmospheric oxygen pressure prior to measurement.

### 3.3 PES Analysis

#### 3.3.1 XPS Confirmation of Stoichiometry

XPS spectra of the core and valence levels of UO<sub>2</sub>-T-18a showed excellent agreement with UO<sub>2</sub>. The most intense core level photopeaks belong to U4f which show shake-up satellite features about 7 eV from each peak. Figure 17 shows the fitting of the U4f region with binding energies summarized in Table 3. For comparison, the spectral summary of high-resolution XPS measured by [34], in good agreement with other high-resolution measurements, of UO<sub>x</sub> surfaces is presented [35].

Table 3. The XPS spectral summary of UO<sub>2</sub>-T-18a and comparative spectra from high-resolution XPS on UO<sub>x</sub> [34]. The measured values for T18a are  $\pm 0.03$  eV. The absence of comparative data indicates the feature either cannot be resolved, ‘- -’, or does not exist, ‘n/a’.

	UO <sub>2</sub> -T-18a		UO <sub>2.00</sub>		UO <sub>2.22</sub>		UO <sub>1.71</sub>	
	B.E. [eV]	FWHM [eV]	B.E. [eV]	FWHM [eV]	B.E. [eV]	FWHM [eV]	B.E. [eV]	FWHM [eV]
U4f <sub>7/2</sub>	380.24	1.76	380.00	2.00	379.20	2.60	380.60	2.40
U4f <sub>7/2</sub> Satt.	387.15	3.49	386.90	--	386.00	n/a	n/a	n/a
U4f <sub>5/2</sub>	391.09	1.79	390.70	2.10	390.10	2.70	391.50	2.40
U4f <sub>5/2</sub> Satt.	398.07	4.05	397.70	--	396.70	n/a	398.30	n/a
U5f	1.43	1.67	1.40	2.4	0.90	2.4	2.70	2.8
O1s	530.50	2.07	530.50	1.80	529.40	1.70	531.40	1.60

The T18a sample shows excellent agreement with the valence and oxygen binding energies of a stoichiometric sample. The U4f<sub>7/2</sub> peak agrees with an O/U = 2.00 but the satellite spacing suggests that the sample is slightly hypostoichiometric.

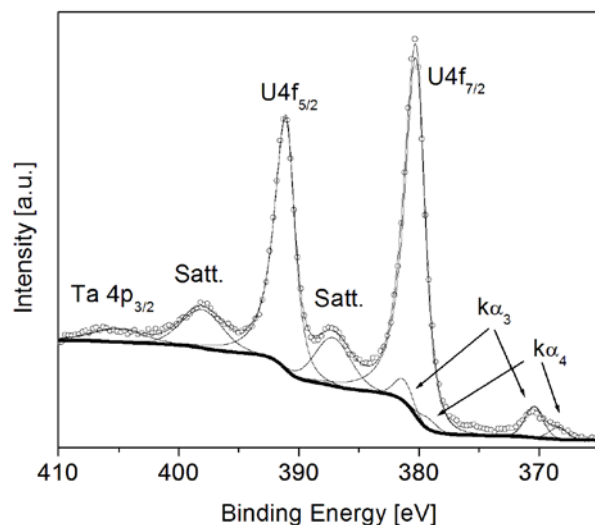


Figure 17. The U4f spectrum of UO<sub>2</sub>-T-18a. The Al  $K\alpha_{3,4}$  ghost peaks were fitted to remove the effects of the nonmonochromated x-ray source.

The measurement was preceded by argon sputtering which is known to leave the surface in such a state. However, the measurement took several hours and surface reconstruction is expected under vacuum conditions. The U5f, a high kinetic energy emission, originates from deeper within the lattice and may not reflect the surface hypostoichiometry.

Defining the valence band maximum to be one standard deviation below the U5f peak, the T18a sample has a valence band maximum 0.72 eV below the Fermi level. It is estimated that intrinsic UO<sub>2</sub> has a 2 eV band gap suggesting the sample must be p-type. However, the high-resolution data measured by [34] for UO<sub>2.00</sub> produces an even stronger indication of p-type with a band edge of 0.38 eV below the Fermi level. If, however, the valence band edge is  $0.4\sigma$  below the U5f peak, the T18a sample edge falls 1.15 eV below the Fermi level and the high resolution data aligns at 1 eV, or one-half the band gap.

Although this does not have a solid statistical basis, it does explain the hypostoichiometry observed in the T18a sample and suggests the material is slightly n-type.

### **3.3.2 Auger Parameter Analysis**

The NOV:U4f Auger parameter, insensitive to charging effects or calibration error, indicates the T18a sample is  $\text{UO}_2$  or perhaps even  $\text{UO}_{2-x}$ . The Auger parameter of T18a was measured to be 660.7 eV which is above the value of 660.0 eV measured for  $\text{UO}_2$  [36]. For comparison, the values for U,  $\text{UO}_3$ ,  $\text{U}_3\text{O}_8$ , and  $\text{U}_4\text{O}_9$  are 658 eV, 659.2 eV, 659.6 eV, and 659.8 eV respectively [36]. There are no known published values for hypostoichiometric  $\text{UO}_{2-x}$  NOV:U4f Auger parameter.

The NOO:U4f Auger parameter was also measured on the UO2-T-29b sample with similar results: 564.6 eV which is above the value of 564.3 eV measured for  $\text{UO}_2$  [36]. For a similar comparison, the values for U,  $\text{UO}_3$ ,  $\text{U}_3\text{O}_8$ , and  $\text{U}_4\text{O}_9$  are 564.0 eV, 564.2 eV, 564.0 eV, and 563.9 eV respectively [36]. There are no known published values for the hypostoichiometric  $\text{UO}_{2-x}$  NOO:U4f Auger parameter either.

## IV. Electronic Characterization of the Crystal Surface

### 4.1 Surface & Subsurface Stoichiometry

The stoichiometry of the samples was investigated using depth-resolved XPS. A binding energy shift of the U4f core level would indicate a change in the chemical environment of the U atoms. As the angle of the sample relative to the electron analyzer is altered from normal, the surface is preferentially measured. If the surface was hyperstoichiometric, the binding energies of the core levels would shift by as much as 1.5 eV higher as outlined in Table 4. It should be noted, however, that a measured peak can be influenced by a contribution from multiple oxidation states [35] [34].

Table 4. The binding energies of the U4f peaks as a function of oxidation state.

UO <sub>x</sub>		U4f <sub>7/2</sub> BE [eV]	U4f <sub>5/2</sub> BE [eV]
UO <sub>2</sub>	UO <sub>2</sub>	380	390.9
UO <sub>2.25</sub>	U <sub>4</sub> O <sub>9</sub>	380.5	391.4
UO <sub>2.5</sub>	U <sub>2</sub> O <sub>5</sub>	380.7	391.6
UO <sub>2.7</sub>	U <sub>3</sub> O <sub>8</sub>	381	391.7
UO <sub>3</sub>	UO <sub>3</sub>	381.5	392.2

Three UO<sub>2</sub> samples were investigated by depth-resolved XPS, UO2-T-18A, and UO2-T-29a&b. The T18a sample had a spheroid geometry while the T29 samples were planar. The information limit of the sub-surface is approximately 50 Å. The results indicated that the crystal surface may oxidize under ambient conditions and stable under vacuum.



#### 4.1.1 Depth Resolved Chemical Shift (Surface to Core Level Shift)

The UO<sub>2</sub>-T-18A sample was mounted, sputtered, and aligned in the XPS system with the sample surface normal to the electron analyzer. The angle was varied from 0° to 59° in 5° increments. At angles steeper than 59°, the XPS signal was no longer resolved. A binding energy shift of approximately 1 eV was observed as shown in Figure 18. Signal diminution was also observed at higher angles. However, the spherical nature of the sample is not conducive to this measurement technique. The sputtering process does not prepare the surface under the crystal equator, a region that increasingly provides signal as the angle is increased. The binding energy shift can be attributed to the oxidized and un-sputtered crystal surface which was exposed for many days to atmospheric oxygen before measurement. Therefore, the sputtered surface is indicative of O/U = 2 indicating that the crystal bulk is nearly stoichiometric UO<sub>2</sub>. The unprepared surface indicates that higher oxides form on a bulk UO<sub>2</sub> crystal under atmospheric conditions.

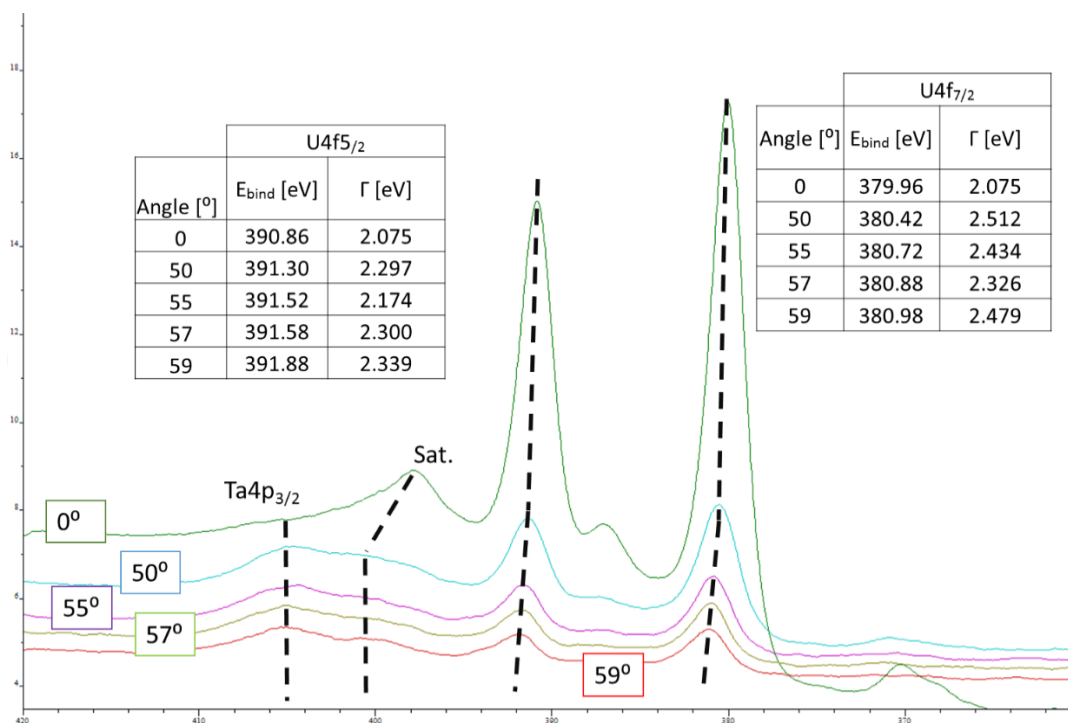


Figure 18. The depth-resolved XPS measurements of the U4f region from normal (0°) to 59°. The binding energy shift of the 4f core levels indicates an increase in the oxidation state of U. The inefficiently sputtered hemisphere of the round sample was responsible for the increasing contribution of higher uranium oxides to the peak at steep angles and subsequent large binding energy shift.

The experiment was repeated for both the T29a (100) and T29b (111) samples which had planar geometry and measured 9×12 mm. They completely filled the spectrometer field of view and were uniformly sputtered. The most surface sensitive angles were measured 6 days after the experiment was initiated providing the maximum time for surface reconstruction following surface preparation. Both samples exhibited a minor binding energy shift, on the order of +0.15 V, between the 0° and ~90° measurements. The results are summarized in Figure 19 and Figure 20. The normal angle measurements were repeated at the conclusion of the experiment and were essentially unchanged. The repeated T29a (100) measurement remained the same while the T29b

(111) measurements was shifted by -0.06 eV. Near 90°, the sample edge contributes to the signal which is observed by a drop in binding energy.

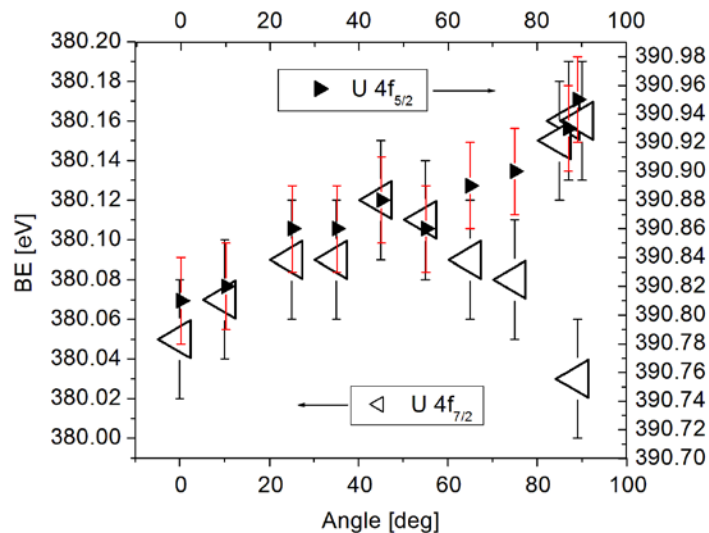


Figure 19. Depth resolved XPS on the UO<sub>2</sub>-T-29a (100) sample. The binding energy shift from minimum to maximum value is 0.11 eV for the 4f<sub>7/2</sub> and 0.14 eV for 4f<sub>5/2</sub>.

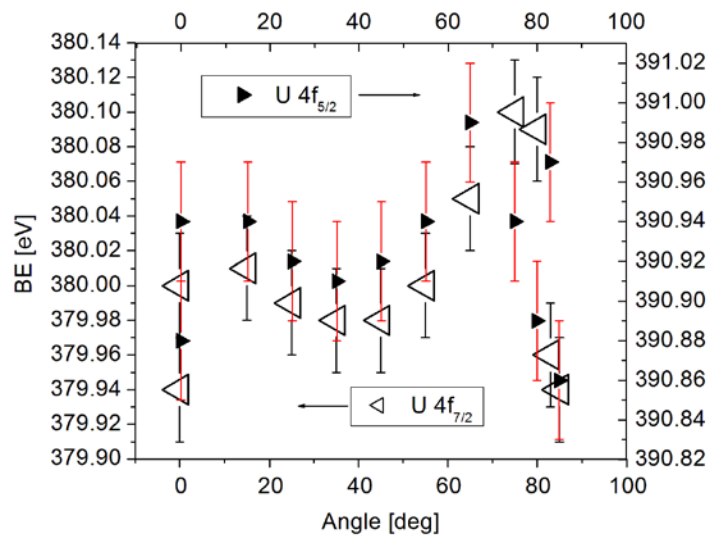


Figure 20. Depth resolved XPS on the UO<sub>2</sub>-T-29b (111) sample. The binding energy shift from minimum to maximum value is 0.16 eV for the 4f<sub>7/2</sub> and 0.13 eV for 4f<sub>5/2</sub>. The 0° measurement was repeated at the end of the experiment and showed a shift to lower energy by 0.06 eV.

A small shift in the binding energy between the surface and subsurface is consistent with the increased contribution from higher oxidation states near the surface. The small magnitude of the shift suggests that the stoichiometry is similar. This is corroborated by similar but high-resolution depth-resolved measurements made at 70 °C by [35] on a polycrystalline  $\text{UO}_2$  sample which showed differing surface to sub-surface U  $4f_{7/2}$  contributions from  $\text{UO}_2$ ,  $\text{U}_3\text{O}_8$ , and  $\text{UO}_3$ . The sub-surface composition, in terms of  $\text{UO}_2$  /  $\text{U}_3\text{O}_8$  /  $\text{UO}_3$ , was reported as 32.6 % / 40.6 % / 21.1 % which changed at the surface to 29.5 % / 43.5 % / 25 %. Although the centroid energies of the two measured  $4f_{7/2}$  peaks were not reported, the decrease in contribution from  $\text{UO}_2$  and the increase from  $\text{UO}_3$  are consistent with the measured  $4f_{7/2}$  peak energy shift.

#### **4.1.2 Depth Resolved Auger**

The Auger parameters  $\text{NOV:U}4f_{7/2}$  and  $\text{NOO:U}4f_{7/2}$  were also measured as a function of the sample angle with respect to the analyzer. This measurement is more surface sensitive than the XPS depth-resolved U4f measurement alone because the kinetic energies of the Auger electrons are about a factor of five lower. Both measured parameters presented a shift toward higher oxidation states as the surface was preferentially sampled. Literature values for the Auger parameters of  $\text{UO}_x$  provide a guide to the trend but the sensitivity of the measurement causes imprecise absolute agreement. Figure 21 and Figure 22 summarize the angle-dependent measurements.

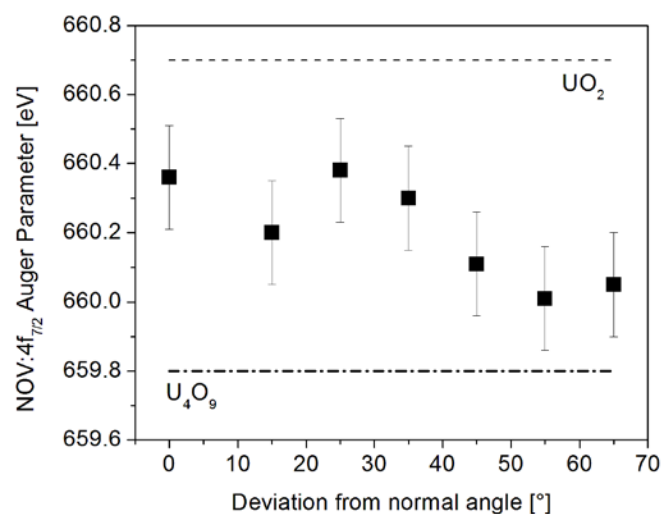


Figure 21. The angle-dependent U NOV:4f<sub>7/2</sub> Auger Parameter shown with an uncertainty of  $\pm 0.15$  eV. The dashed line, the parameter for UO<sub>2</sub>, and the dotted dashed line, the value for U<sub>4</sub>O<sub>9</sub>, as measured by [36], are depicted as reference points. The surface of the crystal displayed a trend toward hyperstoichiometry.

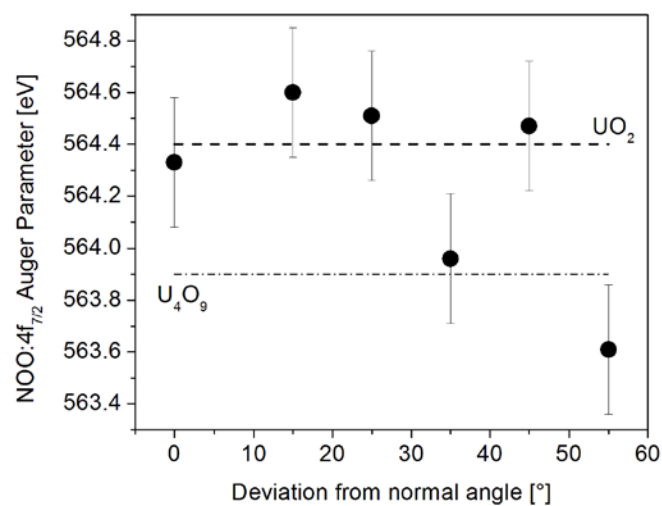


Figure 22. The angle-dependent U NOO:4f<sub>7/2</sub> Auger Parameter shown with an uncertainty of  $\pm 0.25$  eV. The dashed line, the parameter for UO<sub>2</sub>, and the dotted dashed line, the value for U<sub>4</sub>O<sub>9</sub>, as measured by [36], are depicted as reference points. The surface of the crystal displayed hyperstoichiometry.

The U NOO:4f parameter has a larger uncertainty based on the diminished signal to noise ratio of the NOO feature. Both measurements support a slight increase in the oxidation state of U at the surface and further indicate that the depth of the hyperstoichiometric region is probably less than 20 Å.

## **4.2 Effective Surface Debye Temperature Measurement**

The effective surface Debye temperature was measured by temperature-dependent XPS using the sample UO<sub>2</sub>-T-18a. This sample was very solid, the product of a slow growth, and stable under all temperatures considered in this research.

### **4.2.1 Debye Experiment**

The crystal was mounted to a tantalum plate with a k-type thermocouple for temperature monitoring, placed under high vacuum ( $10^{-9}$  Torr), and sputtered (Specs IQE 12/38 ion source, 99.999% Ar) with 1 kV Ar<sup>+</sup> ions at a nominal beam current of 40 µA to remove adventitious contaminants. Two in vacuo annealing conditions were studied post-sputter; a low-temperature anneal at 298 K for 12 hours and a high-temperature anneal at 623 K for 12 hours. X-ray photoemission spectroscopy (XPS) confirmed the clean sample surface subsequent to sputtering when the C1s peak intensity dropped below 3% of the U4f<sub>7/2</sub> photopeak intensity.

The XPS system was allowed to reach steady-state operating conditions over the course of 24 hours prior to measurement which used Mg k-alpha radiation (1253.6 eV), an energy step-size of 100 meV, and a pass energy of 100 eV with the analyzer

positioned normal to the sample surface. At 303 K, this provided over  $1.2 \times 10^6$  counts under the  $U4f_{7/2}$  photopeak after subtraction of a Shirley background. A total of 5 separate XPS spectra were measured at each of 14 different temperatures spanning the range of 303-573 K for each sample preparation from which the mean intensity was used for computation.

XPS spectra of the  $U4f$ ,  $U4d$ ,  $U5f$ , and the  $O1s$  regions were measured for the 298 K annealed surface to verify the phase change followed by measurement of the 623 K annealed surface  $U4f$  region to observe the annealing effect on the effective Debye temperature. The  $U4f_{7/2}$  photopeak is appropriate for the computation of the XPS derived  $\Theta_{DE}$  since it is the most intense core level feature of the  $UO_2$  spectrum and is highly localized.

An example deconvolution of the  $U4f$  spectrum, shown as Figure 23, was constructed into the principle component peaks shown in Table 5 using a Shirley background and Voigt profile line shapes (Gaussian/Lorentzian = 80%).

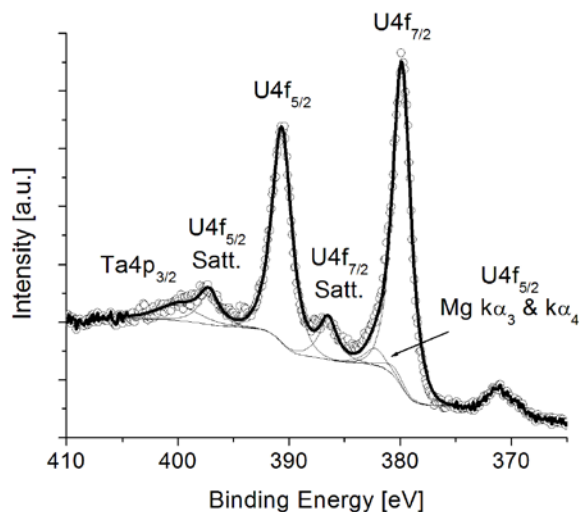


Figure 23. The deconvolved XPS spectrum of the U4f region. The raw XPS data is shown as open circles. The background and peak line shapes are shown as thin lines with the resulting envelope shown as a heavy line.

The Mg  $k\alpha$  excitation source is comprised of an unresolved doublet,  $k\alpha_{1,2}$ , with a centroid energy of 1253.6 eV. The Mg  $k\alpha_3$  and  $k\alpha_4$  lines contribute ‘ghost peaks’ displaced by - 8.4 eV and -10.1 eV with respective intensities of 0.08 and 0.041 of the  $k\alpha_{1,2}$  feature [37]. This phenomenon is primarily of concern for high-intensity peaks and is responsible for the high-BE shoulder of the  $U4f_{7/2}$  peak asymmetries which could be interpreted as a uranium oxidation state  $> 4+$  without careful fitting. The  $U4f_{7/2}$  ghost peaks are also visible at  $\approx 371$  eV. The sample mount contributes the  $Ta4p_{3/2}$  photopeak at 400 eV. The satellite features (‘shake-up’ peaks) located  $\approx 7$  eV higher than the main peaks are a distinct feature of  $UO_2$  and indicate alternate final electronic states of U [34] [38] [39]. Other regions were analyzed in a similar fashion.



Table 5. A nominal deconvolution of the U4f XPS spectral region at 303 K. The values shown are from a single measurement. Major peaks were well-supported by an integrated intensity in excess of a million counts.

Photopeak	Binding Energy [eV]	FWHM [eV]	Intensity [counts]
U4f <sub>7/2</sub>	380.05	1.905	1251735
U4f <sub>5/2</sub>	390.88	2.110	938801
U4f <sub>5/2</sub> Mg k $\alpha$ 3	382.48	2.110	75104
U4f <sub>5/2</sub> Mg k $\alpha$ 4	380.78	2.110	38491
U4f <sub>7/2</sub> Satellite	386.71	1.905	174816
U4f <sub>5/2</sub> Satellite	397.43	2.110	143665
Ta4p <sub>3/2</sub>	400.22	4.428	142638

#### 4.2.2 Debye Analysis

After sputtering and annealing the sample as previously described, the natural logarithm of photopeak intensity as a function of absolute temperature was plotted to determine the Debye-Waller factor. The plots are shown in Figure 24 for each U peak. The data shows two distinct regions of linearity for the core uranium lines; 300-450 K and 470-600 K. The intersection of the linear fit lines marks the threshold temperature at which the crystal surface undergoes a phase change which is between 476 K and 486 based on the U4f<sub>7/2</sub> peak. The slope of the fitting line above and below the threshold temperature equates to a transition from a high  $\Theta_{DE}$  to a low  $\Theta_{DE}$  suggesting that the (UO<sub>2+x</sub> + U<sub>4</sub>O<sub>9-y</sub>) phase presents a stiffer surface than the (UO<sub>2+x</sub>) phase. The computation of  $\Theta_{DE}$  from (44) is summarized in Table 6 and Table 7 using a scattering

center mass of 238 a.m.u. for depleted uranium. The uncertainty in the effective Debye temperature was computed from a 95% confidence interval about the fitted slope.

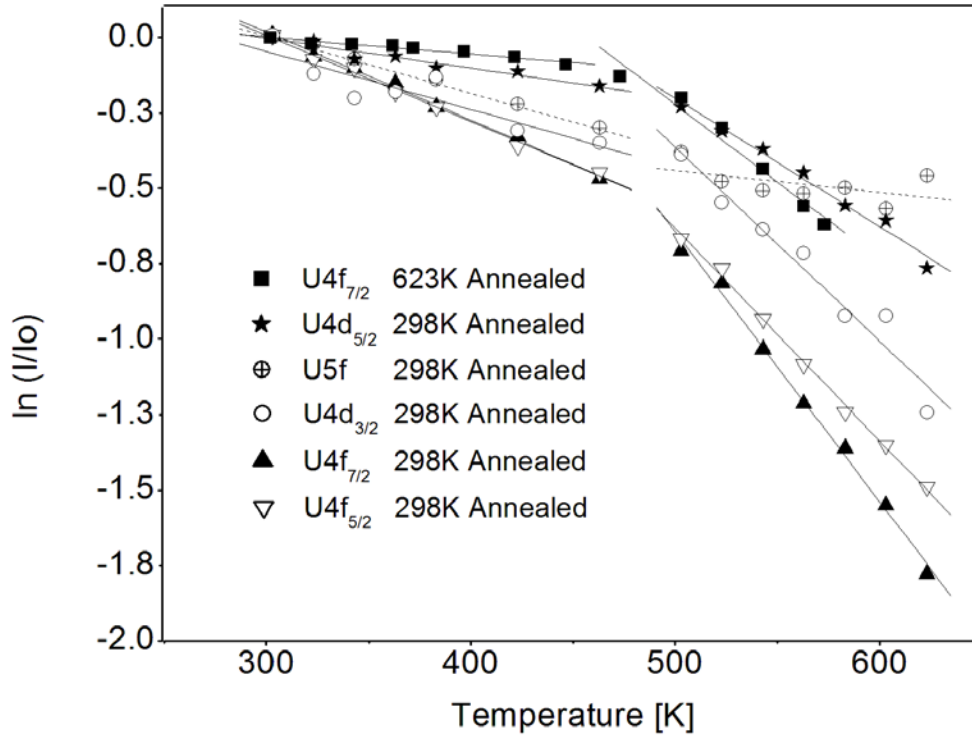


Figure 24. The natural logarithmic ratio of intensities for the uranium peaks as a function of temperature. The reference intensity was the intensity measured at 303 K for both surface annealing conditions. The 623 K annealed surface exhibits the shallowest slope indicating a high effective Debye temperature ( $500 \pm 59$  K) post-transition corresponding to the ( $\text{UO}_{2+x} + \text{U}_4\text{O}_{9-y}$ ) phase. The transition of the crystal surface to the ( $\text{UO}_{2+x}$ ) phase is marked by a sharp change in the intensity ratio point near 475 K. The slope post-transition indicates a lower effective Debye temperature ( $165 \pm 21$  K) for ( $\text{UO}_{2+x}$ ).

Table 6. Summary of the effective Debye temperature computation from the temperature-dependent, photoelectric intensity derived Debye-Waller factor of the sample annealed at 298 K for 12 hours. The U5f valence state does not follow the Debye-Waller relationship and is presented for comparison.

Peak	Temperature Range [K]	2W	Fit R <sup>2</sup>	$\Delta k$ [1/Å]	$\Theta_{DE}$ [K]
U4f <sub>7/2</sub>	300-470	0.00293 ± 0.000103	0.996	15.1	219 ± 4
	500-620	0.00898 ± 0.000357	0.904		125 ± 1
U4f <sub>5/2</sub>	300-460	0.00290 ± 0.000124	0.994	15.0	219 ± 5
	500-620	0.00101 ± 0.000246	0.980		139 ± 1
U4d <sub>5/2</sub>	300-460	0.00101 ± 0.000135	0.946	11.6	285 ± 19
	500-620	0.00430 ± 0.000338	0.980		138 ± 6
U4d <sub>3/2</sub>	300-460	0.00197 ± 0.000522	0.814	11.1	197 ± 27
	500-620	0.00648 ± 0.000790	0.954		108 ± 7
U5f	300-460	0.00193 ± 0.000269	0.940	18.1	323 ± 23
	500-620	0.00197 ± 0.000649	0.310		523 ± 33

Table 7. Summary of the effective Debye temperature computation from the temperature-dependent, photoelectric intensity derived Debye-Waller factor of the sample annealed at 623 K for 12 hours.

Peak	Temperature Range	2W	Fit R <sup>2</sup>	$\Delta k$ [1/Å]	$\Theta_{DE}$ [K]
U4f <sub>7/2</sub>	300-450K	0.000687 ± 0.000064	0.951	15.1	500 ± 59
	470-570K	0.00642 ± 0.000631	0.970		165 ± 21

A comparison of the U4f<sub>7/2</sub> data indicates the 298 K annealed surface has a lower  $\Theta_{DE}$  than the 623 K annealed surface, likely the result of a comparative increase in surface disorder from low-temperature annealing. The transition temperatures, estimated from the intersection of the fitting lines, are summarized in Table 8 as well as the associated uncertainty.

Table 8. Summary of the photoelectron kinetic energy, attenuation length in a  $\text{UO}_2$  lattice (TPP-2M, 99% attenuation), and measured transition temperature of the U photopeaks. The attenuation length illustrates the surface sensitivity of the measurement.

Sample	Peak	Photoelectron Energy [KE]	Attenuation Length [ $\text{\AA}$ ]	Transition Temperature [K]
628K Annealed	$\text{U4f}_{7/2}$	874	63	$476 \pm 91$
298K Annealed	$\text{U4f}_{7/2}$	874	63	$486 \pm 38$
	$\text{U4f}_{5/2}$	863	62	$485 \pm 29$
	$\text{U4d}_{5/2}$	514	43	$500 \pm 59$
	$\text{U4d}_{3/2}$	474	41	$516 \pm 69$

The transition temperature of the 298 K annealed sample, 486 K, is higher than that of the 623 K annealed sample, 476 K. Based on [40], the 298 K annealed sample surface had a higher O/U ratio. The binding energy of the  $\text{U4f}_{7/2}$  peak also indicates that the 298 K annealed sample had a comparatively higher O/U ratio. The centroid of the fitted peak as a function of absolute temperature is plotted as Figure 25. The BE of  $\text{U(IV)O}_2$  is 380.00 eV which is consistent with the 623 K annealed sample above the experimentally determined threshold temperature of 476 K at which the sample surface is primarily  $\text{UO}_2$  [34] [38]. A shift to higher BE indicates uranium oxidation and a shift lower indicates reduction. Both surfaces were therefore slightly hyperstoichiometric with the 623 K annealed surface closer to stoichiometric  $\text{UO}_2$ . Annealing above the transition temperature may have preferentially established the 623 K surface as  $\text{UO}_2$  and retarded the formation of the  $\text{U}_4\text{O}_9$  structure prior to measurement. The BE measurement, with a difference of only 0.1 eV between the maximum and minimum, indicates that the U of both sample surfaces was slightly reduced with increasing temperature but does not show a distinct reduction at the threshold temperature. Therefore, the stoichiometry of the two phases are similar.  $\text{U4f}$  photoelectrons have the highest core-level energy in the dataset

and the deepest sampling depth. The attenuation length in a  $\text{UO}_2$  matrix is approximately 63 Å or 11.5 unit cells as shown in Table 8 [41]. If the surface phase is limited in depth, the U4f signal may sample into the bulk-like sub-surface which would diminish the contribution from higher oxidation states.

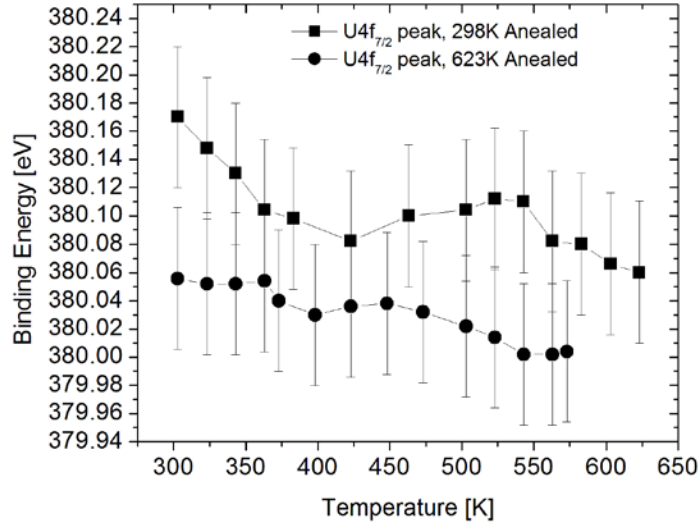


Figure 25. The U4f<sub>7/2</sub> centroid energy measured at different temperatures for both annealing conditions. The surface of both samples was hyperstoichiometric at the onset of measurement and reduced with increasing temperature as evidenced by the shift to lower energy. The 623 K annealed sample is closer to the expected value of 380.00 eV for stoichiometric  $\text{UO}_2$ . The error bars of  $\pm 0.05$  eV are an artifact of the spectrometer energy calibration.

It is also evident that the U5f photopeak, a valence state, does not follow the same intensity diminution shown by the core-levels of the U4d and U4f above the transition temperature. The U5f peak intensity loss is more gradual suggesting the temperature effect is partially offset by an intensity increase. This is also consistent with the reduction of  $\text{U(>IV)}$  to  $\text{U(IV)}$ .

The O1s feature resulting from oxygen in proximity to uranium at 529.9 eV (not depicted) diminishes with increasing temperature consistent with excess oxygen leaving the surface structure. Unfortunately, the Ta-O bond of the sample mount also contributes to this spectral peak. Analysis of the Ta4d<sub>5/2</sub> peak evolution with increasing temperature supports the conversion of Ta<sub>2</sub>O<sub>5</sub> to TaO<sub>2</sub>. Thus, the diminishing O1s signal at 529.9 eV can be explained by TaO<sub>x</sub> and cannot conclusively support the uranium phase change.

The experimentally derived linear expansion coefficient data for polycrystalline UO<sub>2</sub>, measured by [42] as function of temperature, is plotted in Figure 26 on the minor axis along with the U4f<sub>7/2</sub> data for comparison.

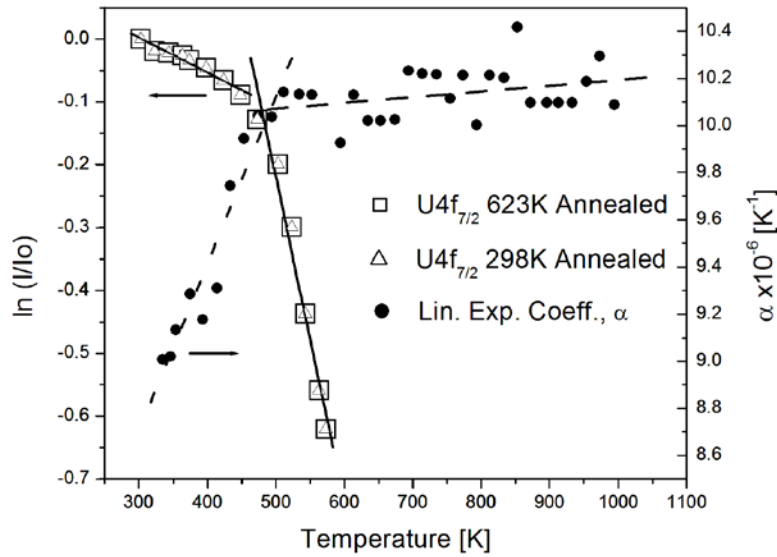


Figure 26. The natural logarithmic ratio of U 4f<sub>7/2</sub> intensity for both surface preparations on the major axis compared to the linear expansion coefficient,  $\alpha$ , for UO<sub>2</sub> as a function of temperature found in the literature on the minor axis [42]. The change in  $\alpha$  occurs at  $\approx 490$  K which is in good agreement with the observed phase change at 476 K determined by XPS.

The regions of constant  $\Theta_{DE}$  intersect near the point identified by [42] at which the lattice expansion coefficient shows a marked change in the expansion rate. The

relationship between the linear expansion coefficient,  $\alpha$ , the lattice parameter,  $a$ , and the temperature,  $T$ , is given by (64) [43].

$$\alpha = \frac{1}{a} \frac{\Delta a}{\Delta T} \quad (64)$$

The data for  $\alpha$  displays two regions of linearity separated at  $\approx 490$  K ( $493 \pm 11$  K) based on the intersection of the two linear fit lines. The data presented by [42] was not derived from a single crystal, does not have an estimate of error, and is scattered near the transition temperature. However, it does corroborate the phase transition temperature for a sample reported to have nominal  $\text{UO}_2$  stoichiometry which is well within the margin of experimental error [42].

#### 4.2.3 Debye Summary

The effective Debye temperature of nearly stoichiometric  $\text{UO}_2$  in the mixed phase of  $(\text{UO}_{2+x} + \text{U}_4\text{O}_{9-y})$  was measured to be  $500 \pm 59$  K for a clean surface annealed under high-vacuum at 623 K for 12 hours. The effective Debye temperature of nearly stoichiometric  $\text{UO}_2$  in the single  $(\text{UO}_{2+x})$  phase was measured to be  $165 \pm 21$  K on the same surface heated beyond the phase transition temperature. The transition temperature was experimentally measured to be  $476 \pm 91$  K. Corroborating photoemission measurements support both the near- $\text{UO}_2$  stoichiometry and the phase transition temperature which is also in good agreement with published data indicating an abrupt change in the linear expansion coefficient of the  $\text{UO}_2$  lattice. The measured  $\text{UO}_2$

effective surface Debye temperature is lower than the published range of bulk  $\text{UO}_2$  Debye temperatures which is 182 to 377 K [40] [44]. This is not unexpected as commonly occurring, stable  $\text{UO}_2$  surfaces are expected to relax at the lattice-vacuum interface where long-range order is abruptly halted [45] [46]. Despite the refractory nature of  $\text{UO}_2$  which melts above 3000 K, the effective Debye temperature is quite low. This has several important implications for the production of  $\text{UO}_2$  based semiconducting devices. The crystal surface should readily accept dopants by ion implantation or diffusion but will be hindered by the presence of a stiffer, mixed-phase surface region which has an effective Debye temperature higher than that reported for bulk  $\text{UO}_2$ . Additionally, the operation of such devices would necessarily need to remain below the phase transition temperature which is likely a factor of dopant concentration just as it is a function of the O/U ratio. The reorganization of the crystal structure may adversely affect the special arrangement of the dopant concentration and deleteriously effect device operation. To first order, this limit can be estimated by the transition temperature of stoichiometric  $\text{UO}_2$  which is approximately 470 K (197 °C). Common integrated circuits have maximum temperature operating limits of 70 °C and maximum storage temperature limits of 150 °C [47]. Neglecting the temperature-dependent atomic diffusion of a dopant which may occur at lower temperature, the phase transition temperature does not appear to restrict the operation of doped  $\text{UO}_2$  devices.

### **4.3 Work Function Measurements**

Two oriented samples UO2-T-29b (111) and UO2-T-29a (100) were grown large enough for work function measurements. As such a measurement relies on the collection



of low energy photoelectrons, the sample must completely fill the analyzer field of view which was experimentally measured to be a rectangle 6 mm high by 10 mm wide.

#### 4.3.1 Experiment and Analysis

The photoelectric work function,  $\Phi_{PES}$ , was determined by x-ray photoemission. Spectra were measured of the secondary electron cut-off region using a pass energy of 100 eV and a 20 meV step-size. A Keithley 2200-60-2 precision power supply was used to provide a 10 V potential between the analyzer and the sample to separate low-energy spectrometer artifacts from the secondary electron cut-off (SEC). This placed the Fermi level of each sample at a binding energy of -10 eV. Each work function value was then determined by a linear fit to the SEC and corrected by 0.43 eV, one-half of the full-width at half-maximum of the 0.85 eV Al K $\alpha$  line-width [12]. Measured values have an associated uncertainty of  $\pm 0.36$  eV due primarily to the excitation photon width.

Measurements were taken continuously every 3.3 minutes beginning 7 minutes post-sputter to observe the effects of surface reconstruction at 299 K and  $4.7 \times 10^{-8}$  Torr. A polynomial fitting of the early data provided an estimate of the work function immediately upon cessation of sputtering. These values are 5.66 eV (111) and 5.56 eV (100). For sake of comparison, the work function of U metal at 300 K is  $3.54 \pm 0.03$  eV [48].

Figure 27 provides the initial and maximum measured  $\Phi_{PES}$  of the (111) surface determined by the linear fitting of the secondary electron cutoff. The energy scale is corrected for bias and photon line-width. The shift indicates a work function change.

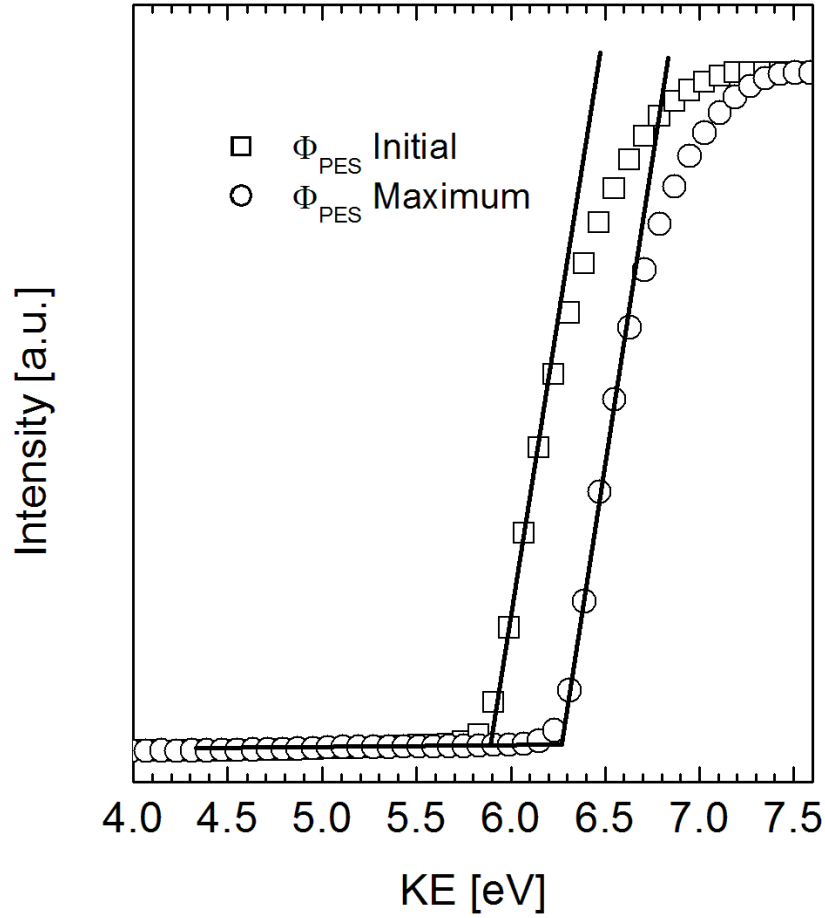


Figure 27. The work function of the (111) sample was obtained by a linear fitting of the secondary electron cut-off. The initial measurement and a subsequent measurement which yielded the maximum value are depicted along with the respective linear fits. The depicted energy scale is corrected for the photon line width.

The time dependent  $\Phi_{PES}$  for both (110) and (100) crystal surfaces are presented in

Figure 28. Both surfaces exhibit an increase in  $\Phi_{PES}$  following the initial measurement which eventually stabilizes within 5% above the initial measured value. The changing work function can be explained by surface reconstruction after Argon ion sputtering an oxygen-deficient, non-stoichiometric condition resulting from the unequal sputtering yields of U and O as well as the influence of vacuum reduction [49] [35]. Oxygen

diffusion from the near-surface is expected to be rapid initially [50], slowing as the surface approaches stoichiometric  $\text{UO}_2$  [50] [51]. Interstitial migration in the fluorite structure is more rapid in the  $\langle 111 \rangle$  direction than the  $\langle 100 \rangle$  direction [51] and the energy of the (100) surface is approximately three times higher than that of the more stable (111) surface [52] [53], both of which explain the comparatively different work function change rates. The maximum work function values were interpreted to be those of the stoichiometric  $\text{UO}_2$  surface. Alternatively, the extent of uranium oxidation on the (111) surface may have been greater than that of the (100) surface at the maximum values.

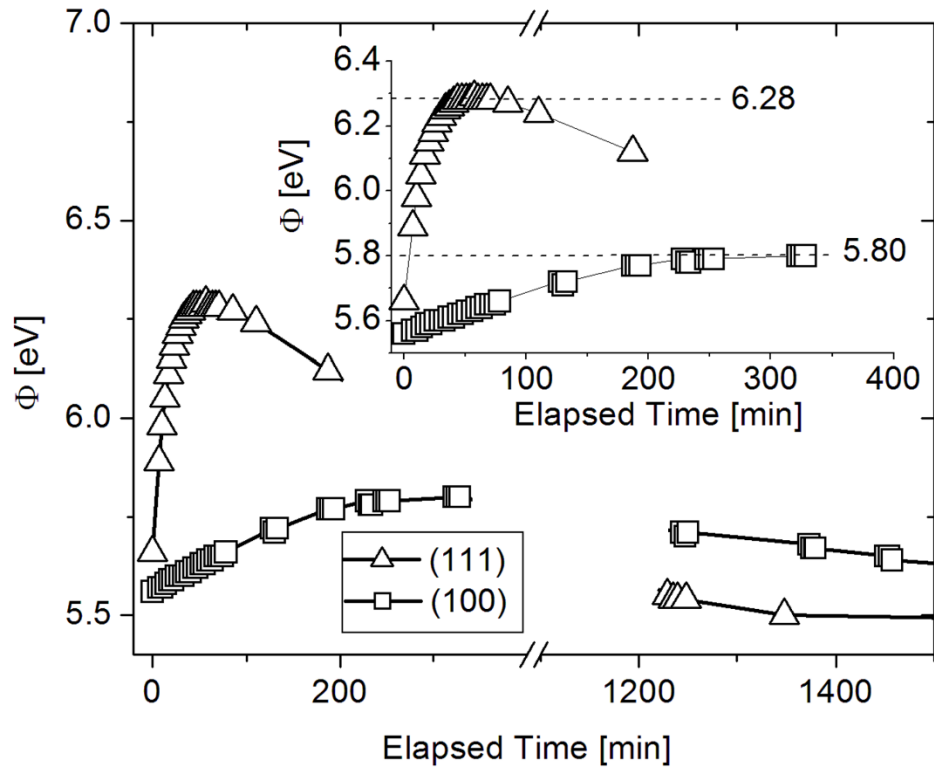


Figure 28. The time-evolution of the work function for the (111) and (100)  $\text{UO}_2$  surfaces. In the figure's inset, an extrapolation of the trend provides an estimate of the initial work function at cessation of sputtering ( $t=0$ ); 5.66 eV (111) and 5.56 eV (100). The maximum values are 6.28 eV (111) and 5.80 eV (100). Error bars of  $\pm 0.36$  eV are omitted for clarity.

The oxidation of  $\text{UO}_2$  is accomplished by the depopulation of the 5f state which constitutes the valence band maximum. The formation of  $\text{UO}_3$  on the surface would effectively create a dielectric barrier and a corresponding increase in the work function [54]. The formation of  $\text{UO}_3$  on the surface within the short timeframe and under high vacuum and low-temperature conditions seems unlikely. However, an oxidation study of finely divided  $\text{UO}_2$  (particle diameters  $< 200$  nm) concluded that oxidation proceeded from  $\text{UO}_2$  to clusters of both  $\text{U}_4\text{O}_9$  and  $\text{UO}_3$  directly without the formation of the intermediate oxides  $\text{U}_3\text{O}_8$  and  $\text{U}_3\text{O}_7$  which form prior to  $\text{UO}_3$  in bulk measurements at room temperature [55]. Although the surface geometry of small particles is much different than the single crystal surface, it does suggest low-temperature formation of  $\text{UO}_3$  is possible although further investigation would be needed.

The decrease in the measured work functions may be caused by the adsorption of contaminants, to include water, even under the vacuum conditions [56] [57]. This is supported by a work function of 5.3 eV measured on the (111) as-grown crystal surface prior to sputtering which is lower than all measured values post-sputter.

#### **4.3.2 Reconstruction Kinetics**

A large part of surface reconstruction may be the re-oxidation of the reduced, oxygen defected surface back to U(IV) and to some extent, higher oxidation states. The transport of oxygen to the reactive surface suggests a diffusion controlled process. Considering the formation of a reconstructed layer at the crystal surface, it would be expected that the average layer thickness,  $\bar{x}$ , would be governed in time,  $t$ , by the

diffusion of oxygen either from within the crystal bulk or from the partial pressure of the vacuum. This is described mathematically by (37) in which  $D$  is the diffusion coefficient [35].

$$\bar{x} \propto \sqrt{Dt} \quad (65)$$

Assuming the growth of the reconstructed layer is responsible for the changing work function and the information depth of the PES measurement is sufficient to measure it, the average layer thickness is considered proportional to the work function changes depicted in Figure 28. The natural log of  $\Delta\Phi$  as a function of the natural log of  $t$  for the (111), (100), and the average of the two surfaces is shown in Figure 29. A linear fit of the data provides the slope,  $m$ , following (66), expected to be near  $\frac{1}{2}$  indicated by (65).

$$\ln(\Phi_t - \Phi_0) = m \ln(t) + b \quad (66)$$

The (111) surface generally displays the expected  $(Dt)^{1/2}$  behavior of a simple diffusion controlled process. The averaged surface, a first-order representation of a polycrystalline sample, dominated by the relatively higher magnitude of the (111) measurement, fits the diffusion controlled relation well.

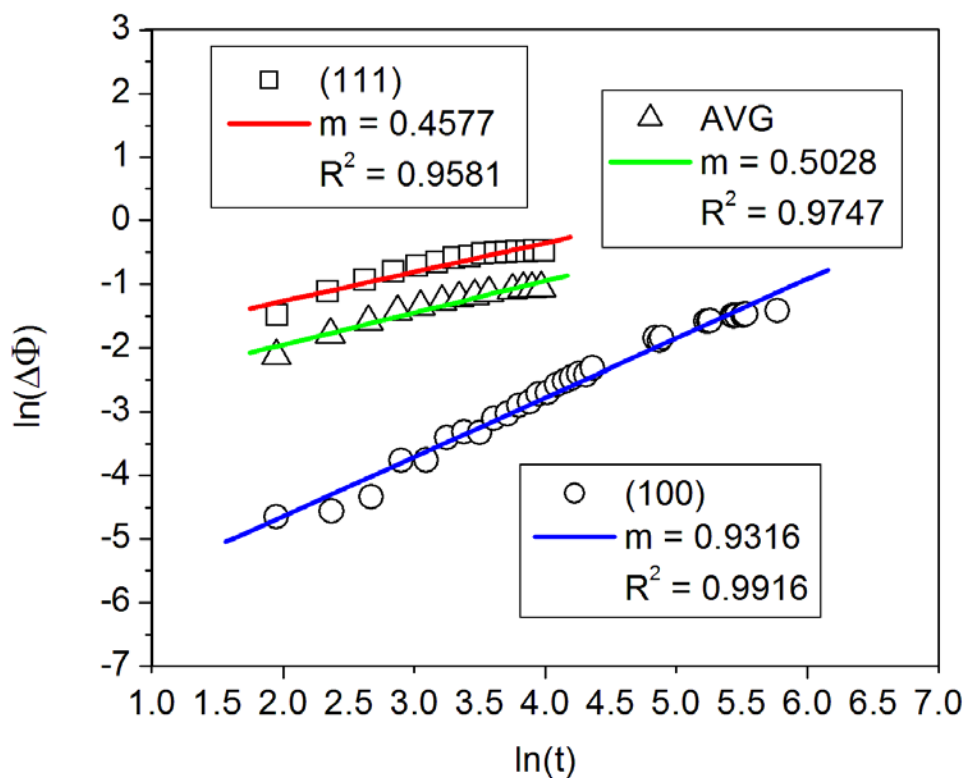


Figure 29. The log of the work function change plotted with respect to the log of time for the reconstructing surfaces.

This implies that the (111) and (100) surfaces, reconstructing under identical conditions, are governed by a different time-dependent mechanism; the (111) surface appears to change with a diffusion-controlled process and the (100) surface by a zero-order process. With some speculation, the excellent fit of the averaged data suggests that the diffusion-controlled oxidation process identified for poly-crystalline  $\text{UO}_x$  may in fact be an aggregate result of the disparate oxidation process of Wulff-shaped particles nominally comprised of {111} and {100} surfaces [58]. However, this cannot be concluded with the available data.

A body of research exists on the oxidation rate of  $\text{UO}_x$  under the conditions of either elevated temperatures, oxygen partial pressure, or both, but less is published for the low pressure and low temperature regime [35] [59] [60] [61]. However, the time-dependent work function data for both the (111) surface as well as the averaged data was compared to the work of [35] in which the rate of in-growth of U(VI) on the surface of a partially reduced poly-crystalline  $\text{UO}_3$  sample was measured. Although the photoluminescent (PL) emission measurement was conducted under 760 Torr of  $\text{O}_2$  pressure, the sample temperature was also 25 °C [35]. The change of work function between the first measured and maximum values along with the corresponding times was compared to the same ratio of PL emission intensity. The time constant, given by (67) which is expressed in terms of the work function, was calculated as 0.35 for the (111) sample and 0.36 for the averaged data. Both values are approximately half of the 0.69 value calculated from the PL measurement data.

$$\frac{\Phi_1}{\Phi_2} = \sqrt{\frac{D t_1}{D t_2}} = \sqrt{\frac{t_1}{t_2}} \quad (67)$$

#### 4.3.3 Work Function Summary

The first ever photoelectric work functions of the (111) and (100) surfaces of hydrothermally grown  $\text{UO}_2$  were measured at  $6.28 \pm 0.36$  eV (111) and  $5.80 \pm 0.36$  eV (100). Both values seem reasonable as they reference the valence band maximum and are approximately 2 eV, the  $\text{UO}_2$  band gap, greater than the work function of U metal. This result is encouraging and supports the predictability of prepared  $\text{UO}_2$  surfaces for electronic device fabrication [62].

#### **4.4 Identification of Cs Contamination by XPS**

The CsF mineralizer is highly soluble and not expected to entrain or deposit within the synthesized crystals. Analysis by XRF with a detection threshold on the order of 100 ppm, or 0.01 a/o, identified Cs in only two samples. In both cases, it was in concentrations below 1 a/o, detected at multiple sample locations, and appeared homogeneously distributed. One of the samples was produced in the same reaction as two other crystals which did not contain Cs. During the cool-down from growth conditions, it is possible that the mineralizer precipitated onto the surface of the crystals as it is common for gross contaminants to adhere to the grown crystals when they are removed from the reaction vessel. This surface is removed by sonication in deionized water. Although it is possible that the Cs contamination was limited to the surface, other samples which did not indicate Cs by XRF analysis, did contain Cs as identified by XPS after several hours of sustained heating above 200 °C. In these cases, it is believed that the Cs migrated to the surface and concentrated above the XPS threshold for detection, approximately 10,000 ppm, or 1 a/o. This was further confirmed by removing the Cs enriched surface by Ar ion sputtering and re-measuring. The Cs, initially absent at room temperatures, re-appeared after similar heating conditions.

##### **4.4.1 Temperature Dependence of Cs Migration**

The temperature-dependent migration of Cs to the surface was studied using XPS analysis of the U4d and Cs3d region in the binding energy range of 790 and 720 eV. The XPS spectrum at 70 °C is shown in Figure 30.



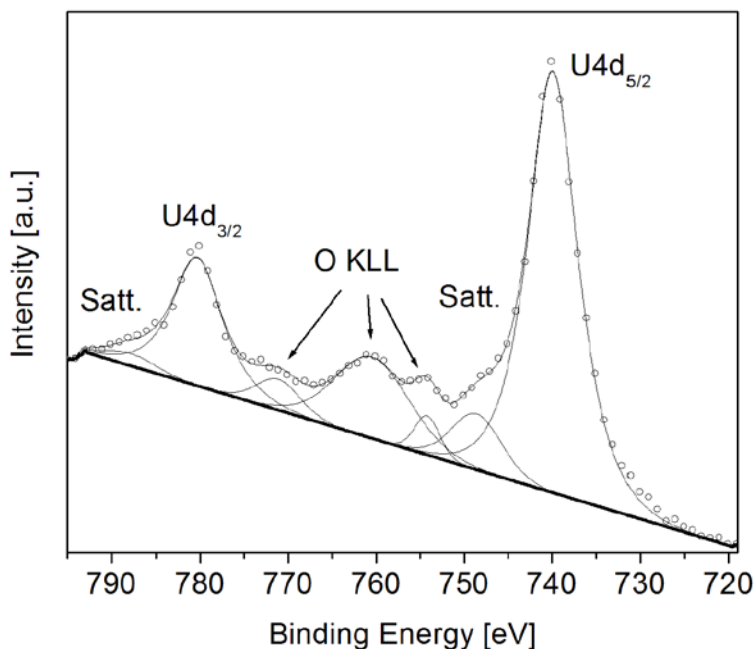


Figure 30. XPS spectrum of the U4d region using Mg  $k\alpha$  radiation on the clean  $\text{UO}_2$  surface at 70 °C showing the  $\text{U4d}_{3/2}$  and  $\text{U4d}_{5/2}$  peaks with the O KLL Auger in the center. The U4d shake-up satellites are also observed.

The most prominent peak is the  $\text{U4d}_{5/2}$  at 740 eV and Cs is not visible. After heating the sample to 350 °C for several hours, the Cs signal is clearly evident in the spectrum presented as Figure 31 in which a  $\text{Cs4d}_{5/2}$  peak at 725 eV has appeared and the peak at 740 eV now has a contribution from both  $\text{U4d}_{5/2}$  and  $\text{Cs4d}_{3/2}$ . The Cs4d feature is the most intense doublet and the degeneracy of the d-shell is used to fit the intensities of the  $\text{Cs4d}_{3/2}$  and  $\text{Cs4d}_{5/2}$  peaks at the ratio of 2:3. Because the intensity of both the U and Cs core lines are diminished at elevated temperature, a comparison of the ratio of Cs to U accurately describes the increased Cs concentration at the crystal surface with respect to the U.

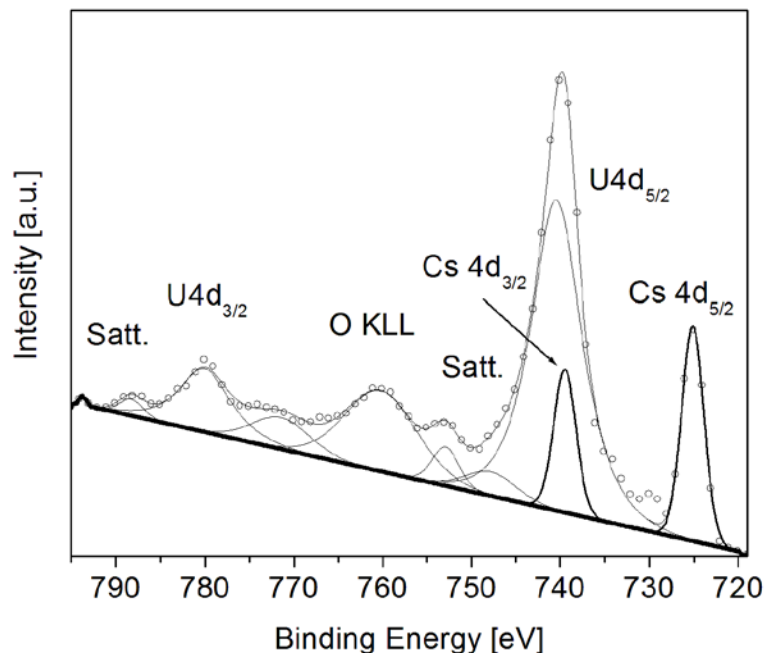


Figure 31. XPS spectrum of the U4d region using Mg  $k\alpha$  radiation held at 350 °C for several hours showing the Cs4d<sub>3/2</sub> and Cs4d<sub>5/2</sub> peaks along with the U4d and O KLL Auger features. The core U lines are diminished by the Debye effects at elevated temperature which is most striking for the U4d<sub>3/2</sub>.

#### 4.4.2 Temperature Threshold of Cs Diffusion

The sample was sputtered and held at nine different temperatures, each for a period of 5 hours, in which the U4d region was measured 12 times. The spectrum was fitted and the ratio of the Cs4d<sub>3/2</sub> to U4d<sub>5/2</sub> intensity was plotted as a function of the sample temperature, summarized in Figure 32. The line is a least squares fit of the data and clearly shows a point near 475 K at which the Cs/U ratio is markedly increased. This threshold temperature is similar to the phase change temperature identified in the Debye measurements.

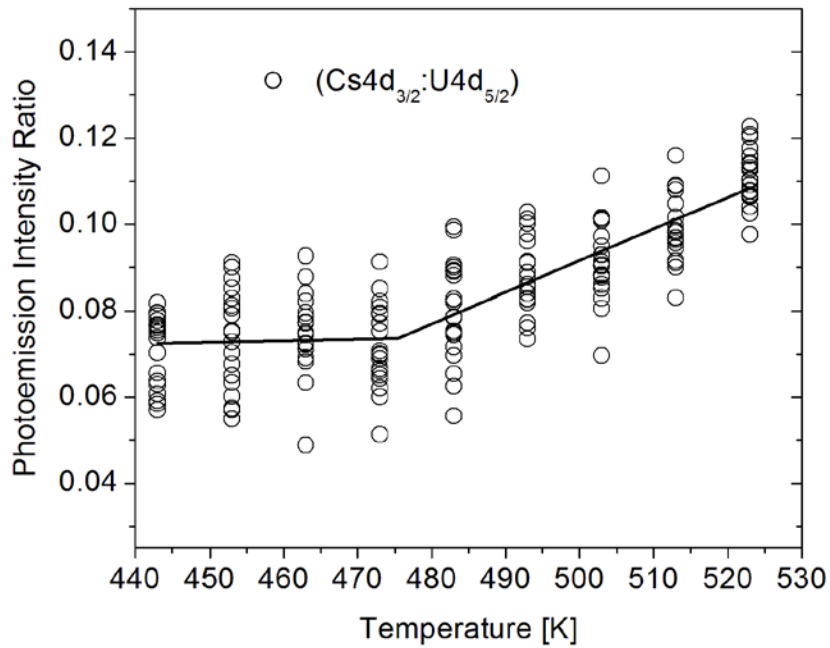


Figure 32. Ratio of the  $U4d_{5/2} : Cs4d_{3/2}$  intensity as a function of sample temperature.

If the threshold temperature is indeed the same as that determined by Debye measurements, the two regions of Cs concentration with respect to sample temperature correspond to a phase change from a mixed ( $UO_{2+x} + U_4O_{9-y}$ ) phase to a ( $UO_{2+x}$ ) phase which is clearly preferential to Cs migration. The implications of this finding are two-fold: the growth process may in fact produce crystals with Cs impurities and the impurities move to the surface rapidly above 475 K. From a crystal purity perspective, the distribution of the Cs must be determined in order to generalize these results from the surface to the bulk of the crystal. The impurities may also be preferentially concentrated at the surface by heating above 475 K where it can be removed. Were impurities

purposely implanted for electronic doping, impurity migration, once implanted, can be reduced by avoiding a phase change.

## V. Contact Study

### 5.1 Determination of Candidate Metals for Electrical Contacts

An important result of measuring  $\Phi_{PES}$  is for assessing metals for electronic contacts. The relationship between the metal work function,  $\Phi$ , and the electronegativity,  $X$ , of the  $\text{UO}_2$  semiconductor establishes the energy barrier presented to charge carriers. In the flat band approximation,  $X$  is obtained by subtracting the band gap from  $\Phi_{PES}$ . Since the band gap was not measured in this research,  $2.1 \pm 0.1$  eV was used as established in [63] [64]. Thus, our measured values indicate  $X$ , as 4.2 eV (111) and 3.7 eV (100) both  $\pm 0.4$  eV. For comparison,  $X$  for GaP, with a band gap of 2.26 eV, is 4.0 eV [15].

In the absence of Fermi level pinning, the Schottky-Mott relationship describes the barrier height,  $\phi_b$ , of a metal-semiconductor junction in terms of  $\Phi$  and  $X$  [15]. Equations (48) and (49) estimate the barrier when the semiconductor is strongly n-type or p-type as denoted by the subscripts  $n$  and  $p$ . In the case of stoichiometric  $\text{UO}_2$ , equating  $\phi_{bn}$  and  $\phi_{bp}$  and solving for  $\phi_m$  predicts a minimum barrier (the Ohmic condition) when the work function is equal to half of the band gap plus the electronegativity. This is in contrast to a rectifying, or Schottky contact, which results from a large barrier.

Another consideration related to making electrical contacts, from a crystallographic perspective, is the lattice compatibility at the contact metal and semiconductor interface. Strain is reduced when the metal lattice spacing is similar to that of either the fluorite  $\text{UO}_2$  unit cell, 5.471 Å, or the complementary sub-lattice cell spacing of 3.87 Å; found on both (111) and (100) surfaces. Figure 33 represents the conventional

unit cell (a) as well as the (100) surface (b), in which both lattice parameters of interest are indicated.

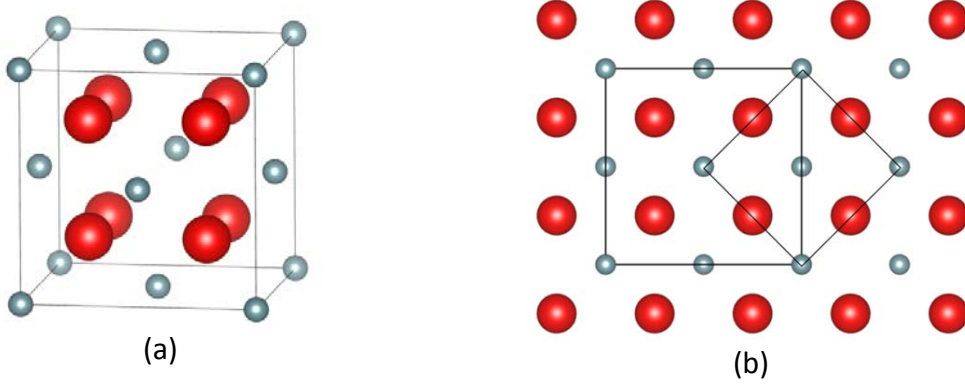


Figure 33. The (100) surface viewed from the  $\langle 100 \rangle$ . The oxygen atoms (large spheres) are red, the uranium atoms (small spheres) are blue. The drawing is scaled by ionic radius. The conventional unit cell is illustrated by the nine uranium atoms of the FCC-like (100) in which four oxygen atoms are located. The sub-cell is offset by  $45^\circ$ .

A particular metal is considered an acceptable contact candidate if the lattice parameter matches to within 10% of  $3.87 \text{ \AA}$  or  $5.47 \text{ \AA}$  and the work function is i) within 10% of that required for an Ohmic contact or ii) greater than a 10% difference for a Schottky contact (considering only the magnitude of the work function mismatch). In confirmation of our method, we have observed the rapid growth of  $\text{UO}_2$  on a Cu surface ( $\text{Fm}3\text{m}$ ,  $a = 3.61 \text{ \AA}$ ) which may be explained by a close match of the sub-lattice orientation. In order to reduce potential metal contact materials to a list of practical choices, metals with a resistivity less than  $12 \times 10^{-8} \Omega \text{ m}$  at 300 K were considered. Using this methodology, candidate metals for electrical contacts on hydrothermally grown  $\text{UO}_2$  are given in Table 9.

Table 9. Candidate metals for electrical contacts. The parenthetical value following the contact type in the two rightmost columns indicates the order of best agreement.

Candidate Contact Metal	Work Function <sup>+</sup> [eV]	Lattice Constant <sup>++</sup> [Å]	Resistivity @300K, 1 atm <sup>++</sup> [ $\times 10^{-8} \Omega \text{ m}$ ]	UO <sub>2</sub> (111)	UO <sub>2</sub> (100)
Zn	3.63	2.67, 4.95	6.06	Schottky (1)	Schottky (1)
Mg	3.66	3.21, 5.21	4.51	Schottky (2)	Schottky (2)
Cd	4.08	2.98, 5.62	6.80	Schottky (3)	
Cu	4.65	3.61	1.73		Ohmic (1)
Be	4.98	2.29, 3.58	3.76		Ohmic (2)
Co	5.00	2.51, 4.07	5.60	Ohmic (5)	Ohmic (3)
Au	5.10	4.08	2.27	Ohmic (3)	Ohmic (4)
Ni	5.15	3.52	7.20	Ohmic (2)	Ohmic (5)
Pd	5.22	3.89	10.80	Ohmic (1)	
Pt	5.50	3.92	10.80	Ohmic (4)	Schottky (3)

<sup>+</sup> [65]    <sup>++</sup> [66]

## 5.2 Evaluation of Experimental Contacts

Contacts were fabricated using a paint/melt deposition technique as well as mechanical placement. The paint/melt contacts were fabricated by application of Ag and GaIn to opposing sides of a fragment of the UO<sub>2</sub>-T-29b (111) sample. Mechanical contacts were made by pressing sharpened tungsten pins into opposing facets of two crystals, UO<sub>2</sub>-T-11a and UO<sub>2</sub>-T-T11b. The choice of metals was made primarily based on availability and convenience. Thin Cu wires were then affixed to the contacts allowing

current-voltage,  $I(V)$ , and capacitance-voltage,  $C(V)$ , measurements using a semiconductor analyzer system. The paint/melt two-point circuit used the Ag contact as the positive voltage reference. The work function of polycrystalline Ag is 4.26 eV, slightly higher than that of GaIn, 4.1 - 4.2 eV [67]. It was assumed that rectification resulted from the Ag/ $\text{UO}_2$  interface since the measured electronegativity of the  $\text{UO}_2$  (111) surface is 4.2 eV. The mechanical contacts were electronically symmetrical and rectification was possible given the work function of polycrystalline W is 4.6 eV.

### 5.2.1 Current-Voltage Measurements

The  $I(V)$  measurement of an Ag/ $\text{UO}_2$ /GaIn device is presented as Figure 34. The larger current values with positive applied voltage indicate a dominant Schottky junction with n-type semiconductor. This is unexpected as  $\text{UO}_2$  should either insulate or become p-type with hyperstoichiometry; the expected surface condition after several days of exposure to ambient oxygen pressures. The absolute value of the forward and reverse bias data are compared side-by-side in Figure 34 to confirm n-type behavior. The larger current response at positive voltage suggests the barrier is lowering with positive voltage on the Ag contact. If the material was p-type, the barrier would decrease with negative voltage on the Ag contact and the opposite response would be observed. The barrier is predicted by (48) to be 0.06 V assuming an abrupt junction and absence of an interface layer. The generally Ohmic response, similar to a 714.3  $\Omega$  resistor at low voltages, seems to support this.



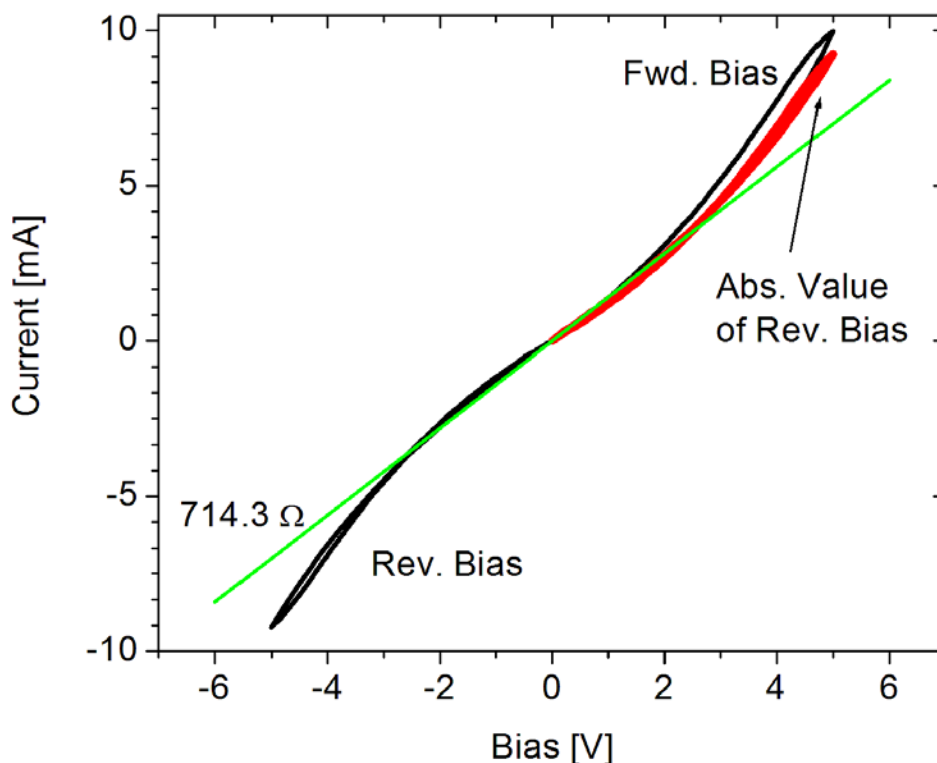


Figure 34. The I(V) response of the Ag/UO<sub>2</sub>/GaIn device. The response was generally Ohmic with a larger rectification in the forward bias. The absolute value of the reverse bias data is displayed alongside the forward bias data for comparison. A reference line representing a 714.3  $\Omega$  is displayed for reference.

The I(V) measurements of the W/UO<sub>2</sub>/W devices are presented in Figure 35 along with the Ag/UO<sub>2</sub>/GaIn device for reference. The current response of the Ag/UO<sub>2</sub>/GaIn device is an order of magnitude higher but has a similar shaped response curve to the T11b W/UO<sub>2</sub>/W device. The response curve of the T11a and T11b devices are not identical despite crystal similarity but do show forward and reverse bias symmetry as expected. The dissimilar current response is probably caused by the contact to crystal junction which is sensitive to contact pressure.

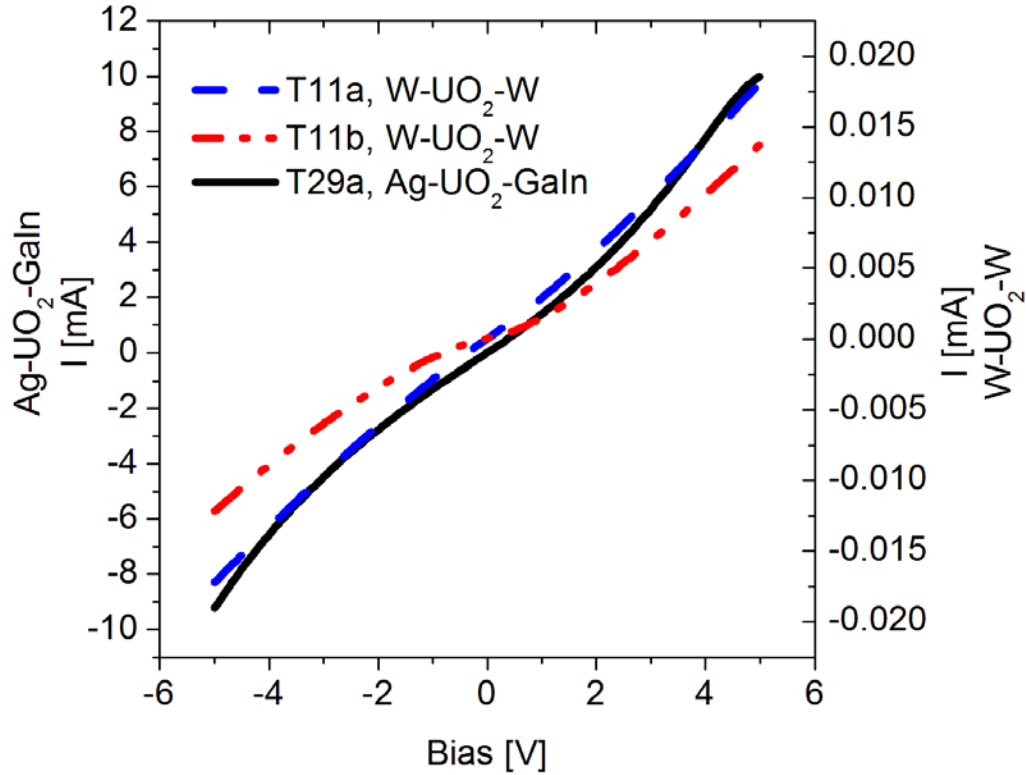


Figure 35. The  $I(V)$  measurements of the  $W/UO_2/W$  devices and the  $Ag/UO_2/GaIn$  device. The response of the  $Ag/UO_2/GaIn$  device is an order of magnitude higher but has a similar response curve to the T11b  $W/UO_2/W$  device. The LEFT vertical axis corresponds to the T29a sample. The T11 sample current is on the RIGHT side vertical axis.

### 5.2.2 Capacitance-Voltage Measurement

$C(V)$  data was collected for the  $Ag/UO_2/GaIn$  device and was analyzed to estimate both the dominant carrier concentration and the built-in voltage of the metal/semiconductor interface. The large current response (mA range) and lack of distinct rectification absent from Figure 34 makes  $C(V)$  derived information prone to error especially when transconductance is large. The energy band diagram of the junction is interpreted in Figure 36 which assumes that the semiconductor is n-type. The

upward bending of the bands at the interface also assumes the work function of the metal is greater than that of the semiconductor which is not the case for  $\text{UO}_2$ . However, it is helpful for visualizing the extraction of the built-in voltage,  $V_{bi}$ , from the  $C(V)$  data.

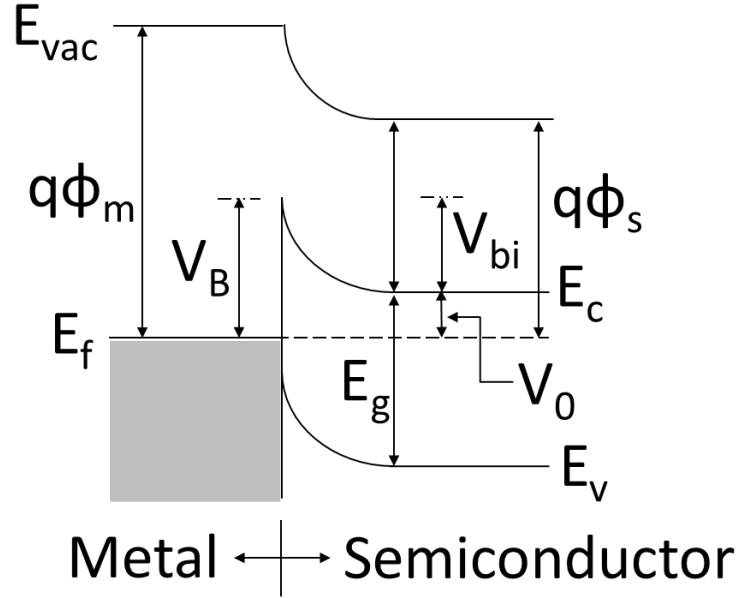


Figure 36. The energy level diagram for an abrupt metal to n-type semiconductor junction adapted from [18].

The barrier height, expressed as a voltage,  $V_B$ , has contributions from  $V_0$  and  $V_{bi}$ . The bending of the energy bands to align the Fermi level produces the built-in voltage. The difference in potential between the Fermi level and the conduction band minimum of the semiconductor produces  $V_0$ . The barrier to electron flow from the semiconductor into the metal is quantified by  $V_{bi}$ , given by (68), which is the difference between the junction barrier,  $V_B$ , and  $V_0$ .  $V_0$  is estimated by (69) in which  $N_c$  and  $N_d$  are the effective density of states in the conduction band and donor band respectively.

$$V_{bi} = V_B - V_0 \quad (68)$$

$$V_0 = -kT \ln \left( \frac{N_c}{N_d} \right) = E_c - E_f \quad (69)$$

Capacitance is defined by (70) in which the static permittivity,  $\epsilon_s$ , is approximated by  $22\epsilon_o$  for  $\text{UO}_2$ , where  $\epsilon_o$  is the vacuum permittivity [68]. The depletion width in the semiconductor bounded by the metal junction is  $W_d$  and the cross-sectional area of the junction is  $A$ .

$$C = \frac{\epsilon_s}{W_d} A \quad (70)$$

A depletion width of 2 nm is computed using (70) to attain the measured  $C/A$  of 0.35 nF/m<sup>2</sup> at 0 V, a reasonable value. The depletion width of the 1-sided abrupt junction is given by (71) in which  $V$  is an applied bias across the device and  $q$  is the elementary charge. Combining (70) and (71) yields (72).

$$W_d = \sqrt{\frac{2 \epsilon_s (V_{bi} + V)}{q(N_d)}} \quad (71)$$

$$\left( \frac{A}{C} \right)^2 = \frac{2}{q N_d \epsilon_s} (V_{bi} + V) \quad (72)$$

A plot of  $\left( \frac{A}{C} \right)^2$  as a function of  $V$  yields a slope of  $\frac{2}{q N_d \epsilon_s}$  and a y-intercept of  $V_{bi}$ . Such a plot is presented as Figure 37 which shows non-linear behavior for negative bias. The data was taken from 0 to 10 V, down to -10 V, and back again. The capacitance values exhibit hysteresis beyond -5 V, a phenomenon possibly attributed to persistent carrier

trapping in the depletion region. However, this cannot be confirmed with the available data.

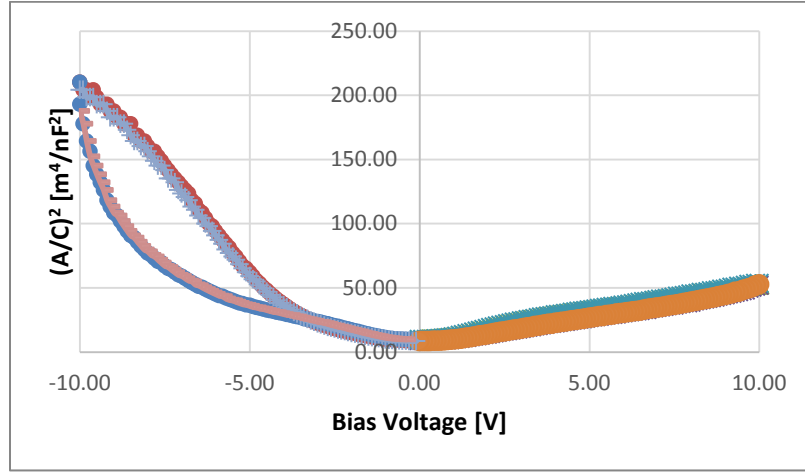


Figure 37. A plot of  $(A/C)^2$  vs  $V$ . The measurement started and ended at 0 V, scanning out to  $\pm 10$  V twice, which produces multiple values for the same bias.

A linear fit of the region between -3.5 and 0 V yielded a  $V_{bi}$  of 0.5 V. The slope provided an estimate of  $N_d$  at  $5 \times 10^9$  [1/m<sup>3</sup>].  $N_c$  was estimated between  $1 \times 10^{23}$  and  $1 \times 10^{25}$  [1/m<sup>3</sup>] using (73) and a range of electron effective masses,  $m^*$ , between 0.05 and 1.1  $m_e$ , in which  $k$  is Boltzmann's constant,  $T$  is absolute temperature, and  $h$  is Planck's constant. The true value of  $m^*$  is not known and the range was chosen from known semiconductor values.

$$N_c = 2 \left( \frac{2 \pi m^* kT}{h^2} \right)^{3/2} \quad (73)$$

$V_0$  was estimated to be 0.8 V. The full barrier height is thus 1.3 V which is much higher than the estimate of 0.06 V.

### 5.2.3 Implications of I(V) and C(V) Measurements

One possible interpretation of the data is that the  $\text{UO}_2$  at the interface may have a bulk n-type to surface p-type transition. Although stable under vacuum, it has been observed that the surface of the  $\text{UO}_2$  crystal will oxidize in the atmosphere; the condition under which the sample was stored for several weeks prior to contact placement. It is thus highly likely that a thin, hyperstoichiometric region was present at the metal-semiconductor interface. The presence of this p-type region is supported by the C(V) measurement which is junction sensitive. It is postulated that the shallow depth of this layer suppresses the effect on the I(V) curve which is consistent with an n-type material. In addition, the generally Ohmic response of the bulk I(V) measurement supports the theoretically small (0.6 V) barrier expected of an n-type material.

## VI. Pulse Discrimination Experiment

### 6.1 Motivation and Purpose

The primary purpose for characterizing hydrothermally synthesized  $\text{UO}_2$  is the determination of suitability for solid-state radiation detection applications. Although primarily envisioned for neutron detection, the response to  $\gamma$  and  $\alpha$  radiation is important to understanding the inherent background signal of the material and the development of discrimination techniques to determine the signal origin. Additionally, alpha radiation (as well as ions) can be used as a low-energy surrogate for the detection of fission fragments following a fission event due to their charge and short path length.

### 6.2 Experiment

A rudimentary radiation detector was fabricated from a  $\text{UO}_2$  crystal and the response to different radiation sources was observed. Analysis of the data did not conclusively demonstrate successful detector operation. Several challenges to successful detector implementation were identified as well as post-processing schemes.

#### 6.2.1 Detector and Instrumentation Scheme

A  $\text{UO}_2$  crystal, UO2-T-11a, was developed into a potential resistive device by application of two mechanical tungsten contacts on opposing facets. The contacts were held under constant force by applying spring-tension within an insulating Lucite block. A magnified image of the device is shown in Figure 38. The resistive  $\text{UO}_2$  *device* became a resistive  $\text{UO}_2$  *detector* by the addition of a pulse processing chain as illustrated in Figure 39.

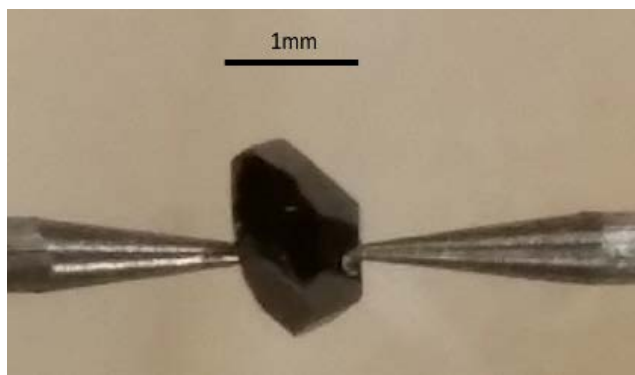


Figure 38. A magnified image of the UO<sub>2</sub> crystal with mechanical tungsten contacts applied.

In most resistive detection schemes, a shaper would be employed following the preamplifier output (e.g. for direct pulse height analysis), but in this experiment only the unshaped signal was considered in order to retain all possible information in the tails of the preamplifier output. As the signals were digitally sampled, stored, and post-processed, this allowed digital shaping of the signals in a post processing program if desired. To this end, an Ortec 142 PC charge sensitive, externally-powered preamplifier was used to collect the voltage signal and provided a convenient means to connect an ORTEC 478 power supply for detector biasing. A Tektronix DPO 7104 oscilloscope was used to capture and digitize the data. A low-pass filter was employed for noise suppression and a grounded aluminum Faraday enclosure surrounded the device to suppress electromagnetic interference.



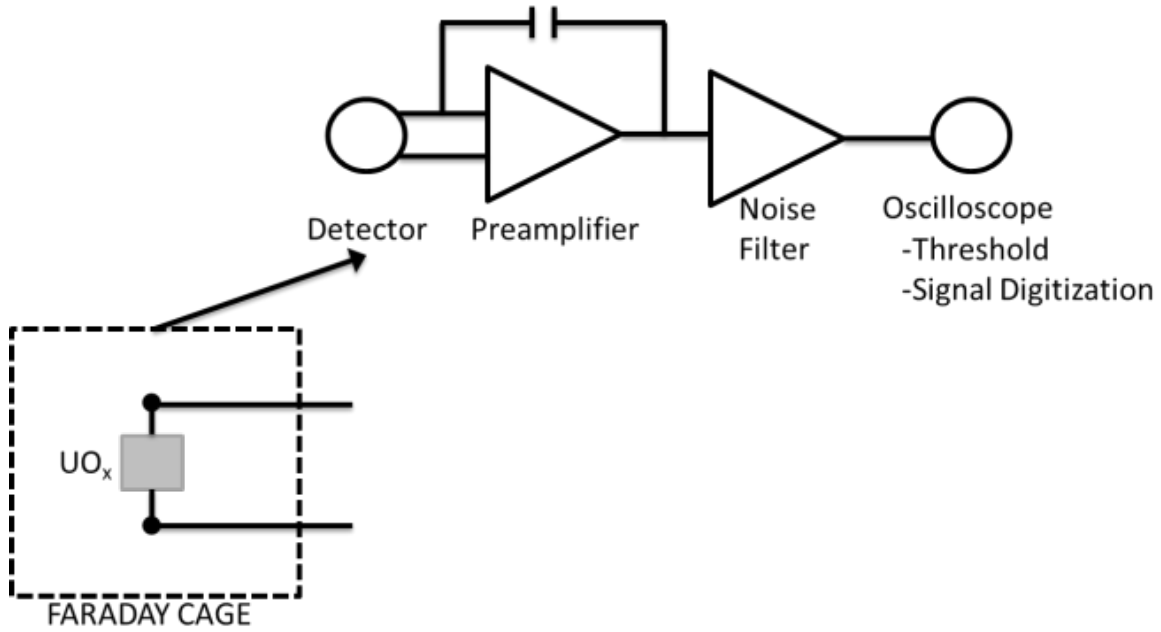


Figure 39. Diagram of the pulse detection instrumentation scheme.

### 6.2.2 Estimation of Detector Background and Expected Signal Parameters

It was assumed, based on the resistive nature of the  $I(V)$  data, that the depleted region at the metal-semiconductor volume was much smaller than the crystal volume. The active volume was modeled as a hemispherical region about each contact with a radius of  $9\text{ }\mu\text{m}$ , the attenuation length of a  $4\text{ MeV } \alpha$  particle as determined by Monte Carlo simulation using the software package SRIM [69]. Assuming both regions about the contacts contribute, the active volume was estimated to be  $3 \times 10^{-9}\text{ cm}^3$ .

The expected background signal of the depleted uranium crystal consists of alpha particles and gamma-rays from the decay sequence of  $^{238}\text{U}$ . Assuming secular equilibrium, the primary contributions are expected from  $^{238}\text{U}$ ,  $^{234}\text{U}$ , and  $^{230}\text{Th}$  as outlined in Table 10.

Table 10. The primary  $^{238}\text{U}$  decay chain contributions to the crystal background.

Conversion	$t_{1/2}$ [y]	$\alpha$ Energy	$\gamma$ Energy	frequency
$^{238}\text{U}$ to $^{234}\text{Th}$	$4.47 \times 10^9$	4.2 MeV	0.013 MeV	9%
$^{234}\text{U}$ to $^{230}\text{Th}$	$2.48 \times 10^5$	4.7 MeV	0.136 MeV	10%
$^{230}\text{Th}$ to $^{226}\text{Ra}$	$7.54 \times 10^4$	4.7 MeV	--	--

The specific activity of  $^{238}\text{U}$ , based on both a uranium density of  $9.7 \text{ g/cm}^3$  in a  $\text{UO}_2$  matrix and the half-life from Table 10, is  $7.2 \times 10^6 \alpha/\text{min cm}^3$ . Combined with the active volume, the minimum background emission rate is  $(32 \alpha + 3 \gamma) / \text{day}$ . Within the time-frame of experimentation, no contribution from spontaneous fission is expected. The rate of such an event, considering a spontaneous fission rate of  $3.93 / \text{min cm}^3$ , is once per 161 years within the small active volume.

The RC time-constant of the ORTEC 142PC charge-sensitive pre-amplifier was determined experimentally. The test jack circuit of the amplifier employs a 1 pF capacitor to provide charge injection to the amplifier circuit [70]. A linear fit of the amplifier response to a series of known amplitude pulses at the test jack provided the parasitic capacitance across the pre-amplifier circuit,  $C_f$ , which has an equivalent resistance of  $500 \text{ M}\Omega$ . The measured capacitance of 0.28 pF is consistent with the 0.1 to 2 pF operating range of the amplifier. The resulting time constant, the product of 0.28 pF and  $500 \text{ M}\Omega$ , is  $140 \mu\text{s}$ .

The maximum amplitude of a pulse for a given ionization energy,  $V/E$ , is related to the amount of charge collected within the detector by (74) in which  $q$  is the elementary charge,  $C_f$  is the amplifier capacitance, and  $E_e$  is the energy for electron-hole pair creation within the detector material [71].

$$\frac{V}{E} = \frac{q}{C_f E_e} \quad (74)$$

The range of  $E_e$  for  $\text{UO}_2$ , an unknown parameter, is estimated by assuming a lower limit of 2 eV, the estimated band-gap. An upper limit is estimated at 6 eV by scaling the band gap by three; a factor empirically observed in silicon which has a band gap of 1.12 eV and an electron-hole pair energy of 3.62 eV [72]. The resulting detector  $V/E$  range is 95 to 286 mV/MeV. The complete collection of a 4 MeV  $\alpha$ -particle from decay is expected to produce a pulse maximum ranging from 1.2 to 0.4 V.

### 6.2.3 Initial Results

A simple experiment was used to examine both the detector background and determine if the detector reacted to an external source. With an applied crystal bias of 6 V over a period of 24 hours, the detector response was observed in the form of persistent oscilloscope traces shown in Figure 40a using an amplitude trigger. The oscilloscope trigger was set above the noise level. This was followed by another 24 hr period in which a single  $^{241}\text{Am}$  button source was placed near the detector. Notable is that during the background acquisition (Figure 40a), there were only 7 counts over the 24-hour period. The signals that were observed had very long tails, much longer than the preamplifier decay time used in the detector. However, in the 24-hour source exposure experiment, 67 counts were observed (Figure 40b). While this rise in counts was accompanied by an increased background (once again composed of long tailed pulses), there were also many preamplifier pulses of the appropriate/expected shape which can be seen by visual comparison of Figure 40a and Figure 40b.

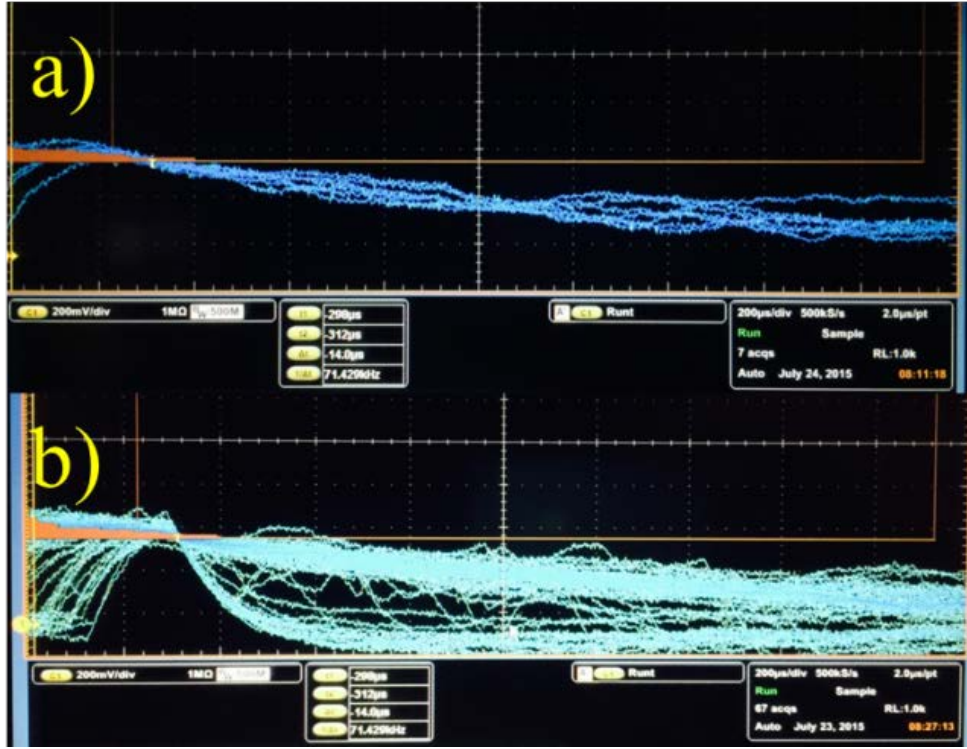


Figure 40. Results of the initial a) 24-hour background/internal noise measurement and b) 24-hour  $^{241}\text{Am}$  signal response are pictured. During the background acquisition, only 7 counts were obtained, whereas 67 counts were acquired during the source exposure time period.

The average pulse amplitude in each case was nearly identical,  $0.47 \pm 0.04$  V without the source and  $0.50 \pm 0.07$  V with the source. The incident  $\alpha$  radiation from the  $^{241}\text{Am}$  source, though initially emitted at 5.47 MeV, was estimated to have a mean energy of  $4.03 \pm 0.05$  MeV after scattering through the 5 mm air-gap to the crystal as determined by a 10k particle SRIM Monte-Carlo simulation [69]. The energy similarity between the incident and expected background signal was encouraging in that it explained why the signal amplitudes were similar. Additionally, 20% of the expected background events and under 3% of the background-subtracted  $^{241}\text{Am}$  events were observed. Both phenomenon were encouraging given the nature of the detector and estimate of the active

region despite the poor sampling statistics. The differences in the decay time of the pulses measured with and without the source also suggested that decay time might be a means to differentiate the signals.

Several new data sets were obtained to measure this phenomenon. After several days, the background noise level increased in amplitude by as much as a volt along with the observed pulse-heights with the same settings. No changes to the experimental apparatus were made. The rise in the signal was tentatively attributed to AC line noise and appeared to be more significant between the times of 1600 and 1900 each day. However, the installation of a sophisticated power conditioner to control this variable did not eliminate this phenomenon.

#### **6.2.4 Noise Analysis**

The  $I(V)$  measurement taken soon after contact placement indicated that  $21\ \mu\text{A}$  of leakage current was created by a 6 V bias, the operating condition of the detector. This total leakage current is a combination of bulk and surface currents. Disregarding contributions from the stable, commercially procured components of the detector, fluctuations in the leakage current of the crystal are the likely cause of detector noise.

According to [72], detector noise is attributed as follows:

- i) 'Shot noise': fluctuations in bulk generated leakage
- ii) Fluctuations in surface leakage
- iii) 'Johnson noise': a contribution from poor electrical contacts or series resistance.

Within the mechanical contact system, all three categories are effectively coupled. Bulk generated leakage current, the result of either semiconductor-metal junction dynamics or thermally generated carriers, can be strongly affected by changes to the contacts from vibration or relaxation. In fact, after establishing the contacts, the relaxation of the system was observed as intermittent noise signals for several minutes, presumably as the tension on opposing pins reached an equilibrium. Were  $\text{UO}_2$  to have piezoelectric qualities, this would provide an additional contribution under the pressure of the pins. However, there is no data to suggest this. Surface leakage can also be affected by the contacts which are established at the surface interface.

Temperature induced shot noise is not expected to significantly contribute to the noise signal. The thermal energy contribution is on the order of 0.025 eV at 70 °F (294 K), the nominal temperature of the laboratory. Fluctuations on this order of magnitude are not significant.

It is a possibility that fluctuating surface leakage is a significant contributor to detector noise as it was observed experimentally that, in at least one experiment, increased noise correlated with a period of high relative humidity. The transient and fluctuating nature of the noise suggests a reversible process unlike enhanced surface oxidation. Conductivity data as a function of humidity for a nearly stoichiometric  $\text{UO}_2$  single crystal are not available. However, an analogous quartz system indicates enhanced surface conductivity varying by two orders of magnitude in the range of 20% and 90% relative humidity [73]. If the  $\text{UO}_2$  surface behaves in a similar manner, an increased surface leakage current would be expected with increased relative humidity.

From a practical stand-point, the noisy signal provided a challenge to data collection. A simple amplitude trigger was no longer sufficient for practical data collection.

### 6.2.5 Pulse Form Analysis

A typical pulse form with a continuous leakage background is depicted in Figure 41. The decaying tail of the pulse can be mathematically described by (75) where  $V$  is the pulse-height in volts,  $t$  is time,  $V_0$  is the maximum pulse height, and  $\tau$  is the decay time constant. The pulse decays in time at a rate described by the decay time constant. The pulse form is provided by the amplifier which provides the nominal time constant but variations in the collection of a pulse are reflected in actual value of  $\tau$ .

$$V(t) = V_0 e^{-t/\tau} \quad (75)$$

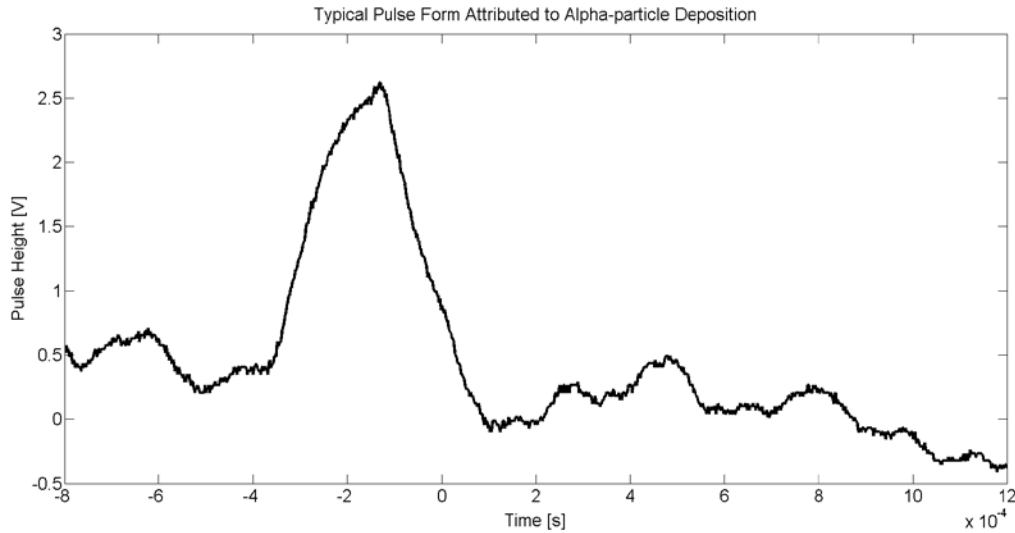


Figure 41. A typical pulse-shape attributed to an alpha-particle deposition in the detector. The zero-time point in this plot is determined by the trigger setting of the oscilloscope which is arbitrary.

In order to both identify and compare pulses in a data set focused on the pulse tail, the data is reduced to a set of parameters. From a practical perspective, a direct fitting of the data points comprising the tail yields  $V_0$  and  $\tau$ . However, the pulse form presents a variable baseline which creates uncertainty in  $V_0$  since the pulse forms are superimposed on a continuous leakage-induced background. Fitting the data in derivative space eliminates the pulse-height variation from the baseline and provides a means to fit the data using (77) where the zero-time reference coincides with  $V_0$ . The derivative fit produces the best measurement of  $V_0$  while the direct fit, informed by the derivative fit, produces the best estimate of  $\tau$ .

$$\frac{dV}{dt} = -\frac{V_0}{\tau} e^{t/\tau} \quad (76)$$

$$\frac{dV}{dt(0)} = -\frac{V_0}{\tau} \quad (77)$$

### 6.2.5 Detector Noise & Trigger Scheme

During periods of increased noise, potentially the result of uncontrolled parameters, the baseline of the signal increased by as much as a volt. When this occurred, data collection with a simple amplitude trigger was affected. The increased baseline noise constantly triggered the oscilloscope. In order to reduce non-pulse data collection, a fall-time trigger employing two amplitude thresholds and a delay time was developed. The trigger required that the signal first drop through an upper threshold and, within a specified minimum time, across the lower threshold; consistent with the behavior of well-defined pulse decay. The nominal pre-amplifier time constant was used



as the delay time with a minor reduction in order to establish an appropriate minimum decay time limit.

Despite the trigger scheme, noisy oscilloscope traces were recorded along with well-defined pulse forms. An automated means of pulse-identification and parameter measurement was developed to identify data for further analysis. Figure 42 depicts some oscilloscope traces captured by the trigger scheme and illustrates the challenge of automating pulse identification from the data. The algorithm for identification of a pulse required the following:

- 1) A pulse maximum within a 0.6 ms window about the trigger point of the 2 ms scope trace.
- 2) A decay tail extending at least one decay constant in time without interruption.
- 3) A time constant less than 0.005 s.
- 4) A coefficient of determination,  $R^2$ , of at least 0.90 required of the fitting of the pulse tail.

Data not fitting these criteria, though potentially a pulse superimposed with noise, was not analyzed. The use of a MATLAB code to process the data files enabled the practical evaluation of large data sets. Each recorded oscilloscope trace was collected as a  $2 \times 1000$  vector of voltage and time values. Based on the memory limitation of the oscilloscope, up to 32,767 triggered-events were recorded for each data set.

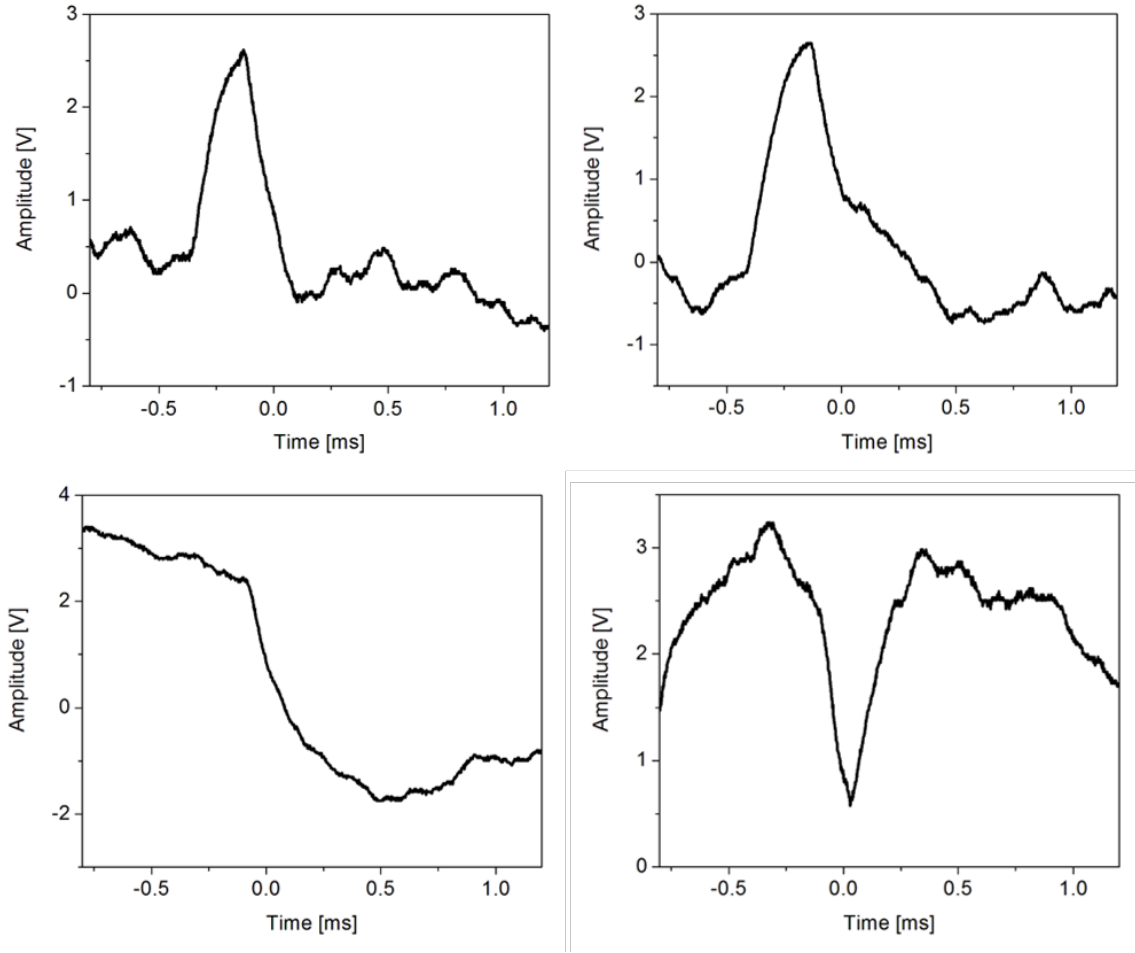


Figure 42. Oscilloscope traces typical of events captured by the fall-time trigger. The upper left trace is considered a pulse. The upper right is pulse-like but excluded by the algorithm due to in insufficiently long tail and poor exponential fit. The bottom left trace is excluded by the absence of a defined pulse peak. The bottom right trace is excluded based on a lack of defined pulse peak and poor exponential tail fitting.

### 6.2.6 Source Description and Geometry

The response to several radiation sources was studied as well as the effect of differing fluxes. Up to four  $^{241}\text{Am}$  sources were placed approximately 5 mm from the crystal both with, and without, a paper shield as shown in the uppermost portion of

Figure 43 and the left side of Figure 44. A closer approach was impractical given the size of the sources and the crystal holder.

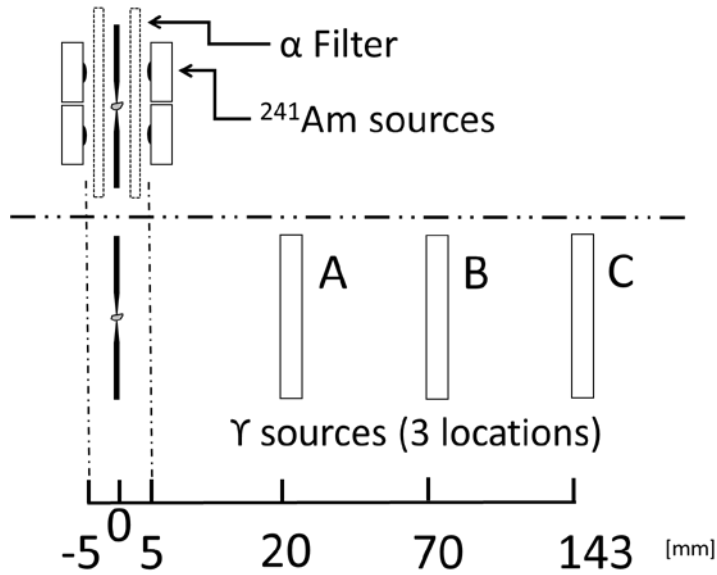


Figure 43. The experimental source and detector geometry.

The use of a paper shield in conjunction with the  $^{241}\text{Am}$  provided a convenient source of either 60 keV  $\gamma$ -rays or a flux of both the  $\gamma$ -rays and  $\alpha$ -particles. Additional  $\gamma$ -ray sources,  $^{55}\text{Fe}$ ,  $^{60}\text{Co}$ , and  $^{137}\text{Cs}$  were set at three different distances from the detector within the Faraday cage as shown on the lower portion of Figure 43. A summary of the source information is presented as Table 11. All  $\beta$  emissions were shielded with plastic.

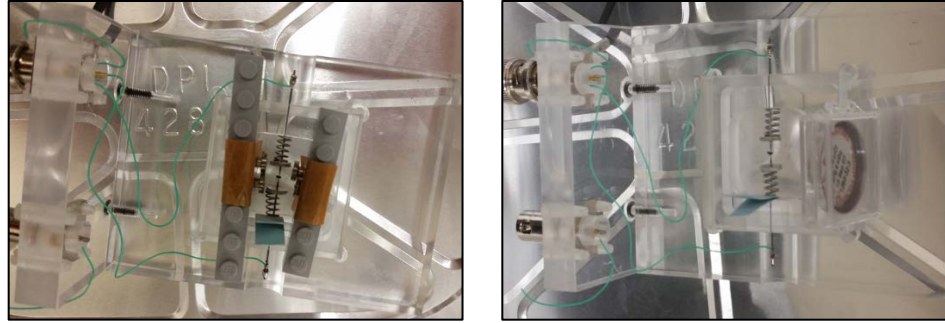


Figure 44. Placement of the  $^{241}\text{Am}$  sources (left) and a  $\gamma$ -ray source (right).

Table 11. Summary of sources. The  $^{241}\text{Am}$  source was used with and without shielding for  $\alpha$  particles.

Source	Activity	Emission	Working Distance
$^{241}\text{Am}$	4 x 36.8 kBq	$\alpha$ , 5.4 MeV; 4 MeV at 5 mm $\gamma$ -ray, 0.060 MeV  $\alpha$ , 5.4 MeV (Shielded) $\gamma$ -ray, 0.060 MeV	5 mm
$^{60}\text{Co}$	134 kBq	$\gamma$ -ray, 1.17 MeV $\gamma$ -ray, 1.33 MeV $\beta$ , 0.31 MeV (Shielded) $\beta$ , 1.48 MeV (Shielded)	20, 70, & 143 mm
$^{55}\text{Fe}$	1680 kBq	$\gamma$ -ray, Mn $K\alpha$ , 0.006 MeV Auger, 0.005 MeV (Shielded)	20, 70, & 143 mm
$^{137}\text{Cs}$	262 kBq	$\gamma$ -ray, 0.662 MeV $\beta$ , 0.512 MeV (Shielded) $\beta$ , 1.174 MeV (Shielded)	20, 70, & 143 mm

### 6.2.7 Efficiency Analysis

The collected data is summarized in Table 13 which shows the number of triggered events, the number of events identified as pulses, and the average trigger and

pulse detection rates. The two background measurements were conducted 7 days apart with different trigger thresholds but in accordance with a delay time of 140  $\mu$ s. The trigger settings for all data acquired using a source were the same. Though not conclusive, this may be the reason why the pulse detection rate for several sources is lower than that of the background. Most of the  $\gamma$ -ray data was acquired at nearly the maximum oscilloscope collection rate (italicized in red) of ~3 events per sec, or 10,800 events per hour. Even at the lowest flux, most of the events were not pulses as indicated by the low acceptance value (ratio of triggered events to code-identified pulses). Although the background noise level increased, the presence of the  $\gamma$  sources appeared to increase the noise as well.

One of the expected attributes of a detector is the reduction of the count rate with reduced flux. The detection rate of a given energy at 70 mm should be four times that at 143 mm, nearly twice the distance. Although this holds in the case of  $^{60}\text{Co}$  in which the count rate was not saturated at 143 mm, it is not replicated by the other  $\gamma$ -ray source data. In the case of  $^{60}\text{Co}$ , a combination of low activity and small cross-section likely prevented saturation though the detection rate was higher than expected. Summarized in Table 12, the  $\gamma$ -ray emissions from  $^{55}\text{Fe}$  and  $^{241}\text{Am}$  are more likely to interact with the crystal than those of  $^{137}\text{Cs}$  and  $^{60}\text{Co}$ . In fact, the crystal should be nearly transparent to  $^{60}\text{Co}$ .

Table 12. Mono-energetic photon attenuation in the UO<sub>2</sub> crystal.

	x-ray Energy [MeV]	Attenuation / mm UO <sub>2</sub>
Fe-55	0.006	100.0%
Am-241	0.060	99.5%
Cs-137	0.662	5.1%
Co-60	1.170	1.4%
	1.330	1.3%

The saturated data is not useable for efficiency computation. Considering the inability to appropriately remove background counts, none of the data is particularly well-suited for such a computation.

The detector volume was based on key assumptions which must be considered for a computation of geometric efficiency. Three estimates of the detector volume within the 1 mm diameter crystal are presented in Table 13 along with the corresponding detection efficiency. The 0.009 mm (9  $\mu$ m) radius is based on the attenuation length of a 4 MeV  $\alpha$  particle. The value of 0.1 mm is approximately 10 times larger and provides a comparative value. A radius of 0.5 mm represents the entire crystal, the maximum possible value. The estimate of geometric efficiency, based on detection of  $\alpha$ -particles, neglecting the background contribution, and bounded by the three active detector sizes, is between 0.01% and 27%. When based only on the 0.06 MeV  $\gamma$ -rays from the shielded <sup>241</sup>Am, geometric efficiency is between 0.003% and 9%. Estimates based on higher energy  $\gamma$ -rays appear nonsensical especially given the low probability of interaction.

Table 13. Summary of the data collected using different sources and source to detector distances. Numbers in *red* indicate the data was collected very near the maximum collection rate of the oscilloscope and is potentially inaccurate.

Source	Events	Code-Identified Pulses	Avg. Event Rate [/h]	Avg. Pulse Detection Rate [/h]	Acceptance	Source Activity [KBq]	Sensitivity to Estimated Detector Radius		
none	16435	6065	1048	387	37%	--	0.009 mm	0.1 mm	0.5 mm
none	32181	9269	1229	354	29%	--	Det. Ratio [%]	Det. Ratio [%]	Det. Ratio [%]
<sup>241</sup> Am, 5mm	32070	19566	339	207	61%	294	27	0.22	0.01
<sup>241</sup> Am/Paper	4605	2540	62	34	55%	147	9	0.07	0.003
<sup>60</sup> Co, 143 mm	32757	6825	723	151	21%	134	31706	257	10
<sup>60</sup> Co, 70 mm	32767	2063	9443	595	6%	134	30294	24581	10
<sup>60</sup> Co, 20 mm	32767	1456	9127	406	4%	134	1974	1598	1
<sup>137</sup> Cs, 143 mm	32767	2830	8738	755	9%	262	80982	656	26
<sup>137</sup> Cs, 20 mm	32767	1983	8928	540	6%	262	1341	1086	0.43
<sup>55</sup> Fe, 143 mm	32767	1886	7380	425	6%	1680	7116	58	2
<sup>55</sup> Fe, 70 mm	32767	1553	9052	429	5%	1680	1741	1412	1
<sup>55</sup> Fe, 20 mm	32767	999	9498	290	3%	1680	112	91	0.04
<sup>55</sup> Fe, 20 mm	32767	1444	8338	367	4%	1680	142	115	0.05

### 6.2.8 Pulse-Shape Parameter Study

With detection rate analysis inconclusive, a pulse-shape parameter study was used to examine the differences, if any, between the measured pulse-forms. Using the fitting data from the pulse identification algorithm, a  $100 \times 100$  bin, three-dimensional histogram was created for each data set using the fitted pulse-height and time constant as the ordinate and abscissa with the number of binned pulses providing an intensity as shown by the 'heat plot' format of Figure 45. The plots are scaled to show the most intense regions of change within the dataset, and initial analysis suggests that the rate of pulse decay differs among the radiation types. Pulses attributed to the  $^{241}\text{Am}$   $\alpha$  particles decay more rapidly than those of the background. This phenomenon was tacitly observed in the initial 24-hour study. Pulses attributed to the  $\gamma$  ray emissions from  $^{241}\text{Am}$  and  $^{60}\text{Co}$  (placed at 143 mm) are characterized by intermediate decay constant values.  $^{60}\text{Co}$  at 143 mm was the only non-Am source that measured below the maximum detection rate.

The pulse amplitudes, however, are higher than expected. The estimate of  $V/E$  placed a 4 MeV  $\alpha$  particle pulse at just over 1 V which is at odds with the measured 2 V pulse cluster for  $^{241}\text{Am}$  depicted in Figure 45. It is, however, gratifying that the pulse height of the externally supplied  $\alpha$  particle is lower than that of the background as one might expect from a detector dead-layer. The response to the 0.06 MeV  $\gamma$ -rays from  $^{241}\text{Am}$ , even at full energy deposition, are predicted to produce only a 0.02 V pulse and yet 2.5 V is measured; a non-physical response. The histograms for  $^{137}\text{Cs}$ , those remaining for  $^{60}\text{Co}$ , and those of  $^{55}\text{Fe}$  show significant scatter and lack of defined clustering as shown in Figure 46 and Figure 47. The pulse-amplitudes are larger than



those of the background cluster and are potentially attributed to detector noise given the decay constant similarity to  $140\text{ }\mu\text{s}$ , the expected data bias from the oscilloscope trigger.

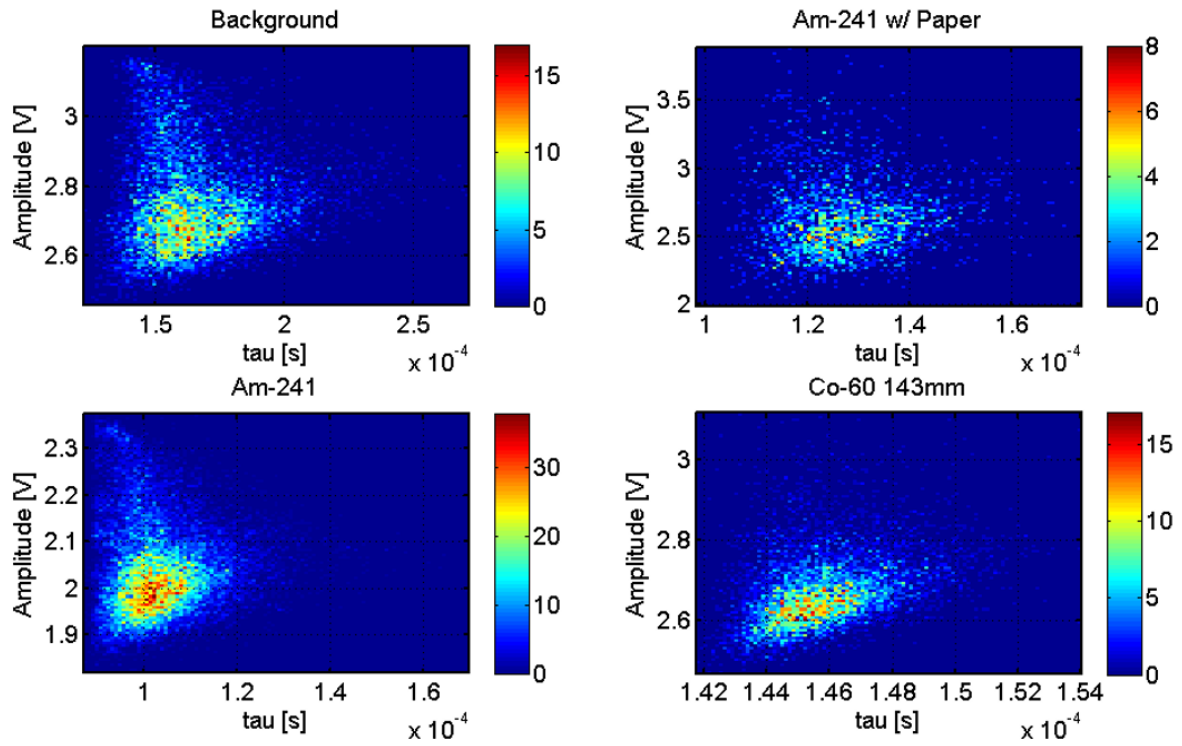


Figure 45. A pulse height vs. time constant histogram summarizing the post-processed detector background, response to  $^{241}\text{Am}$ ,  $^{241}\text{Am}$  with paper filter, and  $^{60}\text{Co}$  at 143 mm. The red pixels are of the highest intensity for each histogram with a value indicated by the color bar.

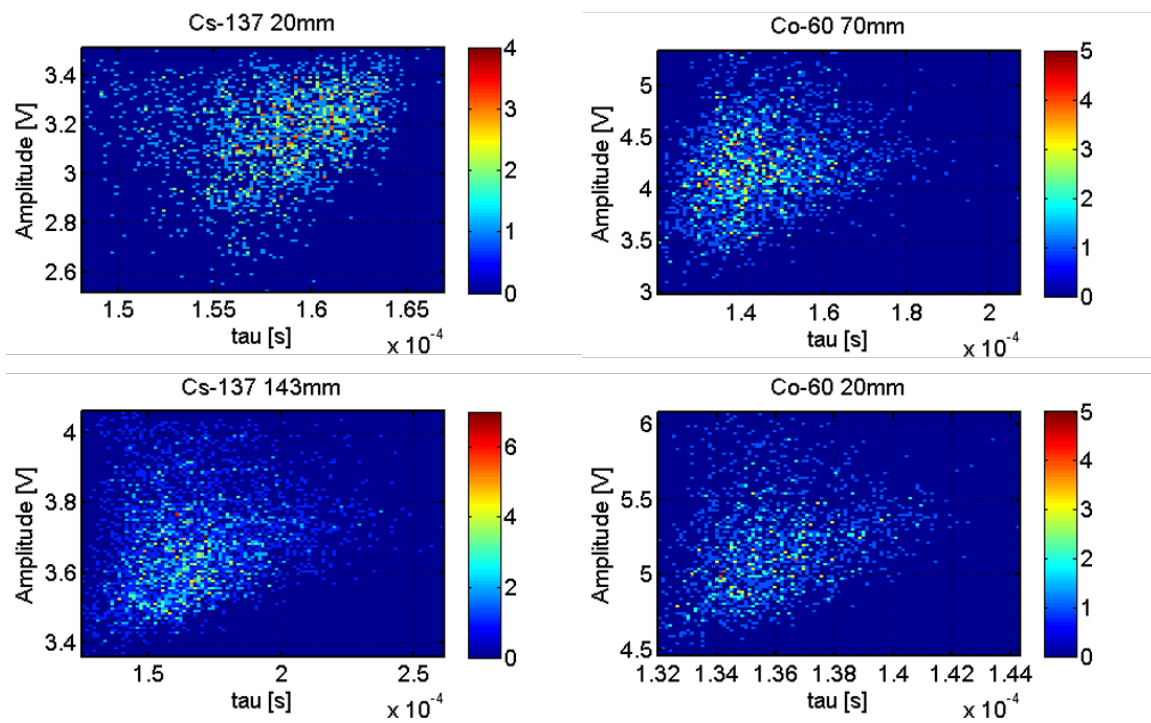


Figure 46. A pulse height vs. time constant histogram summarizing the post-processed detector background, response to  $^{137}\text{Cs}$  at two different distances as well as  $^{60}\text{Co}$ . The red pixels are of the highest intensity for each histogram with a value indicated by the color bar.

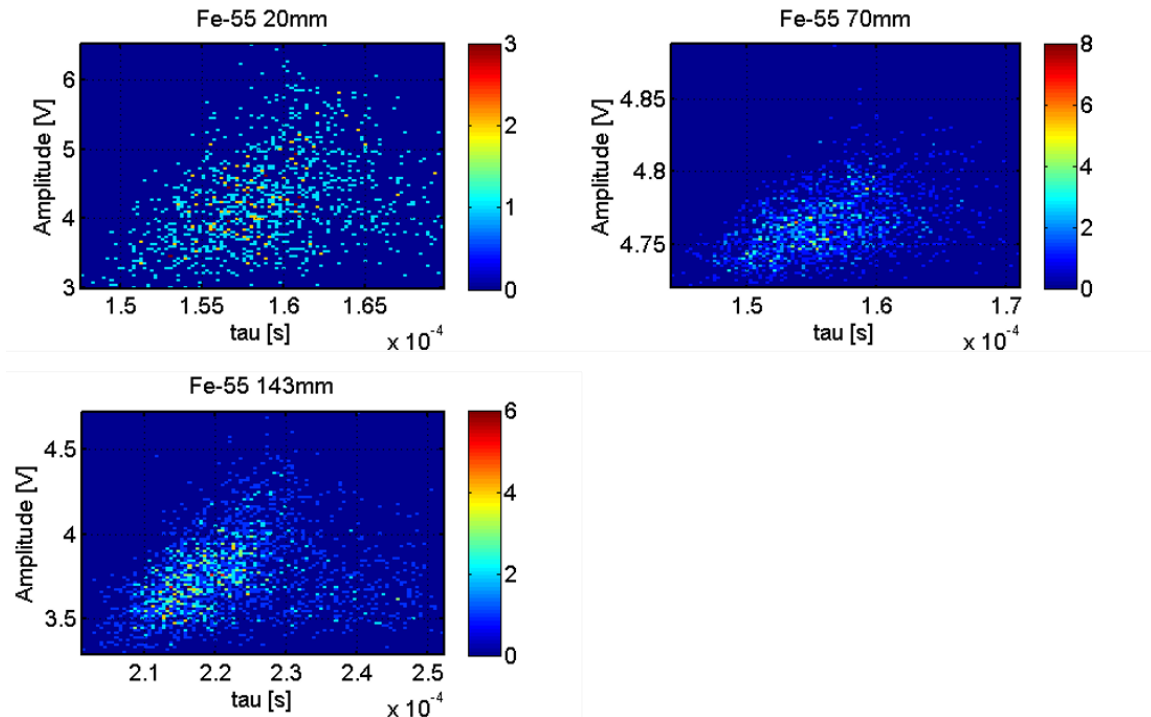


Figure 47. A pulse height vs. time constant histogram summarizing the post-processed detector background, response to  $^{55}\text{Fe}$  at three different distances. The red pixels are of the highest intensity for each histogram with a value indicated by the color bar.

The heat-map clusters can be misleading. They do portray regions of high relative intensity but they do not necessarily show a significant count population. For example, the strong  $^{241}\text{Am}$  cluster contains roughly 545 of the 9269 measured pulses, or approximately 6% of the dataset. An expansion of the histograms to encompass regions containing 63%, a convenient value, of the measured pulse set produced much larger parameter spaces which show significant overlap between the different radiation responses as depicted in Figure 48.

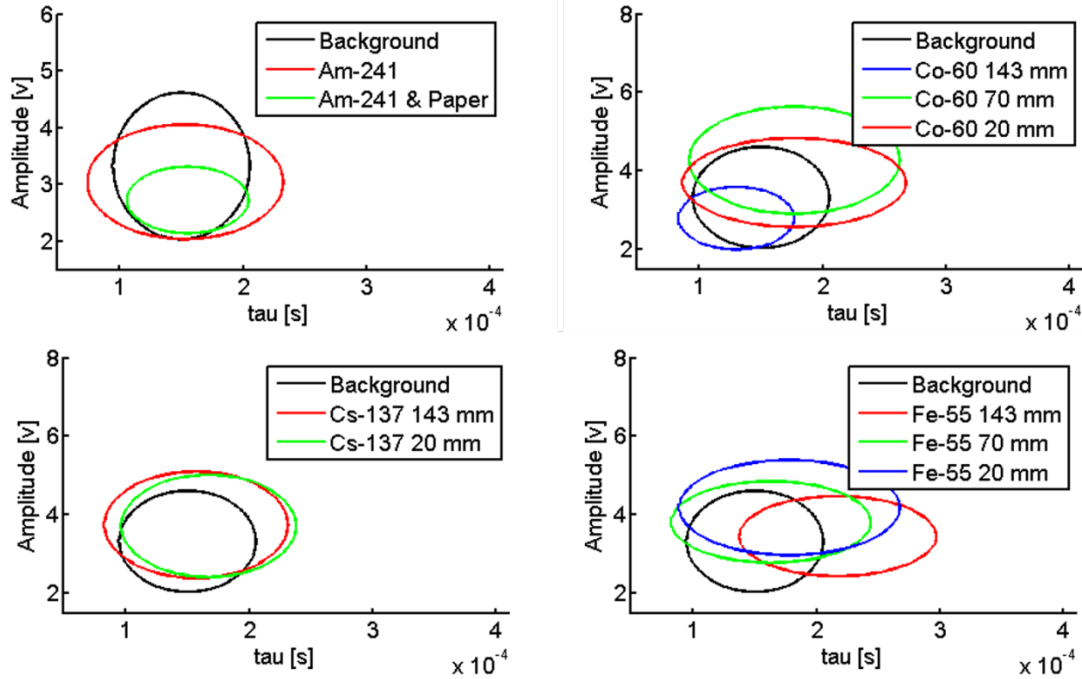


Figure 48. Results of the parameter study using 63% of the identified pulses. The scheme cannot separate the radiation types at this level.

### 6.3 Implications

The ability of the crystal to detect radiation, at least in the configuration of this experiment, is inconclusive. The unstable detector signal is the primary detractor of the study and the most likely reason that the count-rate experiment was inconclusive. The parameter study, at least for  $\alpha$  particles, does show promise given the strong parameter clustering and faster pulse decay specifically attributed to the  $^{241}\text{Am}$   $\alpha$  particles. The expanded parameter space results summarized in Figure 48 can be explained in two ways; either the algorithm identified non-pulse noise in addition to real pulses, or the data is tantalizing, irrelevant, and the detector does not work. Both can be argued, but, it is possible that the detector was in fact responding to  $\alpha$  radiation. Based on a similar origin,

it is certainly possible that the background signal and the external  $^{241}\text{Am}$  response would be similar. The  $\gamma$ -ray data cannot be easily reconciled, but the increased noise levels in the presence of a  $\gamma$ -ray flux do not bode well for this material as a neutron detector.

The detector appeared to degrade over time with an increased noise contribution in the days following contact placement. Subsequent detector studies would benefit from surface sensitivity experiments focused on surface conductivity as well as time-dependent  $I(V)$  and  $C(V)$  measurements to assess detector stability.

## VII. Conclusion

### 7.1 Summary of Findings

The systematic study of hydrothermally grown uranium dioxide crystals was undertaken to specifically address the following questions:

- (1) Does the hydrothermal growth process produce high-quality, high-purity, stoichiometric, single-crystal, uranium dioxide?
- (2) What are the electronic characteristics of the crystal and crystal surface?
- (3) Do the crystals have the potential for radiation detection?

To a great extent, all questions have been answered and the outlook is promising for the use of this material in solid state radiation detectors.

#### 7.1.1 Crystal Quality

Hydrothermally grown  $\text{UO}_2$  crystals have been confirmed to be single-crystal, nearly stoichiometric in the fluorite structure, and high purity. XRD measurements show long-range order and a nominal lattice parameter of  $5.4703 \pm 0.0006 \text{ \AA}$  which is in excellent agreement with measurements on  $\text{UO}_{2.000 \pm 0.001}$  by [32] yielding  $5.47127 \pm 0.00008 \text{ \AA}$  at  $20^\circ\text{C}$ . This provides a nominal stoichiometry for hydrothermally synthesized crystals of  $\text{UO}_{2.003}$ . XRF and XPS measurements of the most recent samples show relatively high purity,  $> 96\%$   $\text{UO}_2$ , containing few (10 or less) impurity species. The growth process has been refined to remove low-Z contaminant species but high-Z impurities ( $Z > 55$ ) remain of concern as the solubility of such species appears similar to that of  $\text{UO}_2$ . It remains to be seen if these impurities extend to the crystal bulk. Depth

resolved XPS measurements indicate that the stoichiometry of the  $\text{UO}_2$  surface remains nearly constant between the surface and sub-surface with little indication of hyperstoichiometry. In addition, temperature dependent XPS measurements indicate that the nearly-stoichiometric crystal surface consists of a mixed phase of  $(\text{UO}_{2+x} + \text{U}_4\text{O}_{9-y})$  which likely becomes a single  $(\text{UO}_{2+x})$  phase at a transition temperature between 475 and 495 K. Impurity mobility appears to increase sharply with the onset of the single phase which may be leveraged for crystal purification, or may identify an operating limitation for doped crystals.

### **7.1.2 Electronic Characteristics**

The XPS spectral features of both the U and O core lines are consistent with  $\text{UO}_2$  which is corroborated by the Auger parameter analysis. Both the (100) and (111) surfaces are electronically stable with work functions deviating less than 5% between measurements of the freshly sputtered and reconstructed surfaces under vacuum conditions. The photoelectric work functions of the  $\text{UO}_2$  (100) and  $\text{UO}_2$  (111) surfaces were measured to be 5.80 eV and 6.28 eV respectively with an uncertainty of  $\pm 0.36$  eV. An experimental  $I(V)$  measurement of a fabricated Ag/ $\text{UO}_2$ /GaIn device identified the semiconductor as n-type and indicated good agreement with the expected Ohmic nature of the contact.  $C(V)$  measurement analysis provided an estimate of the Schottky barrier height larger than expected from theory.

### 7.1.3 Potential for Radiation Detection

A simple resistive  $\text{UO}_2$  detector was fabricated by application of mechanical tungsten contacts. Despite multiple efforts to parse the measured response, the device did not conclusively demonstrate the ability to detect or discriminate between  $\alpha$  and  $\gamma$  radiation. However, the data did show encouraging pulse-shape discrimination results as well as the background signal expected of a depleted  $\text{UO}_2$  device. A number of engineering challenges were identified to successful detector implementation to include detector noise reduction from uncontrolled parameters. The potential for radiation detection using hydrothermally synthesized  $\text{UO}_2$  remains to be answered.

## 7.2 Future Work

Much of the analysis of the hydrothermally grown crystals to date has been surface-oriented. Although XRF measurements have provided an overall composition analysis, both the extent of the hyperstoichiometric surface layer, the location of the cesium impurity and the core composition of the crystal have yet to be fully explored. To this end, a depth-resolved elemental composition measurement, such as time-of-flight secondary ion mass spectroscopy (TOF-SIMS), would provide a more complete picture of the crystal below the surface.

The experimental investigation of electrical contact metal-semiconductor junctions is a rich topic for future work. This research would also benefit from measurements by atomic force microscopy to determine the relative bonding strength of each metal to the crystal surfaces in the pursuit of a robust device. In addition, the



majority charge carrier of the crystals has not been identified. Hall effect measurements may clarify the nature of the majority charge carrier.

The pulse detection experiment identified several avenues of continued research. The most notable challenge was noise reduction which may be improved with better device construction techniques. The electrical behavior of the crystal surface to atmospheric influence is also an area of interest. And finally, the development of new strategies and algorithms for signal processing may benefit experimental work but real-time techniques are needed to implement an effective detector in the future.

## Works Cited

- [1] USNRC, "U.S. Nuclear Regulatory Commission, definition of Special Nuclear Material," USG, [Online]. Available: <http://www.nrc.gov/materials/sp-nucmaterials.html>. [Accessed 2016].
- [2] Bridgman, Introduction to the Physics of Nuclear Weapon Effects, Ft Belvoir, VA: Defense Threat Reduction Agency, 2001.
- [3] G. Knoll, Radiation Detection and Measurement, 3d ed., USA: John-Wiley and Sons, 2000.
- [4] D. Shea and D. Morgan, "The Helium-3 Shortage: Supply, Demand, and Options for Congress," Congressional Research Service, Washington, D.C., 2010.
- [5] J. Walker, Z. Bell and W. Allen, "A miniaturized neutron detector and counting system," *Nuclear Science Symposium Conference Record. IEEE*, vol. 2, pp. 1036-1039, 1998.
- [6] T. Meek and B. von Roedern, "Semiconductor devices fabricated from actinide oxides.," *Vacuum*, vol. 83, pp. 226-228, 2009.
- [7] B. von Roedern, T. Meek and M. Haire, "Some Electrical Properties of Ion-Implanted Urania - Part II," in *Symposium of the Society for the Advancement of Material and Process Engineering (SAMPE)*, Long Beach, 2003.
- [8] C. Kruschwitz, S. Mukhopadhyay, D. Schwellenbach, T. Meek and B. Shaver, "Semiconductor neutron detectors using depleted uranium oxide," in *Proc. SPIE 9213; Hard X-Ray, Gamma-Ray, and Neutron Detector Physics XVI*, San Diego, 2014.
- [9] Y. Leng, Materials Characterization, Introduction to Microscopic and Spectroscopic Methods, 2d ed., Weinheim: Wiley, 2013.
- [10] F. Goulding and J. Jaklevic, "XRF Analysis - Some Sensitivity Comparisons Between Charged-Particle and Photon Excitation," Lawrence-Berkeley National Labs, Berkeley, unk.

- [11] S. Hufner, Photoelectron Spectroscopy, 3d Ed., Heidelberg: Springer, 2003.
- [12] S. Hofmann, Auger and x-ray Photoelectron Spectroscopy in Materials Science, Heidelberg: Springer, 2013.
- [13] S. Tanuma, C. Powell and D. Penn, "Inelastic Mean Free Paths of Low Energy Electrons in Solids," *Acta Physica Polonica A*, vol. 81, no. 2, pp. 169-186, 1992.
- [14] M. Helander, M. Greiner, Z. Wang and Z. Lu, "Pitfalls in measuring work function using photoelectron spectroscopy," *Applied Surface Science*, vol. 256, pp. 2602-2605, 2010.
- [15] S. Sze, Physics of Semiconductor Devices, Hoboken, NJ: John Wiley & Sons, 2007.
- [16] K. Wandelt, "The local work function: Concept and implications," *Applied Surface Science*, vol. 111, pp. 1-10, 1997.
- [17] S. Hufner, Photoelectron Spectroscopy, Berlin: Springer, 2003.
- [18] D. Schroder, Semiconductor Material and Device Characterization, New York: John Wiley & Sons, 1998.
- [19] C. Kittel, Introduction to Solid State Physics, 4th ed., New York: John Wiley & Sons, 1971.
- [20] P. McKelvey, Solid State Physics for Engineering and Material Science, Kreiger Publishing Co., 1993.
- [21] N. Wu, D. Wisbey, T. Komesu, Z. X. Yu and M. Manno, "The kinetic energy dependent effective Debeye temperature for CoS<sub>2</sub>(100)," *Physics Letters A*, vol. 374, no. 14, pp. 2484-2489, 31 March 2008.
- [22] D. Briggs and J. Grant, Surface Analysis by Auger and X-ray Photoelectron Spectroscopy, Trowbridge, UK: The Cromwell Press, 2003.
- [23] LBNL, "X-Ray Data Booklet, 2d ed.," Lawrence Berkeley National Labs, US Department of Energy, Berkeley, 2001.

- [24] NIST, "X-ray Photoelectron Spectroscopy Database 20, V 4.1," 15 September 2012. [Online]. Available: <http://srdata.nist.gov/xps/Default.aspx>. [Accessed 22 July 2016].
- [25] S. M. Sze and K. K. Ng, *Physics of Semiconductor Devices*, 3d ed., Hoboken: John Wiley & Sons, 2007.
- [26] S. Sze, *Semiconductor Devices*, 2d ed., Hoboken: John Wiley and Sons, 2002.
- [27] K. Byrappa and M. Yoshimura, *Handbook of Hydrothermal Technology*, Park Ridge, NJ: Noyes Publications, 2001.
- [28] M. Mann, D. Thompson, K. Serivalsatit, T. Tritt, J. Ballato and J. Kolis, "Hydrothermal Growth and Thermal Property Characterization of ThO<sub>2</sub> Single Crystals," *Crystal Growth and Design*, vol. 10, pp. 2146-2151, 2010.
- [29] K. Momma and F. Izumi, "VESTA 3 for three-dimensional visualization of crystal, volumetric and morphology data," *J. Appl. Crystallogr.*, vol. 44, pp. 1272-1276, 2011.
- [30] T. d. Freitas, "Uranium dioxide sintering kinetics and mechanisms under controlled oxygen potentials," University of Illinois, Doctoral thesis, Champaign, IL, 1977.
- [31] J. Stubbs, A. Chaka, E. Ilton, C. Biwer, M. Engelhard, J. Bargar and P. Eng, "UO<sub>2</sub> Oxidative Corrosion by Nonclassical Diffusion," *Phys. Rev. Lett.*, vol. 114, pp. 246103-1,5, 2015.
- [32] G. Leinders, T. Cardinels, K. Binnemans and M. Verwerft, "Accurate lattice parameter measurements of stoichiometric uranium dioxide," *Journal of Nuclear Materials*, vol. 459, pp. 135-142, 2015.
- [33] L. Lynds, W. Young, J. Mohl and G. Libowitz, "X-ray and Density Study of Nonstoichiometry in Uranium Oxides," in *Nonstoichiometric Compounds*, American Chemical Society, 1963, pp. 58-65.
- [34] S. Senanayake and H. Idriss, "UO<sub>2</sub>(111) Single Crystal: Comparison of Stoichiometric and Defective Surfaces by XPS," *Surface Science Spectra*, vol. 13, pp. 72-80, 2006.

- [35] R. Schueneman, A. Khaskelis, D. Eastwood, W. van Ooil and L. Burggraf, "Uranium oxide weathering: spectroscopy and kinetics," *J. Nucl. Materials*, vol. 323, pp. 8-17, 2003.
- [36] K. Holliday, W. Siekhaus and A. Nelson, "Measurement of the Auger Parameter and Wagner Plot for Uranium Compunds," *J. Vac. Sci. Technol. A.*, vol. 31, no. 3, p. 031401, 2013.
- [37] S. Hofmann, *Auger and x-ray Photoelectron Spectroscopy in Materials Science*, Heidelberg: Springer, 2013.
- [38] Y. Teterin and A. Y. Teterin, "The structure of X-ray photoelectron spectra of light actinide compounds," *Russian Chemical Reviews*, vol. 73, no. 6, pp. 541-580, 2004.
- [39] S. Van den Berghe, F. Miserque, T. Gouder, B. Gaudreau and M. Verwerft, "X-ray photoelectron spectroscopy on uranium oxides: a comparison between bulk and this layers," *Journal of Nuclear Materials*, vol. 294, pp. 168-174, 2001.
- [40] IAEA, "Thermodynamic and Transport Properties of Uranium Dioxide and Related Phases, Report No39," IAEA, Vienna, 1965.
- [41] S. Tougaard, "QUASES-IMFP-TPP2M Ver.3," [www.quases.com](http://www.quases.com), 2016.
- [42] P. Ruello, L. Desgranges, G. Baldinozzi, G. Calvarin, T. Hansen, G. Petot-Ervas and G. Petot, "Heat capacity anomaly in  $\text{UO}_2$  in the vicinity of 1300K: an improved description based on high resolution x-ray and neutron powder diffraction studies," *Journal of Physics and Chemistry of Solids*, vol. 66, pp. 823-851, 2005.
- [43] R. Krishnan, R. Srinivasan and S. Devanarayanan, *Thermal Expansion of Crystals*, New Delhi: Thomson Press, 1979.
- [44] B. Willis, "Neutron diffraction studies of the actinide oxides II. Thermal motions of the atoms in uranium dioxide and thorium dioxide between room temperature and 1100 C," *Proceedings of the Royal Society of London*, vol. A274, pp. 134-144, 1963.

- [45] F. Skomurski, R. Ewing, A. Rohl, J. Gale and U. Becker, "Quantum mechanical vs. Empirical potential modeling of uranium dioxide (UO<sub>2</sub>) surfaces: (111), (110), and (100)," *American Mineralogist*, vol. 91, pp. 1761-1772, 2006.
- [46] P. Tasker, "The structure and properties of fluorite crystal surfaces," *Journal de Physique Colloques*, vol. 41, no. C6, pp. 488-491, 1980.
- [47] T. Instruments, *LM555 Timer IC Specification Sheet, SNAS548D*, Texas Instruments, 2015.
- [48] W. McLean and H. Chen, "The thermionic emission and work function of U and UO<sub>2</sub>," *Journal of Applied Physics*, vol. 58, no. 12, pp. 4679-4684, 1985.
- [49] S. Senanayake and H. Idriss, "UO<sub>2</sub>(111) Single Crystal: Comparison of Stoichiometric and Defective Surfaces by XPS," *Surface Science Spectra*, vol. 13, pp. 72-79, 2007.
- [50] S. D. Senanayake, G. Waterhouse, A. Chan, T. Madey, D. Mullins and H. Idriss, "Probing Surface Oxidation of Reduced Uranium Dioxide Thin Film Using Synchrotron Radiation," *J. Phys. Chem. C*, vol. 111, pp. 7963-7970, 2007.
- [51] A. Y. Kuksin and D. Smirnova, "Calculation of Diffusion Coefficients of Defects and Ions in UO<sub>2</sub>," *Physics of the Solid State*, vol. 56, no. 6, pp. 1214-1223, 2013.
- [52] P. Tasker, "The Surface Properties of Uranium Dioxide," *Surface Science*, vol. 78, pp. 315-324, 1979.
- [53] F. Skomurski, R. Ewing, A. Rohl, J. Gale and U. Becker, "Quantum mechanical vs. empirical potential modeling of uranium dioxide (UO<sub>2</sub>) surfaces: (111), (110), and (100)," *American Mineralogist*, vol. 91, no. 11-12, pp. 1761-1772, 2006.
- [54] H. Heming, D. Andersson, D. Allred and K. Rector, "Determination of the Insulation Gap of Uranium Oxides by Spectroscopic Ellipsometry and Density Functional Theory," *J. Phys. Chem. C*, vol. 117, pp. 16540-16551, 2013.
- [55] G. Leinders, J. Pakarinen, R. Delville, T. Cardinaels, K. Binnemans and M. Verwerft, "Low-Temperature Oxidation of Fine UO<sub>2</sub> Powders: A Process of Nanosized Domain Development," *Inorg. Chem.*, vol. 55, pp. 3915-3927, 2016.

- [56] J. Heras and L. Viscido, "Work function changes upon water contamination of metal surfaces," *Appl. Surf. Sci.*, vol. 4, pp. 238-241, 1980.
- [57] P. Maldonado, L. Evins and P. Oppeneer, "Ab Initio Atomistic Thermodynamics of Water Reacting with Uranium Dioxide Surfaces," *J. Phys. Chem C*, vol. 118, pp. 8491-8500, 2014.
- [58] M. Castell, "Wulff shape of microscopic voids in  $\text{UO}_2$  crystals," *Phys. Rev. B.*, vol. 68, pp. 235411-1, 8, 2003.
- [59] F. Valdivieso, V. Francon, F. Byasson, M. Pijolat, A. Feugier and V. Peres, "Oxidation behavior of unirradiated sintered  $\text{UO}_2$  pellets and powder at different oxygen partial pressures above 350 C," *J. Nuclear Materials*, vol. 354, pp. 85-93, 2006.
- [60] G. Rousseau, L. Desgranges, F. Charlot, N. Millot, J. Niepce, M. Pijolat, F. Valdivieso, G. Baldinozzi and J. Berar, "A detailed study of  $\text{UO}_2$  to  $\text{U}_3\text{O}_8$  oxidation phases and the associated rate-limiting steps," *J. Nuc. Mat.*, vol. 355, pp. 10-20, 2006.
- [61] B. Carey, "Surface Oxidation Study of Uranium Dioxide Under Wet and Dry Conditions," Thesis, Air Force Institute of Technology, Wright-Patterson AFB, OH, 2005.
- [62] C. Young, J. Petrosky, J. H. E. Mann, D. Turner and T. Kelly, "The work function of hydrothermally synthesized  $\text{UO}_2$  and the implications for semiconductor device fabrication," *Phys. Stat. Sol. (RRL)*, 2016.
- [63] J. Schoenes, "Optical properties and electronic structure of  $\text{UO}_2$ ," *Journal of Applied Physics*, vol. 49, no. 3, pp. 1463-1465, 1978.
- [64] Y. Baer and J. Schoenes, "Electronic Structure and Coulombic Correlation Energy in  $\text{UO}_2$  Single Crystal," *Solid State Communications*, vol. 33, pp. 885-888, 1980.
- [65] S. Hufner, Photoelectron Spectroscopy, Principles and Applications, 3rd Ed., Heidelberg: Springer, 2003.
- [66] Handbook of Chemistry and Physics, Boca Raton: CRC Press, 1992.

- [67] R. Chiechi, E. A. Weiss, M. D. Dickey and G. Whitesides, "Eutectic Gallium-Indium (EGaIn): A Moldable Liquid Metal for Electrical Characterization of Self-Assembled Monolayers," *Angew. Chem. Int. Ed.* , vol. 47, pp. 142-144, 2008.
- [68] T. Meek, M. Hu and J. Haire, "Semiconductive Properties of Uranium Oxides," in *Waste Management 2001 Symposium*, Tucson, 2001.
- [69] J. F. Ziegler , M. Ziegler and J. Biersack, "SRIM - The stopping and range of ions in matter (2010)," *Nuclear Instruments and Methods in Physics Research*, vol. 268, no. 11-12, pp. 1818-1823., 2010.
- [70] ORTEC, *Model 142PC Preamplifier Operating and Service Manual, Rev B.*, ORTEC / Advanced Measurement Technology, 2002.
- [71] H. S. S. Division, "Characteristics and Use of Charge Aamplifier, Technical Information SD-37," Hamamatsu Photonics, Hamamatsu City, Japan, 2001.
- [72] G. F. Knoll, *Radiation Detection and Measurement*, 2d Ed., New York: John Wiley and Sons, 1989.
- [73] R. Bartnikas, *Engineering Dielectric Vol. IIB, Electrical Properties of Solid Insulating Materials: Measurement Techniques*, Baltimore: American Society for Testing and Materials, 1987.



REPORT DOCUMENTATION PAGE				Form Approved OMB No. 074-0188	
<p>The public reporting burden for this collection of information is estimated to average 1 hour per response, including the time for reviewing instructions, searching existing data sources, gathering and maintaining the data needed, and completing and reviewing the collection of information. Send comments regarding this burden estimate or any other aspect of the collection of information, including suggestions for reducing this burden to Department of Defense, Washington Headquarters Services, Directorate for Information Operations and Reports (0704-0188), 1215 Jefferson Davis Highway, Suite 1204, Arlington, VA 22202-4302. Respondents should be aware that notwithstanding any other provision of law, no person shall be subject to a penalty for failing to comply with a collection of information if it does not display a currently valid OMB control number.</p> <p><b>PLEASE DO NOT RETURN YOUR FORM TO THE ABOVE ADDRESS.</b></p>					
1. REPORT DATE (DD-MM-YYYY) 29-08-2016		2. REPORT TYPE Dissertation		3. DATES COVERED (From – To) Sept. 2013 – Sept. 2016	
TITLE AND SUBTITLE  <b>Evaluation of Hydrothermally Synthesized Uranium Dioxide for Novel Semiconductor Applications</b>				5a. CONTRACT NUMBER	
				5b. GRANT NUMBER	
				5c. PROGRAM ELEMENT NUMBER	
6. AUTHOR(S)  Young, Christopher M., LTC, USA				5d. PROJECT NUMBER	
				5e. TASK NUMBER	
				5f. WORK UNIT NUMBER	
7. PERFORMING ORGANIZATION NAMES(S) AND ADDRESS(S) Air Force Institute of Technology Graduate School of Engineering and Management (AFIT/ENP) 2950 Hobson Way, Building 640 WPAFB OH 45433-8865				8. PERFORMING ORGANIZATION REPORT NUMBER  AFIT-ENP-DS-16-S-027	
9. SPONSORING/MONITORING AGENCY NAME(S) AND ADDRESS(ES) Domestic Nuclear Detection Office Samantha Connelly 245 Murray Lane, Suite #0115 Washington, DC 20528 <a href="mailto:Samantha.connelly@dhs.gov">Samantha.connelly@dhs.gov</a>				10. SPONSOR/MONITOR'S ACRONYM(S)  DNDO	
				11. SPONSOR/MONITOR'S REPORT NUMBER(S)	
12. DISTRIBUTION/AVAILABILITY STATEMENT DISTRIBUTION STATEMENT A. APPROVED FOR PUBLIC RELEASE; DISTRIBUTION UNLIMITED.					
13. SUPPLEMENTARY NOTES This material is declared a work of the U.S. Government and is not subject to copyright protection in the United States.					
14. ABSTRACT Neutron radiation detection is an important part of the national strategy for nonproliferation efforts worldwide. Key to the success of these programs is detector material development which establishes the limits of efficiency, sensitivity, and power usage for a detector of practical use. This research focused upon the study of neutron detection using single crystal actinide compounds, specifically UO <sub>2</sub> , taking advantage of the successful hydrothermal synthesis of UO <sub>2</sub> at the Air Force Research Laboratories. Initial indications are that this material may be of sufficient quality for semiconductor application.					
15. SUBJECT TERMS UO <sub>2</sub> , Uranium Dioxide, Semiconductor, Radiation Detection, Hydrothermal growth					
16. SECURITY CLASSIFICATION OF:			17. LIMITATION OF ABSTRACT  UU	18. NUMBER OF PAGES  137	19a. NAME OF RESPONSIBLE PERSON James C. Petrosky, AFIT/ENP
a. REPORT  U	b. ABSTRACT  U	c. THIS PAGE  U			19b. TELEPHONE NUMBER (Include area code) (937) 255-6565, ext 4562 (james.petrosky@afit.edu)

Standard Form 298 (Rev. 8-98)  
Prescribed by ANSI Std. Z39-18